High-Rate Irradiation of 15mm Muon Drift Tubes and Development of an ATLAS Compatible Readout Driver for Micromegas Detectors

Dissertation der Fakultät für Physik

der

Ludwig-Maximilians-Universität München

vorgelegt von

André Zibell

geboren in Starnberg

München, den 25.04.2014

Erstgutachter: Prof. Dr. Otmar Biebel
Zweitgutachter: Prof. Dr. Wolfgang Dünnweber

Tag der mündlichen Prüfung: 6.6.2014

Kurzfassung

Die zukünftigen Upgrades des LHC Beschleunigers am CERN erfordern mehrere Verbesserungen der Detektoren des ATLAS Myonspektrometers, hauptsächlich wegen der damit einhergehenden Erhöhung der unkorrellierten Untergrund Trefferrate.

Dies betrifft auch das "Small Wheel" des ATLAS Endkappen-Myonspektrometers. Eine präzise Myon Spurrekonstruktion kann nicht länger sichergestellt werden, wenn die Luminosität gegen 2020 um einen Faktor 2 bis 5 oberhalb des Designwertes von $1 \times 10^{34} \mathrm{cm}^{-2}\mathrm{s}^{-1}$ liegen wird, und wegen der Untergrund Trefferraten oberhalb von 10 kHz/cm^2. Dies, zusammen mit dem Bedarf an einer zusätzlichen Triggerstation mit einer Winkelauflösung besser als 1 mrad, erfordert den Bau von "New Small Wheel" Detektoren. Der Austausch ist für die lange Wartungsperiode 2018 und 2019 geplant.

Als mögliche Technologie für die beiden New Small Wheels wurden sMDT Driftrohre, basierend auf der ATLAS 30 mm Monitored Drift Tube Technologie, getestet. Bei einem halbierten Durchmesser von 15 mm erwartet man diese als genügend hochratenfest.

In der vorliegenden Arbeit wurde am Münchner Tandembeschleuniger eine sMDT Prototypenkammer unter dem Einfluss von Protonen-, Neutronen- und Photonenbestrahlung bei hohen Raten getestet, und somit die Bedingungen für ein LHC Hochluminositätsexperiment nachgestellt.

Spurauflösung und Rekonstruktionseffizienz für minimalionisierende Myonen werden als Funktion der Bestrahlungsrate präsentiert. Die Geometrie der Myonentrigger im Experiment erlaubt es, zwischen Effizienzverlusten aufgrund von elektronischen Totzeiteffekten und Raumladungseffekten zu unterscheiden. Mittels modifizierter Ausleseelektonik wurde die analoge Pulsform der Detektoren im Hinblick auf eine Abnahme der Gasverstärkung und potentielle Unregelmäßigkeiten aufgrund der hohen Bestrahlungsraten und -stärken untersucht.

Das Ergebnis der Studie zeigt, dass die sMDT Detektortechnologie die hohen Anforderungen an die New Small Wheel Detektoren erfüllt. Bei einer Bestrahlungsrate von 10 kHz/cm^2 liegt die mittlere Einzelrohr-Ortsauflösung bei 140 μm und die Spurrekonstruktionseffizienz bei etwa 72% pro Rohrlage.

Als weitere Technologie für die New Small Wheels wurden Micromegas Detektoren vorgeschlagen. Diese mikrostrukturierten planaren Gasdetektoren mit hoher Ortsauflösung sind konstruktionsbedingt hochratenfest und erlauben zusätzlich Winkelauflösung und Spurrekonstruktion in einer einzelnen Detektorlage. 2013 hat sich die ATLAS Kollaboration für diese Technologie als Präzisions-Spurdetektoren in den New Small Wheels entschieden.

Ein Prototyp Micromegas Detektor wird im Sommer 2014 auf einem der beiden ATLAS Small Wheels installiert als Technologietest und Probedurchlauf der nötigen Änderungen an ATLAS Hard- und Software. Hierfür ist ein ATLAS-kompatibler Read Out Driver (ROD) entwickelt worden, der es erlaubt, die Prototypkammer vollständig in die ATLAS Datenaufnahme zu integrieren, um somit

den Erkenntnissgewinn aus der Installation zu maximieren. Die Hardware dieser Ausleseelektronik basiert auf modernsten FPGAs und wurde im Rahmen der RD51-Kollaboration als Scalable Readout System entworfen.

Das Firmwaredesign, seine Funktionalität und die Verbindungsglieder zwischen den verschiedenen Komponenten der Auslesekette werden unter Verwendung von APV25 Auslesekarten vorgestellt. Alle anfänglichen Probleme des Systems wurden im Rahmen dieser Arbeit behoben.

Das System wurde erfolgreich in die Auslesekette des LMU Höhenstrahl Messstandes integriert und somit sowohl mit der Ausleseelektronik der ATLAS Monitored Drift Tubes, als auch einer VME-basierten Datenaufnahme synchronisiert. Innerhalb der ATLAS Datenaufnahmekette wurden zwischenzeitlich weitere erfolgreiche Integrationstests durchgeführt. Als Ergebnis ist das Systems bereit, um innerhalb des ATLAS Detektors problemlos eingesetzt zu werden.

Abstract

The upcoming luminosity upgrades of the LHC accelerator at CERN demand several upgrades to the detectors of the ATLAS muon spectrometer, mainly due to the proportionally increasing rate of uncorrelated background irradiation.
This concerns also the "Small Wheel" tracking stations of the ATLAS muon spectrometer, where precise muon track reconstruction will no longer be assured when around 2020 the LHC luminosity is expected to reach values 2 to 5 times the design luminosity of $1 \times 10^{34} \mathrm{cm}^{-2}\mathrm{s}^{-1}$, and when background hit rates will exceed $10\,\mathrm{kHz/cm^2}$. This, together with the need of an additional triggering station in this area with an angular resolution of 1 mrad, requires the construction of "New Small Wheel" detectors for a complete replacement during the long maintenance period in 2018 and 2019.

As possible technology for these New Small Wheels, high-rate capable sMDT drift tubes have been investigated, based on the ATLAS 30 mm Monitored Drift Tube technology, but with a smaller diameter of 15 mm.

In this work, a prototype sMDT chamber has been tested under the influence of high-rate irradiation with protons, neutrons and photons at the Munich tandem accelerator, simulating the conditions within a high luminosity LHC experiment. Tracking resolution and detection efficiency for minimum ionizing muons are presented as a function of irradiation rate. The experimental muon trigger geometry allows to distinguish between efficiency degradation due to deadtime effects and space charge in the detectors. Using modified readout electronics the analog pulse shape of the detector has been investigated for gain reduction and potential irregularities due to the high irradiation rates and ionization doses.
This study shows that the sMDT detectors would fulfill all requirements for successful use in the ATLAS New Small Wheel endcap detector array, with an average spatial resolution of 140 μm and a track reconstruction efficiency of around 72% for a single tube layer at $10\,\mathrm{kHz/cm^2}$ irradiation rate.

A second proposal for a New Small Wheel detector technology are Micromegas detectors. These highly segmented planar gaseous detectors are capable of very high rate particle tracking with single plane angular resolution or track reconstruction. The ATLAS community has decided in 2013 in favor of this technology for precision tracking in the New Small Wheels.

A prototype Micromegas detector will be installed in summer 2014 on the present ATLAS Small Wheel to serve as test case of the technology and as template for the necessary changes to the ATLAS hardware and software infrastructure.
To fully profit from this installation, an ATLAS compatible Read Out Driver (ROD) had to be developed, that allows to completely integrate the prototype chamber into the ATLAS data acquisition chain. This device contains state-of-the-art FPGAs and is based on the Scalable Readout System (SRS) of the RD51 collaboration.

The system design, its necessary functionalities and its interfaces to other systems are presented at use of APV25 frontend chips. Several initial issues with the system have been solved during the development.

The new ROD was integrated into the ATLAS Monitored Drift Tube Readout and into a VME based readout system of the LMU Cosmic Ray Facility. Additional successful operation has been proven meanwhile in several test cases within the ATLAS infrastructure. The whole data acquisition chain is ready for productive use in the ATLAS environment.

Contents

Chapter 1

Introduction

1.1   Proton and ion collisions at the LHC accelerator complex

The Large Hadron Collider (LHC) is a particle accelerator and collider, located in a large underground tunnel at the CERN[1] research site in Geneva, Switzerland. It re-uses the 27 km circumference tunnel of the former LEP accelerator in a depth of around 100 m below surface, to accelerate two beams of proton bunches in opposite direction and collide these bunches at up to 14 TeV center of mass collision energy as design value. It also allows the acceleration and collision of heavy ions, as lead.

Up to 2808 bunches of around 10^{11} protons each circulate in two beams, at a nominal spacing of 25 ns.[2] Until 2013, a spacing of 50 ns has been chosen. The protons bunches are injected into the LHC at an energy of 450 GeV through a series of linear and synchrotron accelerators (See figure 1.1). After acceleration to the desired LHC proton energies, the beams are brought to collision at four designated locations, around which the particle detectors ATLAS, CMS, ALICE, LHCb, TOTEM and LHCf have been built. ATLAS and CMS are designed as multi-purpose detectors, covering a wide range of physics processes like the search for supersymmetry or measurements on the recently discovered Higgs particle [2]. The other experiments are dedicated to special tasks, like the study of B-Mesons within the LHCb experiment or the investigation of the quark-gluon-plasma created by the collision of heavy ions within ALICE.
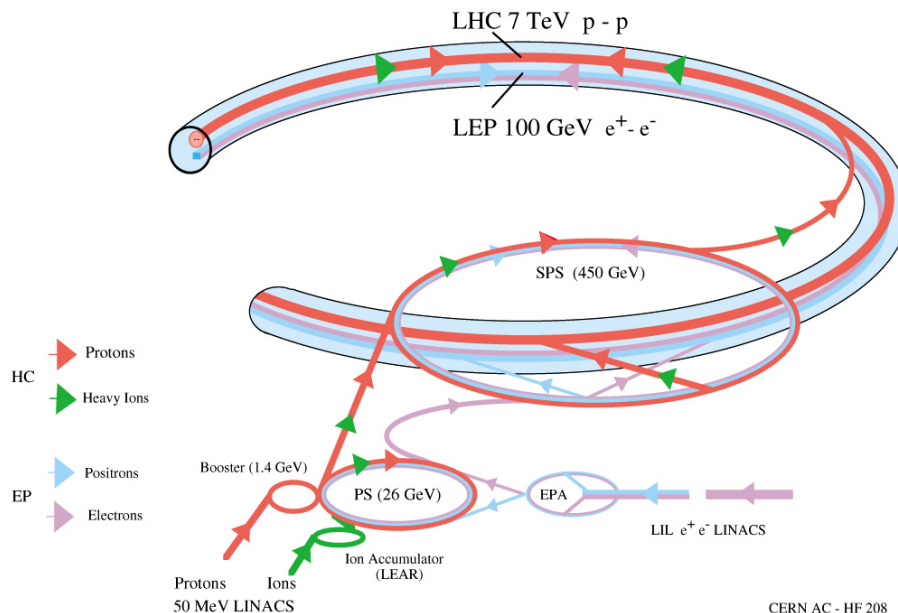
Figure 1.1: The LHC injection complex [3]

LHC operation has started in fall 2008, but after the failure of an electrical interconnection between superconducting magnets on September 19th, extensive repairs had to be carried out. Physics operation therefore started on November 23rd, 2009, with the collision of the first protons. Up to early 2013, the LHC has been operated at a maximum proton energy of 4 TeV per beam, resulting in a maximum center of mass energy of 8 TeV, due to operations safety considerations.

---

[1]Conseil Europeen de recherche nucleaire
[2]Numbers and design parameters in this chapter are taken from the LHC Technical Design Report [1].

1.2   The ATLAS detector

The following section describes the principle of operation of the ATLAS detector, as well as an overview over its main components. The ATLAS detector is the largest of the LHC experiments, being a cylindrical structure of 46 m in length and 25 m in diameter, with a weight of 7000 t. The detector parts that are wrapped in parallel around the LHC beam pipe are referred to as "barrel", and the detector surface is completed by disk-like "end-cap" systems perpendicular to the beam pipe.
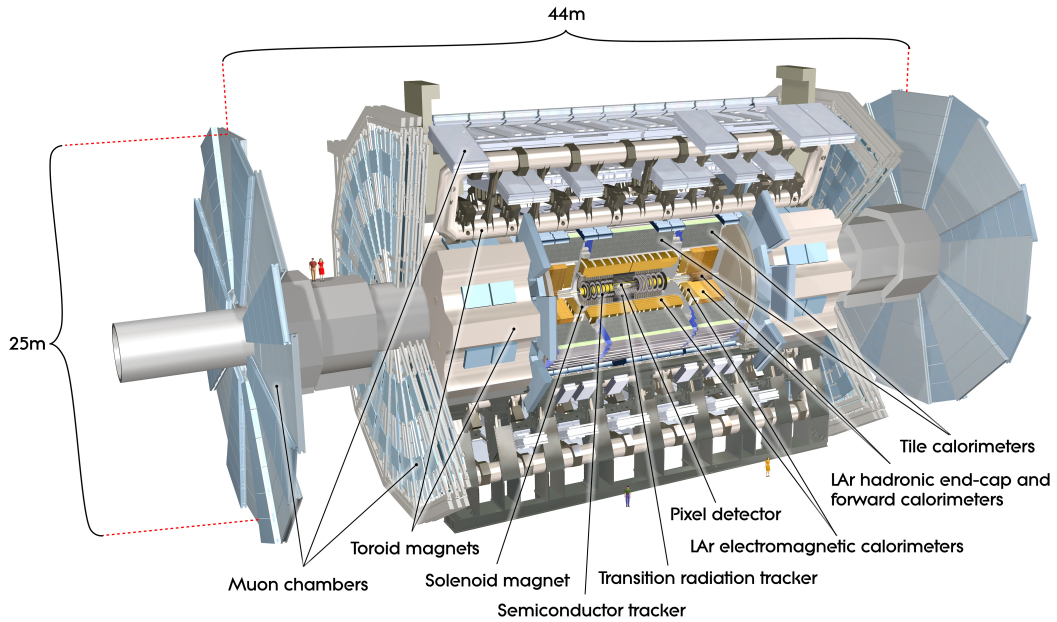
Figure 1.2: Schematic view of the ATLAS detector [4]

The proton bunches collide in the center of the detector, and the products of the collisions are detected in the several concentric shell-like subdetectors of the experiment. These can be sorted into the main categories inner detector, hadronic and electromagnetic calorimeter and muon spectrometer systems. The ATLAS detector also contains a powerful magnet system, forcing charged particles on curved tracks to identify their charge and momentum. The magnet system consists of a central solenoid magnet of about 2 T field strength for the inner detector and calorimeter, and a toroid system each covering barrel and end-caps of the muon system, at an average field strength of 0.4 T.

ATLAS uses a right-handed coordinate system, with the x-axis pointing to the center of the LHC ring and the z-axis along the beam-pipes. When θ measures the polar angle of the direction of a particle coming from the interaction point, its pseudo-rapidity η is given as:

$$\eta = -\log(\tan\frac{\theta}{2})$$

The azimuthal angle ϕ is defined zero at positive x-axis.

1.2.1   Inner tracking detector

The ATLAS inner detector is built from three different subsystems, the pixel detector, semiconductor tracker (SCT) and transition radiation tracker (TRT). It resides within a solenoidal magnetic field, which allows to measure the curvature of the particle tracks at high resolution.

Figure 1.3: Schematic layout of the ATLAS shell-structure and the signature of various particles. [4]

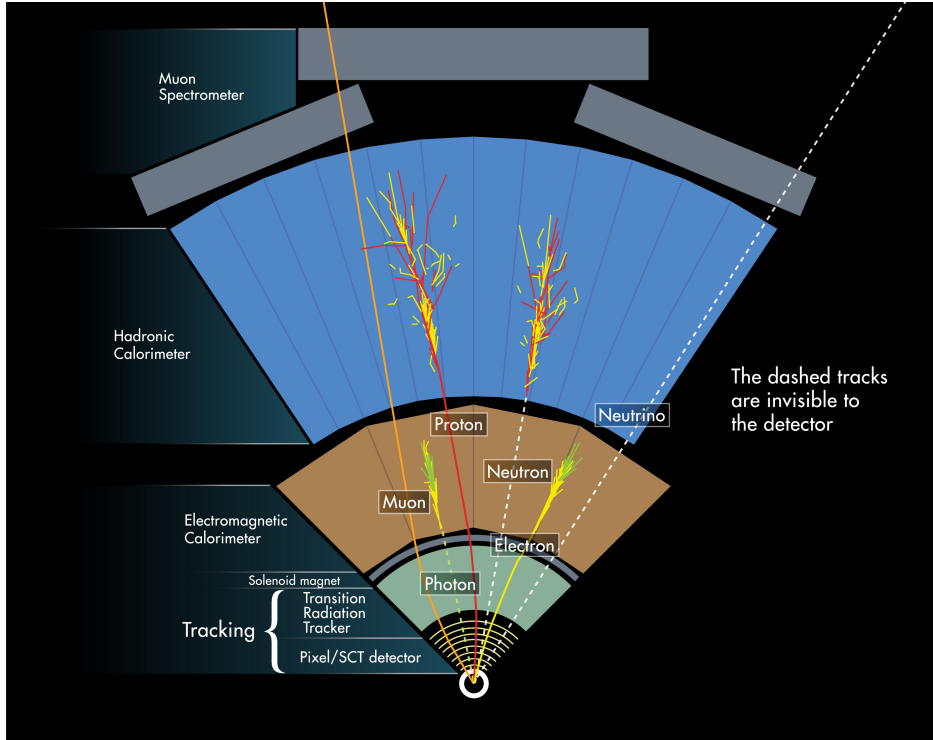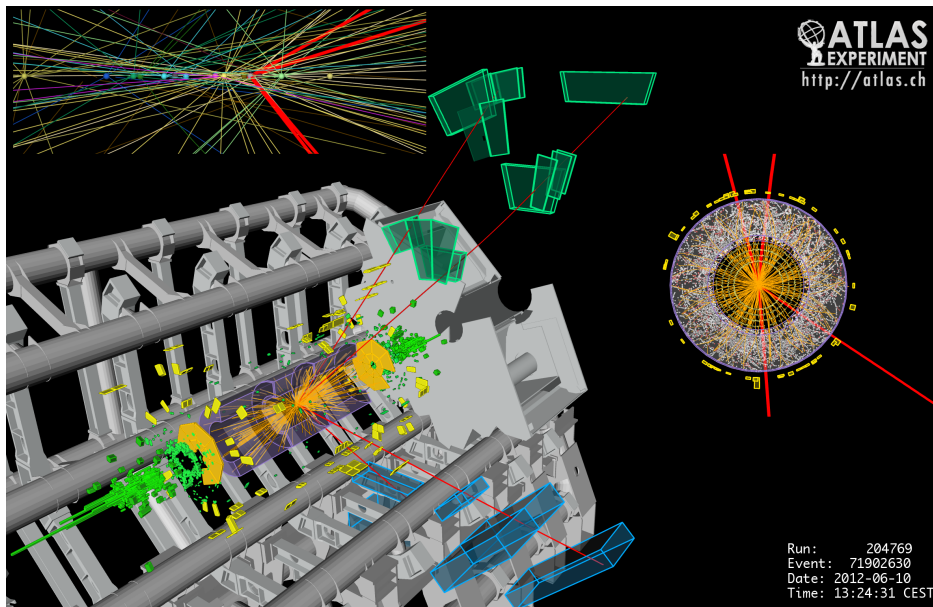**Figure 1.4:** Display of a candidate event for the decay of a Higgs boson into four muons. The image shows the response of the various ATLAS subsystems, that are briefly explained in this section. [4]

1. The Pixel detector is the system closest to the interaction point, and therefore performs at the highest spatial resolution. It consists of silicon wafers containing pixels of 50 x 400 μm^2 in size each. The interaction point is surrounded by three barrel layers of pixels, and three disks at each side of the barrels, for a total of 80 million pixels, covering an area of 1.7 m^2. The pixel modules provide at a high spatial resolution of about 10 μm. [5]

2. The semiconductor tracker is made of eight layers of silicon strip detectors that surround the pixel detector, again in form of concentric barrels and disks. Modules 6.36 x 6.40 cm^2 in size are mounted on carbon-fiber cylinders and contain 768 readout strips at a pitch of 80 μm each. The SCT covers the area down to $|\eta| < 2.5$.

3. The transition radiation racker is the outermost part of the inner detector, reaching up to a radius of 107 cm. It is made out of 370000 straw tubes with a diameter of 4 mm. Barrel tubes are arranged parallel to the beam pipe, end cap tubes radial. In addition to measuring particle tracks by electron drift time in the gas-filled tubes, the detector also contains plastic radiator fibers. These allow to distinguish electrons from other particles due to their transition radiation.
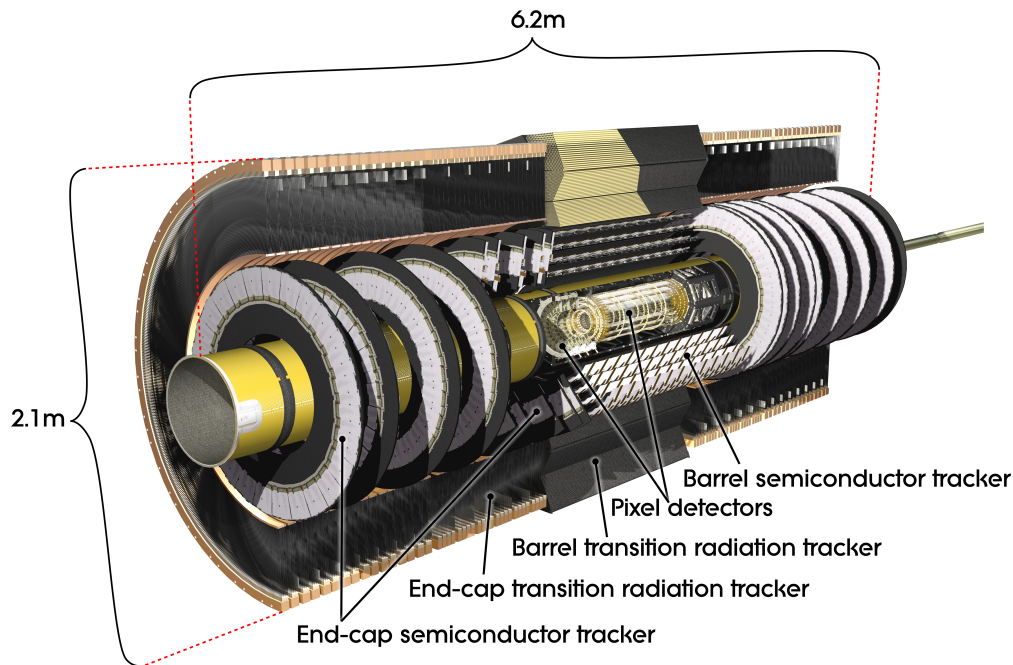
Figure 1.5: Schematic view of the ATLAS inner detector systems [4]

1.2.2 Calorimeter systems

The ATLAS inner detector is surrounded by a large calorimeter system to measure the energies of the particles emerging from the inner detector. The calorimeter systems are built from interleaving layers of high density materials and detectors. The particles interact with the dense material, creating more and more additional particles, which form a bundle of particles that are called shower. The size of the shower can be measured by the interleaving sensing layers, that convert the energy loss of the shower particles into detectable light. Assuming that the calorimeter system is large enough to stop the primary entering particle and its complete cascade of secondary particles, the amount of light detected in the calorimeter allows to reconstruct the shower energy.
The calorimeter system is split into an electromagnetic and a hadronic calorimeter.
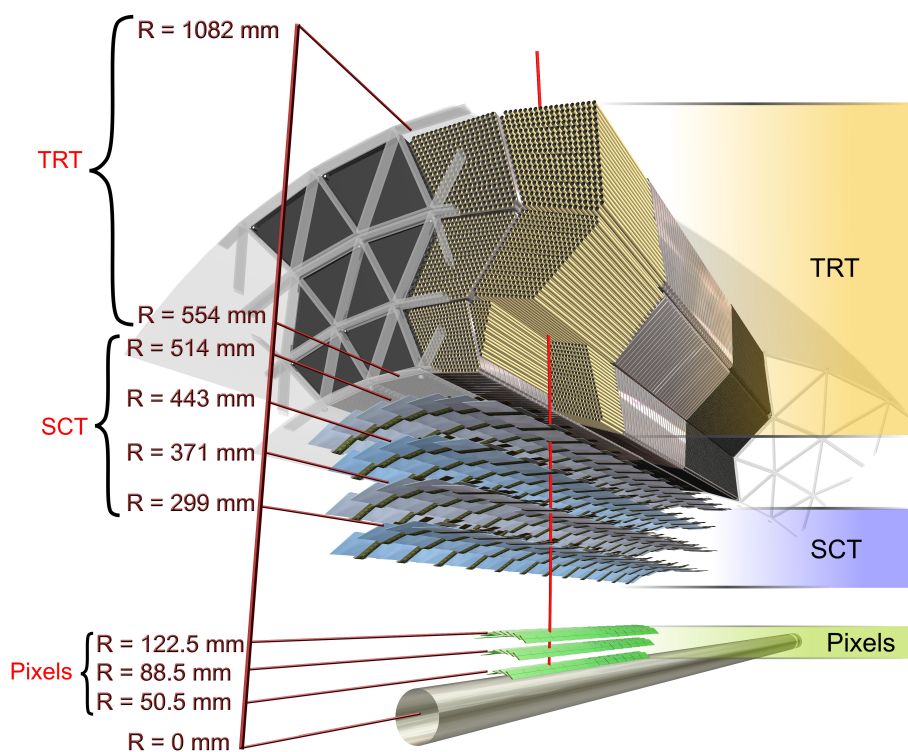
Figure 1.6: Detailed schematic view of the inner detector components [4]

The innermost system consists of electromagnetic barrel and end cap, using metal plates as absorber, interleaved with liquid argon as sensing layers. In forward direction there are additional forward calorimeter systems, close to the beam pipe covering the η range from 3.1 to 4.9 and a hadronic end-cap calorimeter. These systems are fully surrounded radially by the hadronic tile calorimeter, where scintillating plastic tiles are used as active medium.

Apart from shower leakage, the only standard model particles that can exit the calorimeter are neutrinos and muons. A whole detector subsystem is dedicated to the latter.
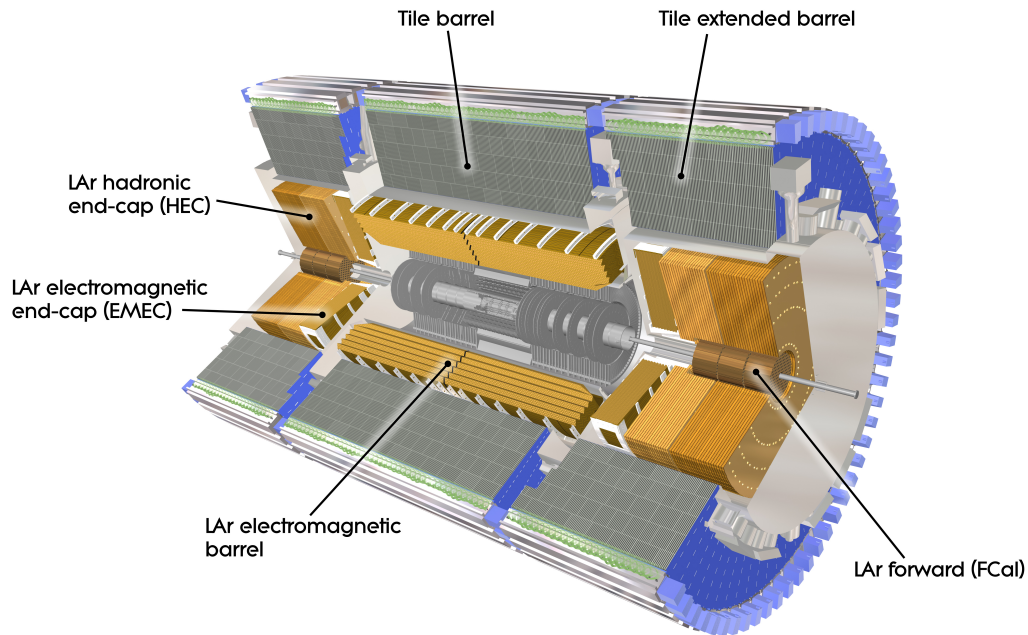
Figure 1.7: Overview over the ATLAS calorimeter components [4]

1.2.3　Muon spectrometer

Muons exiting the calorimeters enter the muon spectrometer. It is the largest of the ALTAS sub detector systems, covering the complete remaining volume outside the calorimeters. Due to the presence of a magnetic field, induced by the barrel- and end-cap toroid magnets, muon tracks are curved, and by determining their sagitta, charge and momentum can be measured. The momentum resolution $\frac{\Delta p}{p}$ needs to be smaller than 10% for a muon transverse momentum of $p_t = 1$ TeV and 3% for 3 GeV $< p_t < 250$ GeV. This requires the muon tracking stations to provide a spatial resolution of better than 100 μm along the η-direction.

Like the inner detector and calorimeter systems, the muon detectors are divided into barrel and end cap chambers.

Muon tracking in the barrel section is performed by three layers of Monitored Drift Tubes (MDT) chambers. This technology will be covered in-depth in chapter 2.1. To trigger on incident muons, the outer and middle layer barrel MDT chambers are backed with Resistive Plate Chambers (RPC), that indicates the presence of a crossing particle at very low latency. The RPC timing resolution is about 1 ns, and RPC detectors additionally provide a coarse spatial resolution of 1 cm, also perpendicular to the MDT precision coordinate.

In forward direction, three stations of disk-shaped muon detector systems are available, the innermost of them called the "small wheels" (see the leftmost boxed region in figure 1.8 and a photo of an

Figure 1.8: Schematic view of a quadrant of the ATLAS muon spectrometer with the collision point in the lower left corner. Horizontal numbered blocks represent MDT chamber layers of the barrel muon spectrometer, vertical blocks represent end cap layers. RPC and TGC tr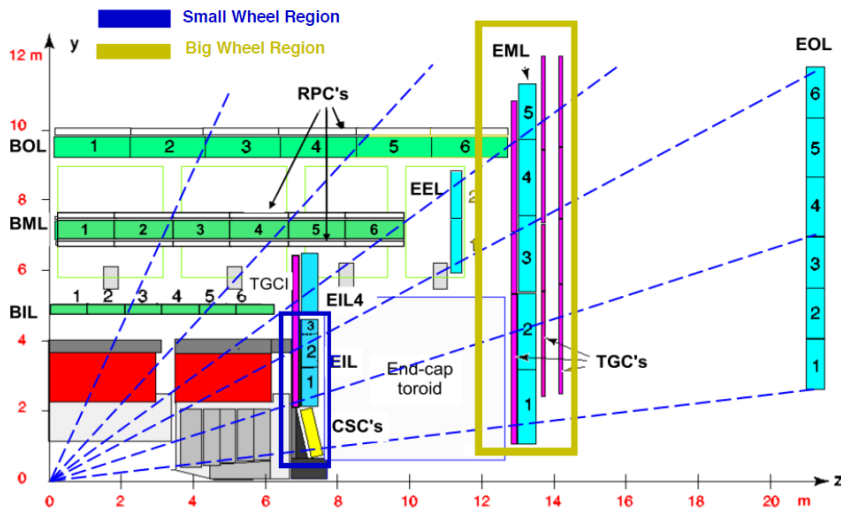igger detectors are also indicated, as well as the CSC tracking stations forming the innermost part of the Small Wheel innermost end cap stations. [8]

assembled small wheel in figure 1.10). This part of the muon system will be covered in detail in chapter 1.5.

Again, MDT chambers are used for muon tracking in the forward region, except for the innermost part of the small wheels, for $2.0 < |\eta| < 2.7$, which is covered by Cathode Strip Chambers (CSC). The endcap muon tracking detectors are equipped with Thin Gap Chambers (TGC) for the generation of a fast trigger signal.

1.2.4   Trigger systems and data acquisition

The ATLAS detector uses a multiple staged trigger system, to reduce the amount of data generated at the bunch crossing rate of 40 MHz to a final value of 200 Hz, that gets stored on hard disks. The first stage to filter out the most interesting events based on several criteria is called Level 1 (L1) trigger. This mechanism selects events at a rate of up to 100 kHz, based on online measurements of the calorimeter and muon systems. Chapter 3.2 is dedicated to the ATLAS trigger and data acquisition system.

1.3   Physics processes and discoveries

During the 2011 operation of the LHC accelerator at a center of mass energy of $\sqrt{s}$=7 TeV the ATLAS detector was able to record an integrated luminosity of 5.08 fb^{-1}. 2012 operation added an additional 21.3 fb^{-1} at $\sqrt{s}$=8 TeV. The evolution of these values is illustrated in figure 1.11.

The ATLAS data analysis groups are examining this large amount of data in search for not only the popular Higgs boson, but also discoveries beyond the standard model.

This includes the search for supersymmetry (SUSY), dark matter, extra dimensions and CP violation. The first milestone analysis result that also caused large public attention is the discovery of a particle, that is consistent with the long predicted but so far undiscovered Higgs boson. On July 4th 2012 both the ATLAS and CMS collaborations were able to claim the discovery of the long-sought Higgs-
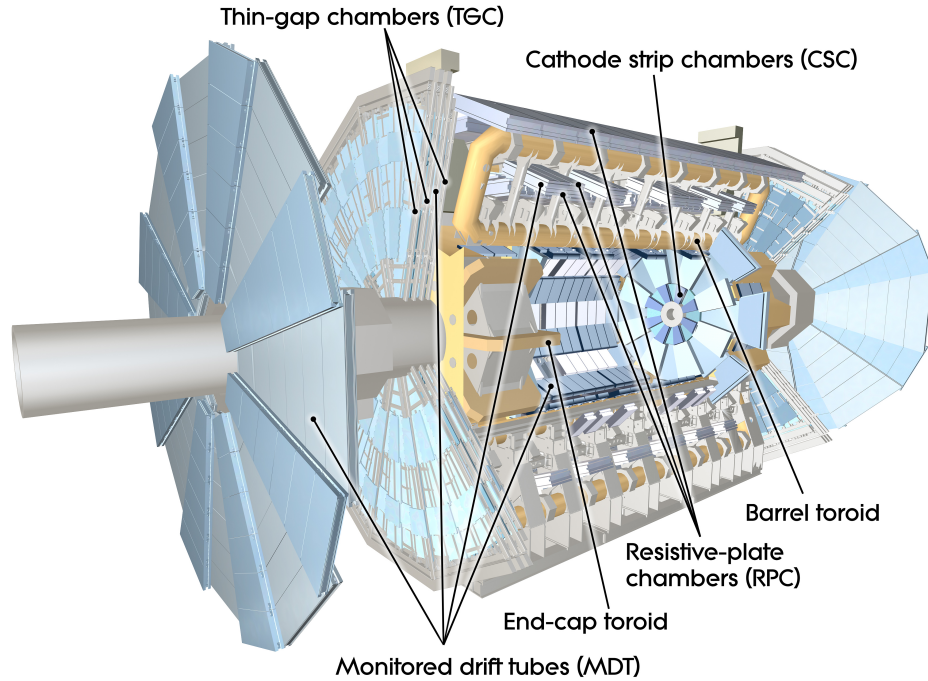
Figure 1.9: Schematic view of the ATLAS Muon spectrometer [4]

Boson. Higgs bosons generated in proton collisions decay into secondary particles, and thus the Higgs boson properties have to be measured indirect via its decay remnants.

Several Higgs boson production mechanisms are possible, of which some are summarized in figure 1.12.

Analyzing the $H \to ZZ* \to 4l$ and $H \to \gamma\gamma$ decay channels, a Standard Model (SM) Higgs Boson was discovered. [2]

The precise muon spectrometer plays an especially important role for the first mentioned process, when the final state contains muons to be reconstructed.

Figure 1.13 shows two plots from the corresponding publication that claim a Higgs boson of 126 GeV mass with a signal strength of 5.9 σ .

Beyond this, muons play an important role in nearly every search for physics beyond the standard model.

1.4 Present and future upgrades of the LHC

In February 2013 the so-called LS1 (Long shutdown 1) began, which will last until November 2014. The LHC magnets and especially their superconducting interconnects will be carefully inspected and if necessary replaced, to allow safe LHC operation at or close to the maximum design beam energy of 7 TeV per beam. In addition, the luminosity will reach or exceed its design value of $1 \times 10^{34} \mathrm{cm}^{-2} \mathrm{s}^{-1}$. Not only the LHC receives modifications, the experiments also take the opportunity to repair and upgrade components. During LS1 the ATLAS detector for example receives a major update by the installation of an additional layer of silicon detectors between the particle collision point and the inner detector, called the Insertable B Layer (IBL).

The next long shutdown (LS2) is then planned for 2018, after which the luminosity is planned to reach a value of $2 - 3 \times 10^{34} \mathrm{cm}^{-2} \mathrm{s}^{-1}$, allowing the accumulation of approximately 100 fb^{-1} of integrated luminosity per year. This period is in the following referred to as High Luminosity
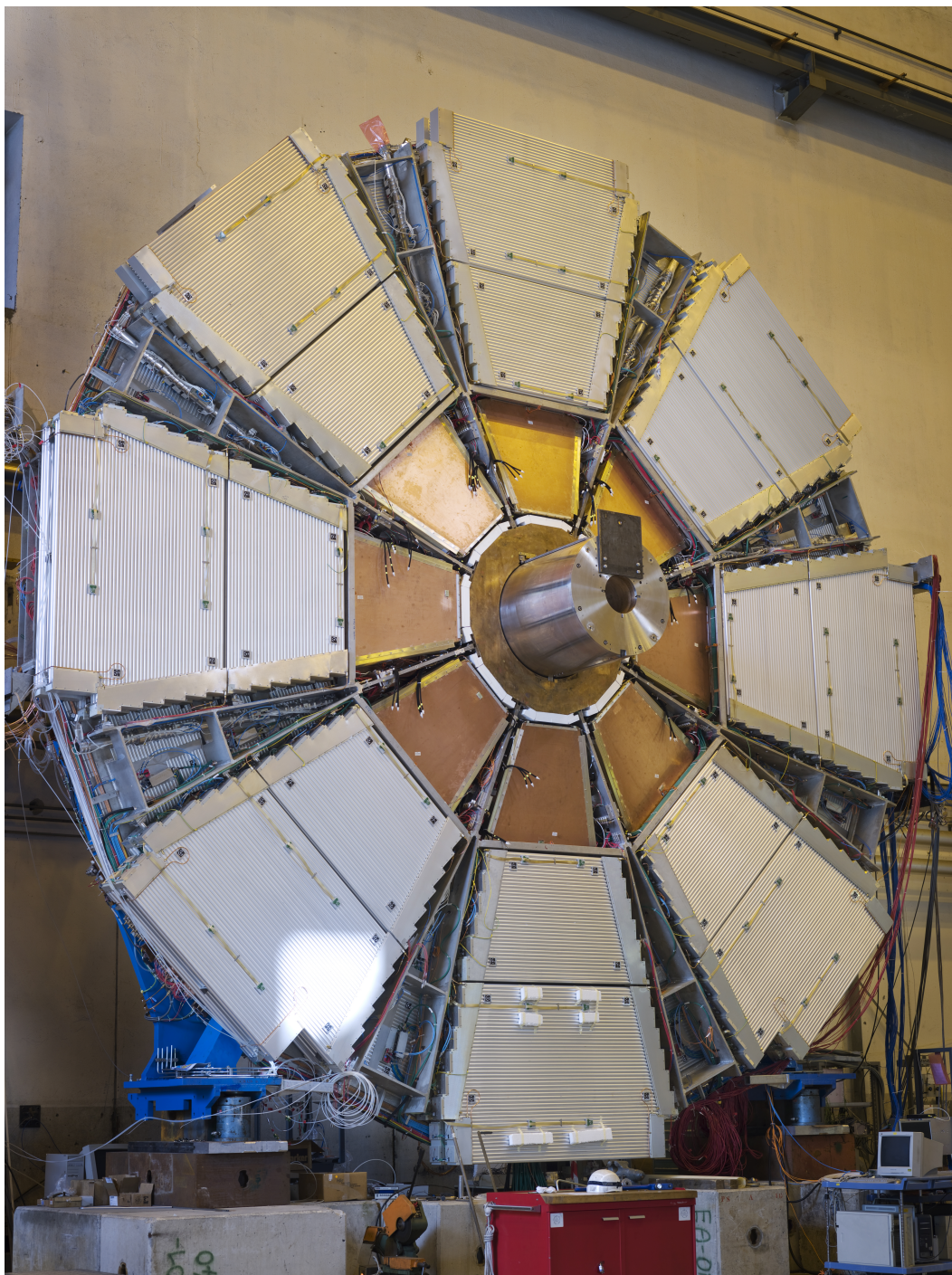
Figure 1.10: Assembled small wheel before installation, with CSC chambers in the inner and MDT chambers in the outer region. [4]
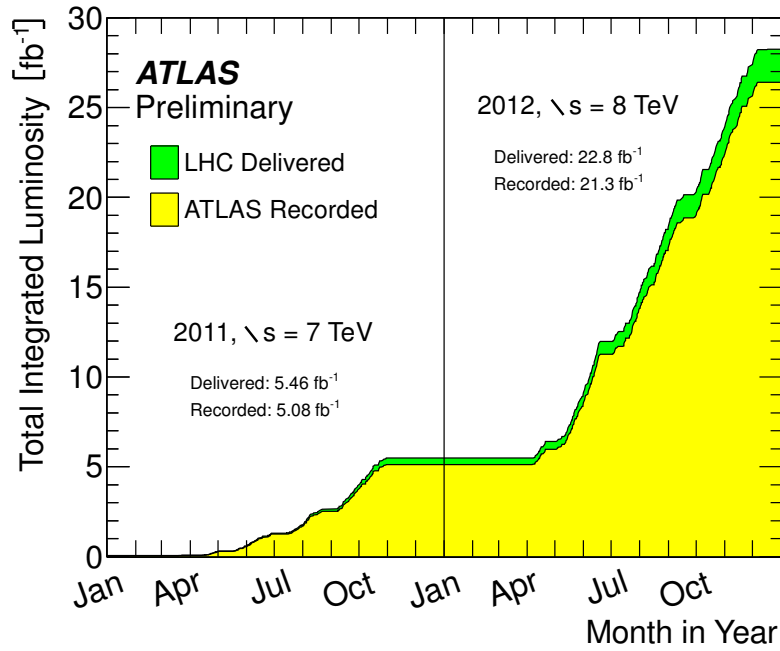
Figure 1.11: Total integrated luminosity delivered by the LHC and captured by the ATLAS detector in 2011 and 2012. [6]

(a) gluon-gluon fusion

(b) vector boson fusion

(c) associated production with W or Z boson

(d) associated production with $t\bar{t}$
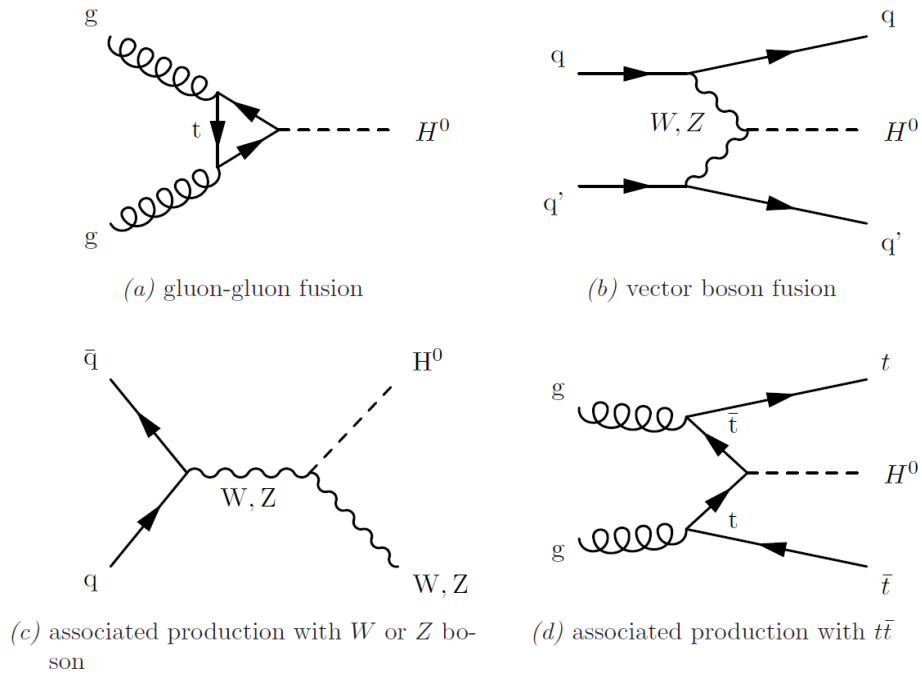
Figure 1.12: The different Higgs boson production mechanisms [7].
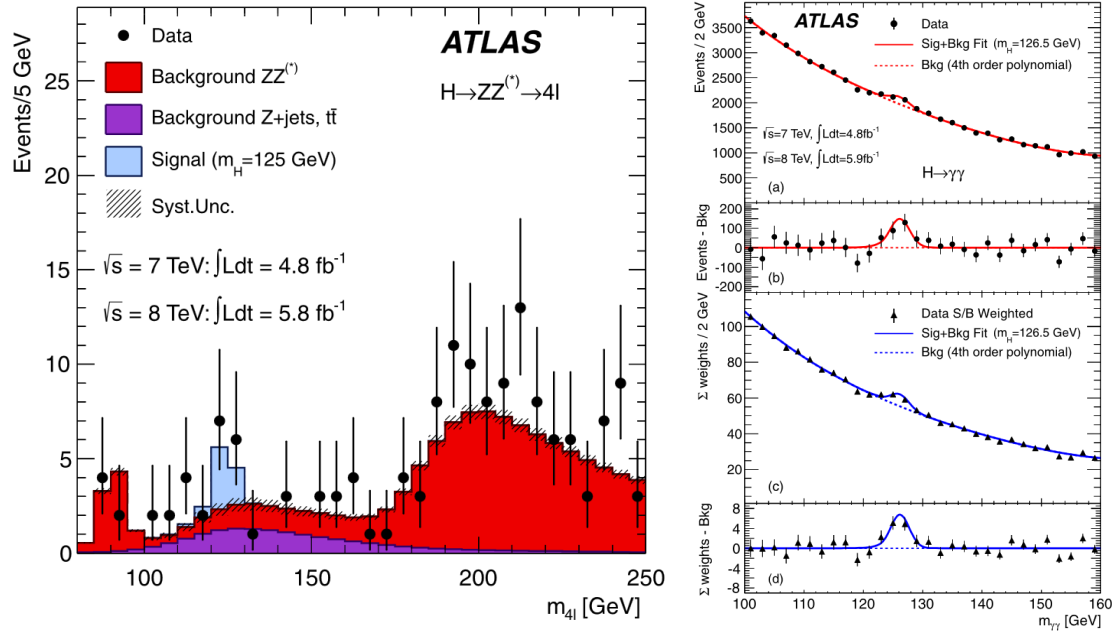
Figure 1.13: ATLAS Results on the search for the Higgs Boson in the H $\to$ ZZ* $\to$ 4l channel (left), and the H $\to$ $\gamma\gamma$ channel (right). [2]

(HL) LHC operation. The mean number of interactions per bunch crossing probably increases to 55 - 80 (pile up) at this luminosity level. At a later point in time after the LS2, subsequent modifications to the Interaction Point (IP) are planned, that will increase the luminosity to its ultimate value of about $5 \times 10^{34} \text{cm}^{-2}\text{s}^{-1}$, resulting in an average 140 interactions per bunch crossing. For an approximate time line of the planned upgrades to the LHC and the ATLAS detector, see figure 1.14.
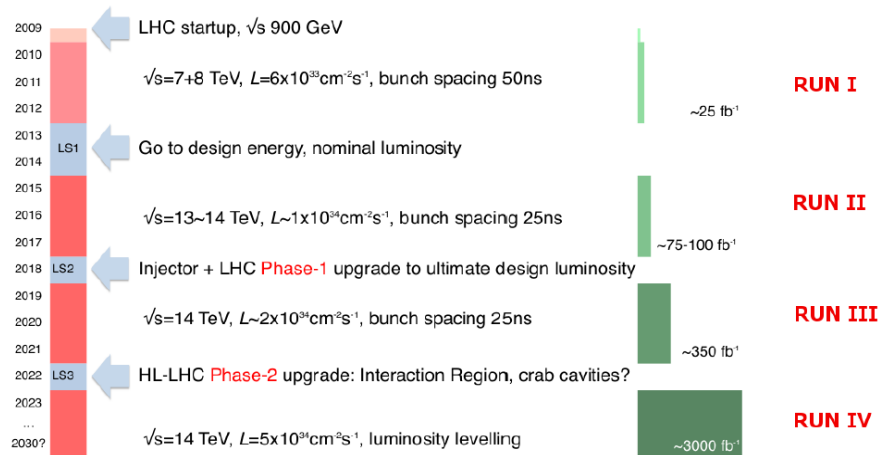
Figure 1.14: Approximate time line of the LHC and ATLAS upgrades, with their increased luminosities of $2 \times 10^{34} \text{cm}^{-2}\text{s}^{-1}$ and $5 \times 10^{34} \text{cm}^{-2}\text{s}^{-1}$ respectively. [8]

As the particle flux in the ATLAS cavern scales at least linearly with luminosity, the uncorrelated hit rate in the muon spectrometer increases by a factor of at least 5 - 7, compared to the values during 2012 operation. Figure 1.15 shows the results of a simulation, that has been performed under the assumption of a luminosity of $1 \times 10^{34} \text{cm}^{-2}\text{s}^{-1}$. Neutron and gamma hit rates increase to several tens

of kHz/cm^2 at the innermost parts of the muon spectrometer [9], compared to the current systems design value of 500 Hz/cm^2

Figure 1.16 illustrates the ratio between measurements and corresponding simulation for a run with a center of mass energy of 7 TeV and a luminosity of 1.9×10^{33}cm^{-2}s^{-1}. In this comparison, simulations are validated within a safety factor of two, allowing predictions for high luminosity conditions.
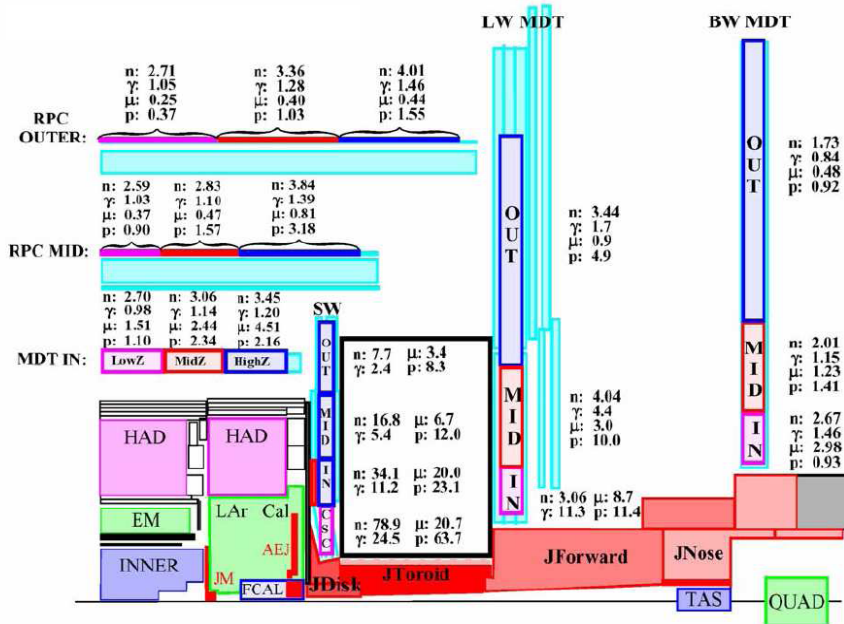
Figure 1.15: Simulation of the background particle fluences at 1×10^{34}cm^{-2}s^{-1} [9].

1.5 The ATLAS New Small Wheel (NSW) project

This increased background particle flux will exceed the rate-capability of the innermost muon end-cap stations, the Small Wheels, and therefore high-precision tracking of muons in this forward direction is no longer guaranteed, as their reconstruction crucially depends on the Small Wheel's measurements. As these receive the highest hit-rate of background radiation, their unavailability or mis-measurements due to channel masking by background hits reaches an unacceptable level. More details on the current performance of the Small Wheel MDT detectors and an extrapolation to higher luminosities can be found in chapter 2.2.

In addition, the ATLAS Level 1 muon trigger in the forward region of the detector is based on track segments reconstructed only in the Big Wheel end cap station. A large fraction of triggers origins in low energy particles generated by interactions with detector material in between the inner and middle stations, and are, therefore, fake triggers, as pictured out in figure 1.17.

Figure 1.18 shows the distribution of muon Level 1 triggers with a trigger threshold of 10 GeV across the ATLAS detector η coordinate, as well as the triggers that could be reconstructed as muons from
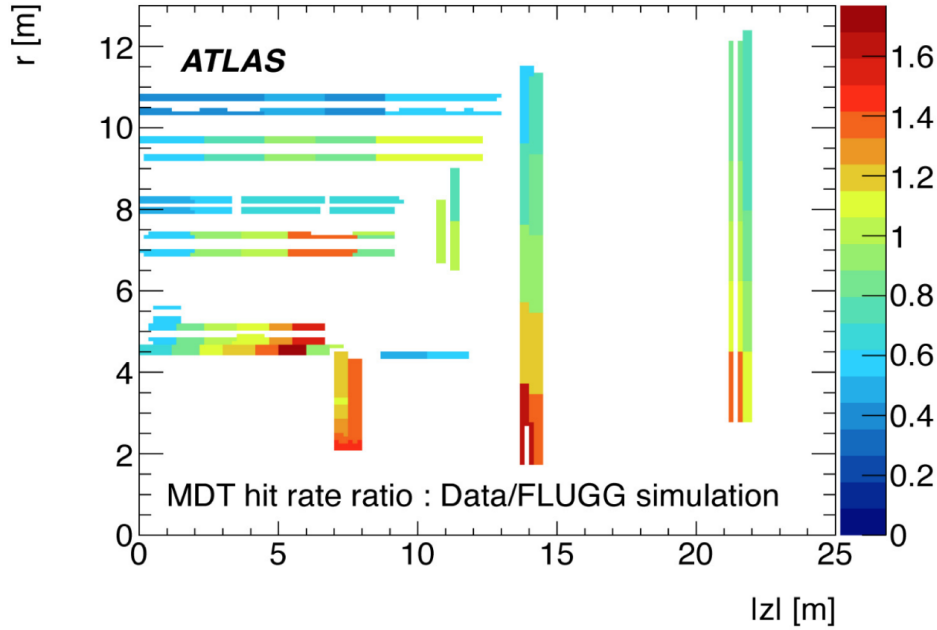
Figure 1.16: Ratio of measured hit rate in the MDT chambers to simulated values, during a run at L=1.9 $\times$ 10^{33}cm^{-2}s^{-1}. [8]

the interaction point with $p_t > 3$ GeV and $p_t > 10$ GeV. The latter show a homogeneous distribution over η. The majority of muon triggers in the end cap region is therefore generated by non-collision particles, occupying valuable trigger bandwidth.

As the maximum Level 1 trigger rate of the ATLAS data acquisition system is limited to around 100 kHz, either the number of triggers has to be prescaled, or the trigger threshold has to be raised. Both options are not desirable, since they result in a loss of valuable physics data.

As an example for the importance of low p_t muon triggers, figure 1.19 shows the momentum distribution of the leading and subleading leptons emerging from the decay of a Higgs boson into two leptons and two neutrinos. In case of muons, a significant loss in event yield would occur, if the trigger threshold would have to be raised for example from 20 GeV to 40 GeV.

To overcome both of these limitations, the ATLAS collaboration decided to exchange the Small Wheels with New Small Wheels (NSW) during the LS2 in 2018. These must be built with detector technologies that are high-rate capable and contribute to the Level 1 muon trigger with high angular resolution. These improvements are expected to keep up the New Small Wheels tracking performance even at high luminosities, and massively reduce the amount of fake triggers in the forward region due to the additional trigger station.

The demands on the New Small Wheel detectors can be summarized as follows. [8]

1. The detectors must withstand the expected particle flux of 14 kHz/cm^2 at HL LHC operating conditions. This corresponds to a charge generation of 45.2 mC/cm^2 per five years of operation where the detectors must not show any gain reduction, material modification or other signs of aging.

2. For offline muon track reconstruction, the spatial resolution of the New Small Wheel tracking detectors must be better than 100 μm to keep up the present muon systems tracking capabilities.

Figure 1.17: Particles originating from the interaction point (A) and from other detector material (B, C), the latter ones resulting in fake triggers if only the Big Wheel stations participate in the trigger decision. [8]
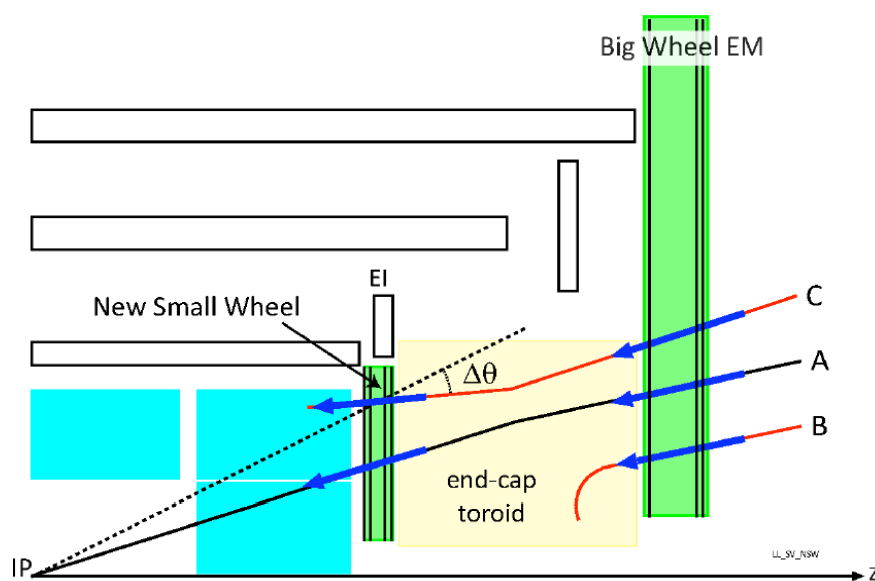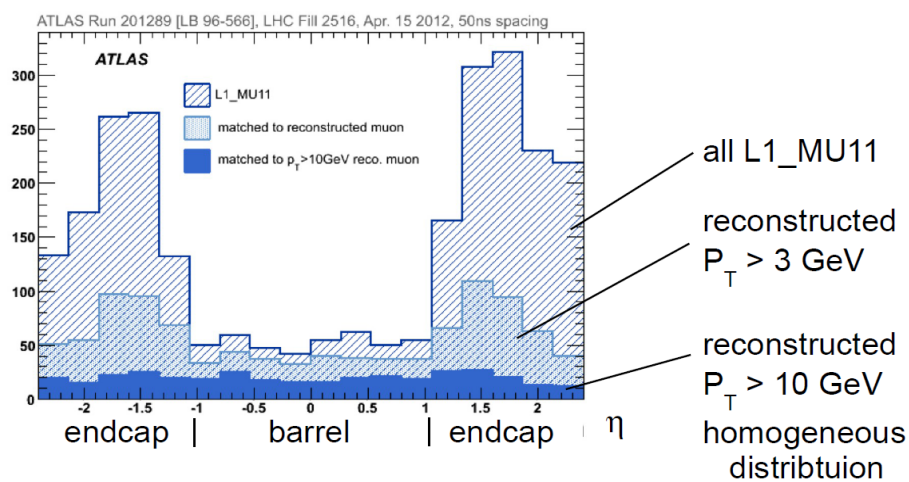

Figure 1.18: Triggers in the current end cap configuration are dominated by fake triggers, that do not origin in collision collision products. [8]
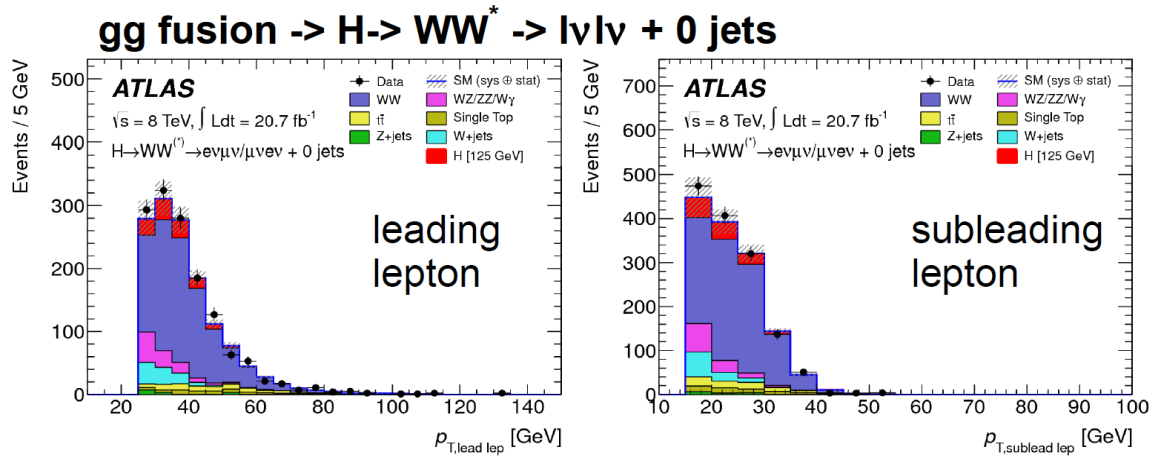
Figure 1.19: p_t distribution of the leptons emerging the decay of a Higgs boson via two W-bosons. As the majority of these have a low p_t value, an increase of the muon trigger threshold would cut away most of these signal events. Therefore it is important of maintain a low p_t trigger even at increased LHC luminosities and background particle fluxes. [8]

3. In order to reduce the Level 1 muon trigger rate in the end-cap region, it is necessary that the New Small Wheel detectors participate in the trigger generation. Here their angular resolution must be better than 1 mrad (RMS). Track segment granularity in the η-Φ-plane must be at least 0.04 x 0.04, to match the current muon triggering system. Online track segment information must arrive at the sector logic electronics within 1.088 μs, which is the delay time of the Big Wheel TGC chambers. The online track segment reconstruction efficiency should be better than 95%.

4. The New Small Wheels must fit into the space of the present Small Wheels. This includes also cooling, cables, alignment equipment and other services.

Several design concepts have been created, how these demands could be achieved, including the different particle detector technologies small strip Thin Gap Chambers (sTGC), Resistive Plate Chambers (RPC), small Monitored Drift Tubes (sMDT) and Micromegas (MM).

Both of the precision tracking technologies choices available, sMDT and Micromegas detectors, are covered in this thesis. A sMDT prototype chamber has been irradiated by high-rate proton and neutron beams to investigate its tracking capabilities for cosmic muons under these conditions, as well as the detector's response to highly ionizing particles. These tests have been performed at the Tandem accelerator facility, located at the MLL (Maier-Leibnitz-Laboratory) in Garching/Munich.

The second part of this thesis covers the development of a FPGA firmware for ATLAS compatible readout electronics for use with Micromegas detectors. The RD51 [10] collaboration at CERN developed a scalable and modular electronic readout system called SRS (Scalable Readout System) [11], which is the hardware basis for a firmware, that turns it into a fully ATLAS-compatible Read Out Driver (ROD).

In May 2012, the ATLAS muon community has chosen to equip the new Small Wheels with sTGC and Micromegas detectors. sTGCs are foreseen as trigger system but also for tracking, whereas Micromegas are supposed to do precision tracking, but also triggering.

The NSW disks will keep the wedged structure of the present small wheels as shown in figure 1.20. Each wheel will be built from eight large sectors and eight small sectors, with their envelope size described in figures 1.21 and 1.22.
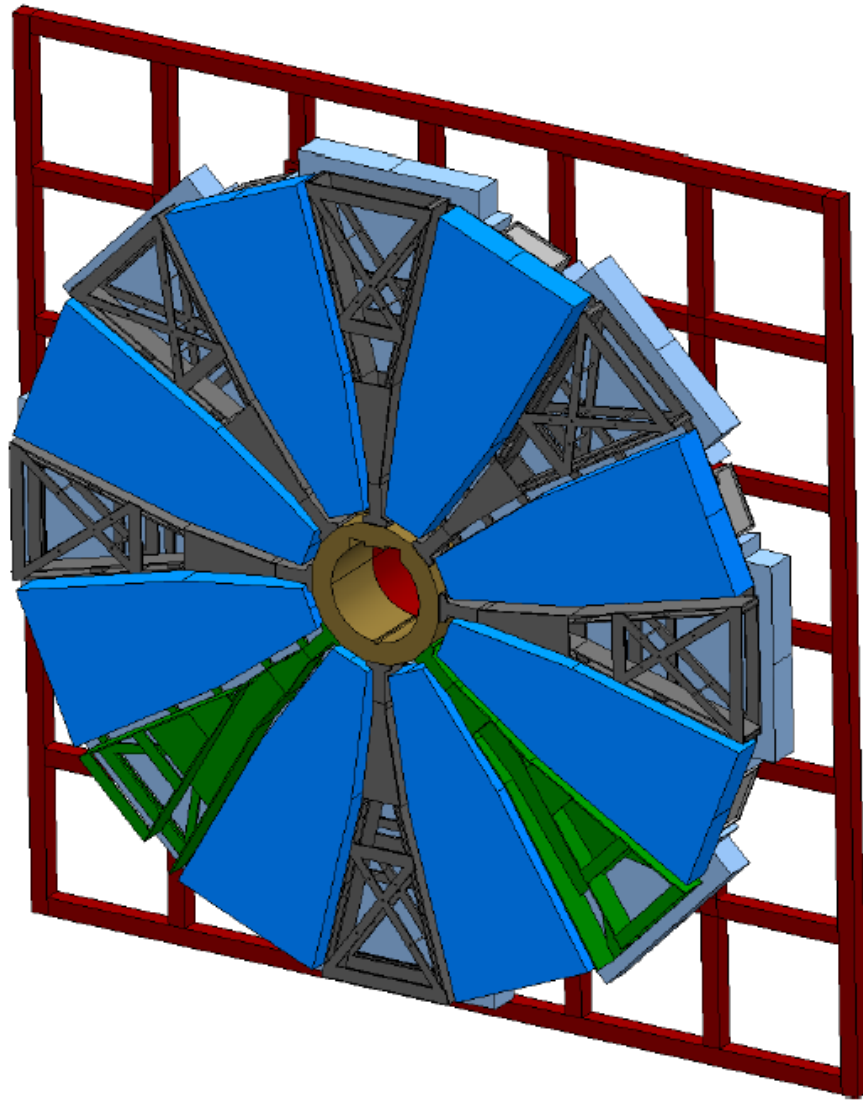
Figure 1.20: Sketch of the New Small Wheel Layout, composed of 8 large sectors and 8 small sectors mountes on a support frame [8].
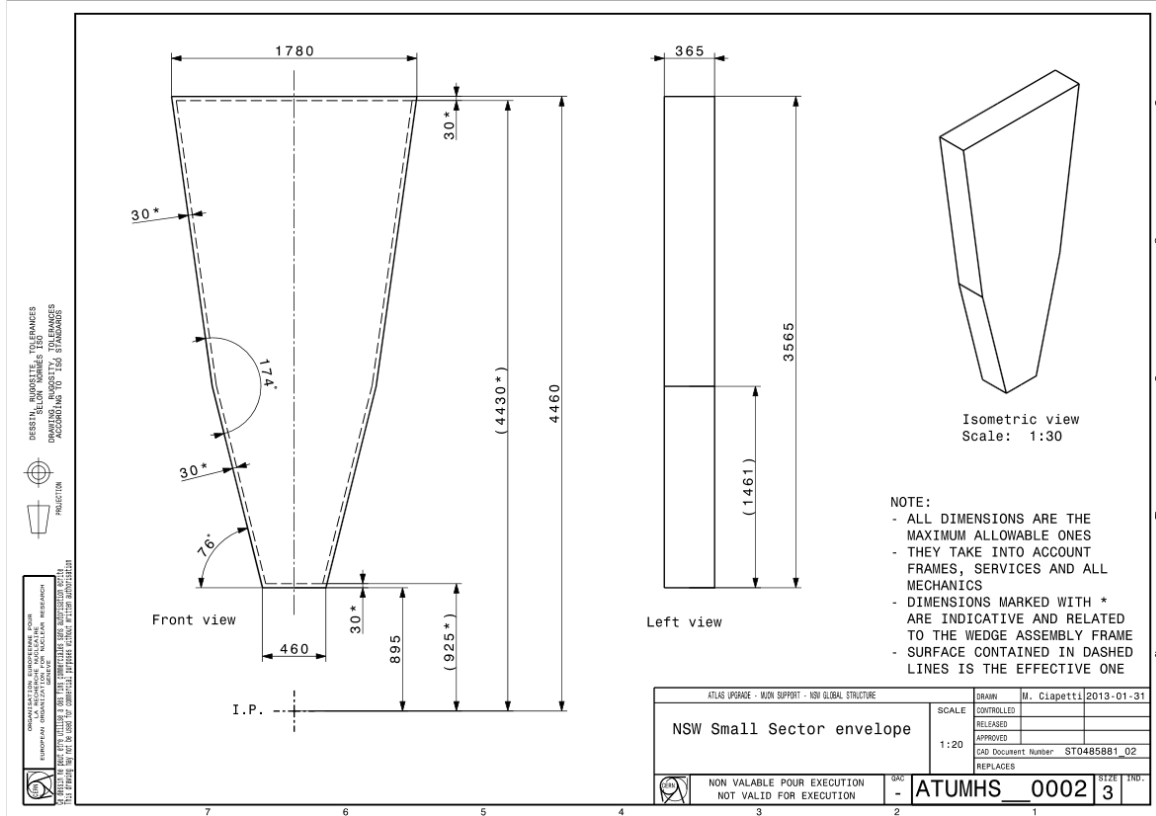
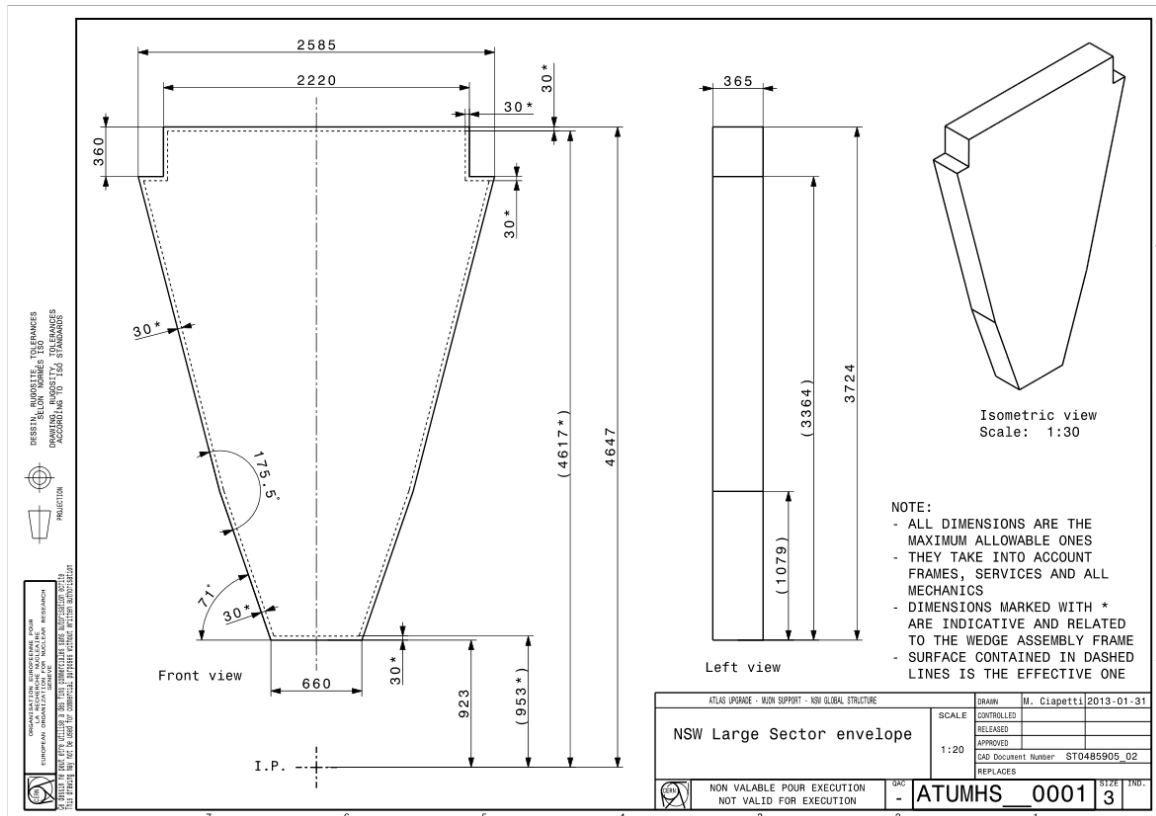**Figure 1.21:** Envelope of a NSW small sector. [8]

Figure 1.22: Envelope of a NSW large sector. [8]

Chapter 2

Irradiation studies with sMDT chambers

The sMDT detector technology is used to build large-area high-rate capable muon tracking detectors. Since the design is based on the Monitored Drift Tube (MDT) technology used in the ATLAS muon spectrometer, the common operation principle is described in chapter 2.1. Chapter 2.2 explains the practical limitations of the MDT technology, whereas chapter 2.3 introduces the sMDT construction and benefits.

A series of background simulating irradiation experiments with a sMDT prototype chamber have been performed at the LMU tandem accelerator facility, see chapter 2.4. These were track measurements and reconstruction of cosmic muons during the irradiation with protons (chapter 2.5) and neutrons (chapter 2.6), as well as the investigation of the analog signal shapes produced by these particles in the sMDT tubes in chapter 2.7.

2.1   Principle of ATLAS MDT operation

The ATLAS inner detectors and calorimeter systems are surrounded by three layers of muon tracking and triggering detectors. These are the inner, middle and outer barrel in the transverse direction, and the Small Wheel, Big Wheel and outer end cap stations in the forward direction. Apart from the CSC chambers on the Small Wheels for $2.0 < \eta < 2.7$, all muon precision tracking is performed by Monitored Drift Tubes (MDT). These tubes are made from 0.4 mm aluminum with 3 cm in outer diameter and a length of up to 6 m. They contain a central anode wire at 3080 V high voltage potential and are filled with a gas mixture of 93 volume percent argon and 7 percent carbon dioxide, at an absolute pressure of 3 bar.

Charged particles crossing the tube gas volume create electron-ion pairs. The amount of ionization is characterized by the Bethe-Bloch formula, the calculation for muons in copper can be seen in figure 2.1. Electric neutral particles create signals via secondary effects. Neutrons can either be captured by nuclei, and the charged β-particle of a subsequent decay of the atom is measured, or a recoil nucleus ionizes the gas. Photons are detected either via photo effect, compton scattering or pair production.
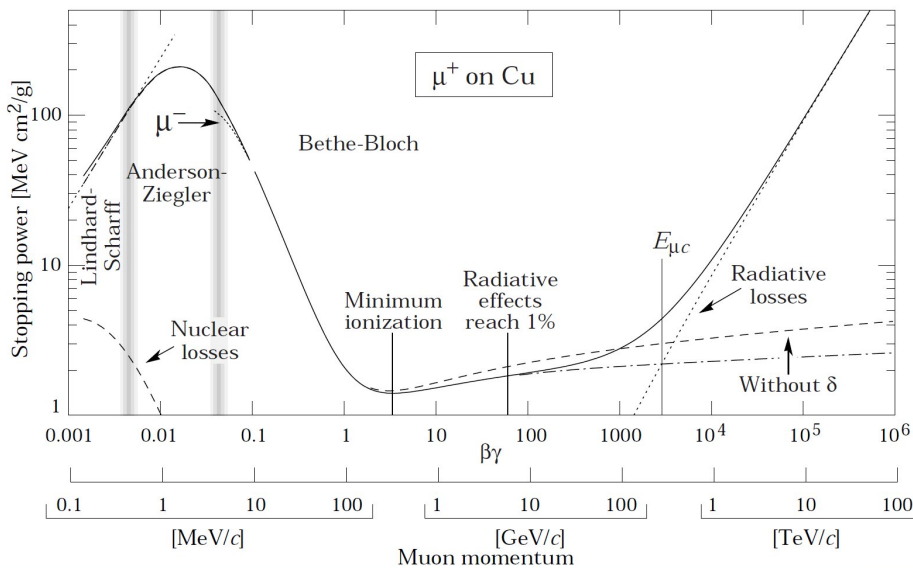
Figure 2.1: Stopping power for muons in copper as a function of $\beta\gamma = p/Mc$ [25]. Although the energy loss in Argon gas is slightly different, the graph shows the minimum ionizing character in the range from cosmic muons with several GeV, up to several hundred GeV within the ATLAS experiment.

Figure 2.2 illustrates the energy loss of muons, calculated for 3 bar argon gas, which approximates the ATLAS gas mixture.
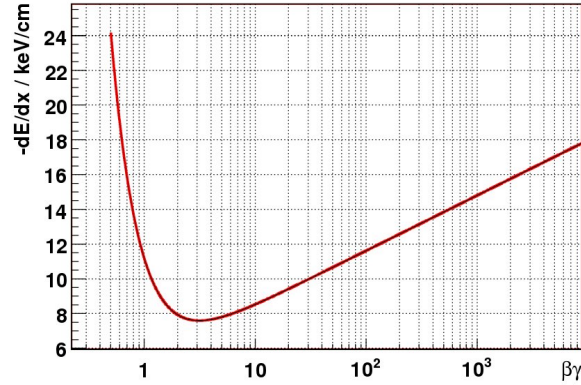
Figure 2.2: Energy loss of muons in argon gas at 3 bar pressure, derived from the Bethe-Bloch formula [26]. In the $\beta\gamma$ range from 3 to 4 a minimum is observed, resulting in a average energy loss due to ionization of around 23 keV in an 30 mm ATLAS drift tube for muons in this range. Due to the Landau distribution of the energy loss, the most probable value of around 21 keV is lower than the mean value.

Due to the radial electric field inside the tube, the electrons drift to the anode wire at a certain, not necessarily constant, speed. The electric field follows the formula

$$E = \frac{U}{r\, ln(\frac{R_2}{R_1})} \tag{2.1}$$

with R_1 being the wire radius of 25 μm. Electrons close to the wire are accelerated enough by the electric field, to ionize gas atoms themselves. This causes a charge avalanche, with a typical amplification factor of 2×10^4 (gas gain).

Due to this multiplication of the primary charge, the electrical signal induced in the wire is large enough, to be picked up by further amplification electronics, and thus an electrical signal is generated, as soon as the closest primary electrons reach the wire.
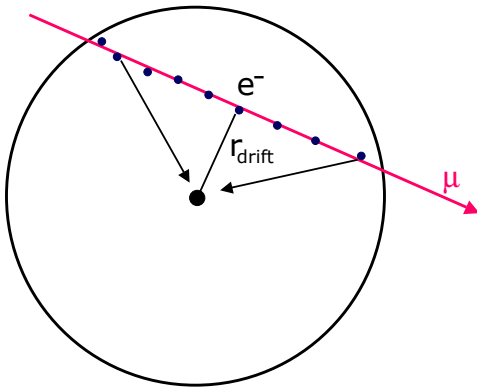
Figure 2.3: Principle of drift tube operation. Free electrons from ionization processes move to the central anode wire at high voltage potential. Drift time is measured for the reconstruction of the drift radius.
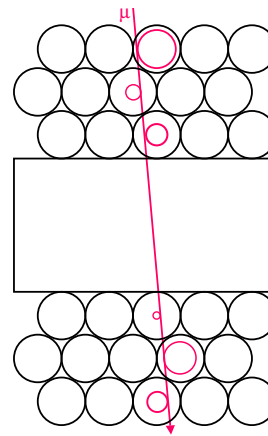
Figure 2.4: Several layers of tubes provide a track segment by fitting a straight line to the drift radii.

The time between the crossing of the particle and the electronic signal of the first electrons arriving at the central wire, is called the drift time. It is the main measurement variable for the MDT system,

and it is correlated with the drift radius by means of the rt-relation. The slope of this rt-relation can be interpreted as the radius-dependent drift velocity of the electrons.

A typical rt-relation for the ATLAS MDT drift tubes is shown in figure 2.5. It is non-linear, especially for radii above 7 mm. Since the rt-relation is sensitive to environmental parameters, like temperature, pressure or gas mixture, regular calibration measurements have to be taken to be able to obtain the correct drift value from the measured drift time.
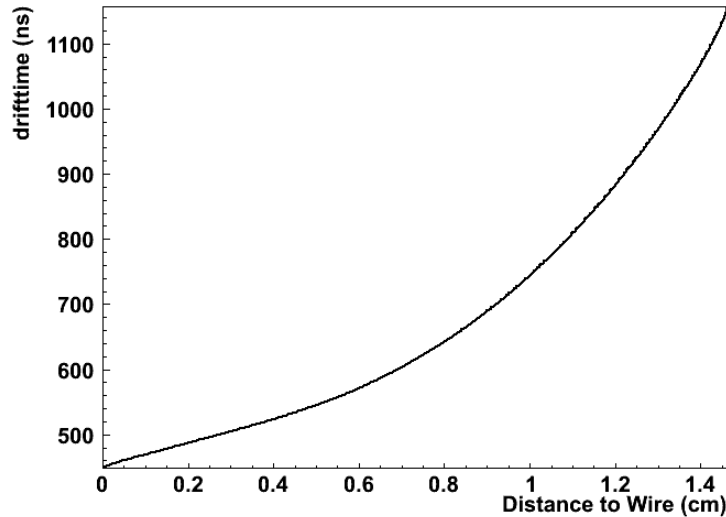
Figure 2.5: Typical nonlinear rt-relation of the standard ATLAS Monitored Drift Tubes (MDT).

Combining the radius measurements of several adjacent tube layers, a straight line fit can be performed to the drift radii, calculated from the measured drift times, as shown in figure 2.4.

In the ATLAS MDT muon chambers, either three or four layers of drift tubes are combined to a multilayer. Two of these multilayers together with a passive spacer in between form a MDT chamber, as depicted in figure 2.6. Depending on the position of the MDT chamber, the length of the tubes reaches up to 6 m.

Track segments from several multilayers are combined to reconstruct the curvature of the muon tracks emerging from the particle collisions. Cosmic muons that enter the cavern from above are detected as well, either as particle background that can be removed from physics data by their track distance from the interaction point and their timing behavior, or in dedicated cosmic runs for calibration during time periods when the LHC is not operational.

To compensate for the unavoidable thermal movements and deformations of the chambers, optical alignment systems are used to monitor each chamber position and deformation, hence the letter M in MDT.

One end of the tubes is dedicated to mount high voltage distribution boards to the chamber, the other end houses frontend electronics boards, referred to as mezzanine cards. Each mezzanine card is plugged onto hedgehog cards, that route the central tube pins connected to the wire onto standard pcb board connectors. A series capacitor on the hedgehog cards ensures DC decoupling of the signal from the wire's high voltage potential. Figure 2.7 shows a picture of a MDT chamber readout side that is partly equipped to illustrate the different components.
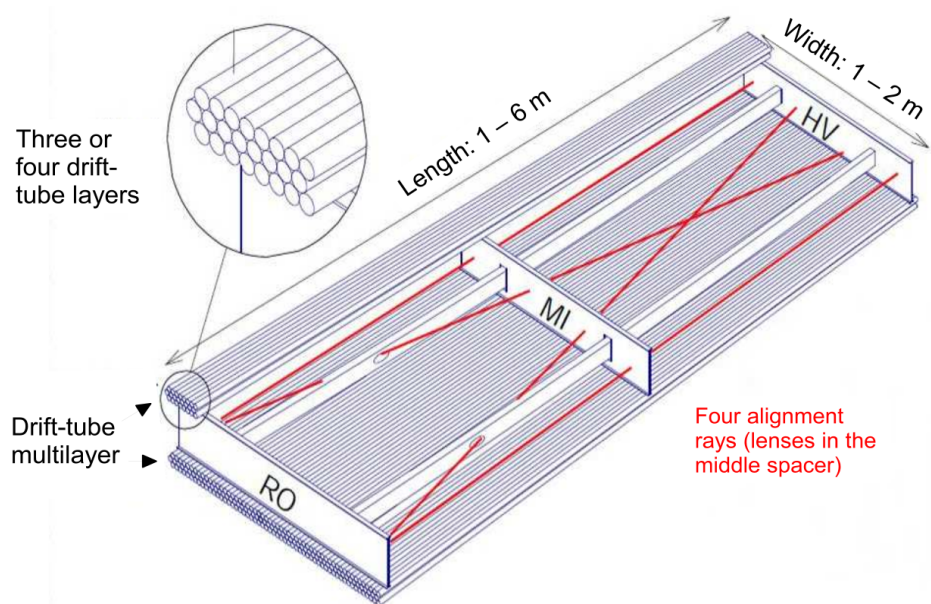
Figure 2.6: Construction drawing of a MDT chamber, containing two multilayers of three tube layers each. Also shown is the optical alignment system that monitors mechanical deformations of the chamber. [27]
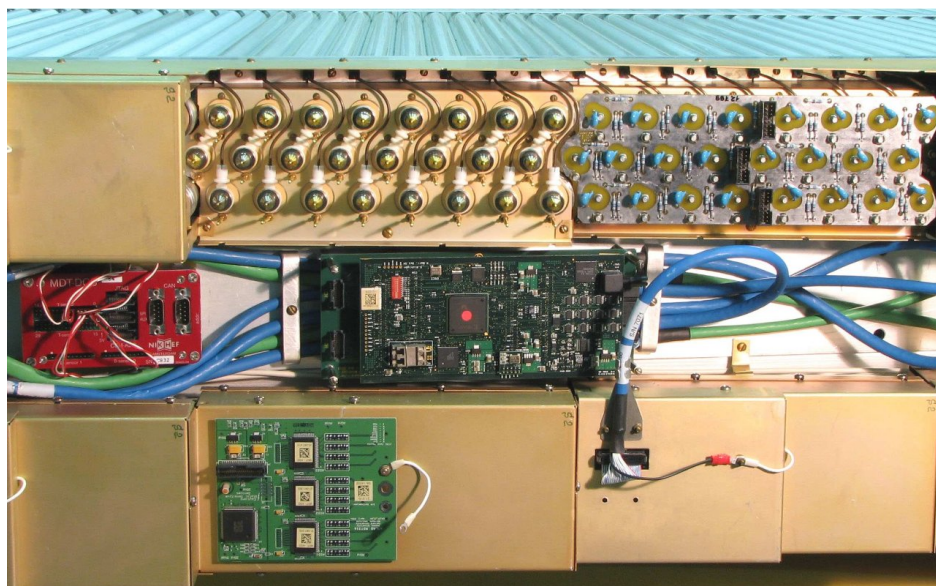
Figure 2.7: Photo of a partly equipped MDT chambers readout side, where the different components can be seen. The upper middle section shows the tube ends with gas connections. Right of that, a hedgehog board has been attached that includes termination resistors, coupling capacitors and connectors for the readout electronics. A mezzanine card has been plugged onto the hedgehog board in the lower middle picture, right of it a mezzanine card is covered by a shielding cage. The center of the image shows a Chamber Service Module and an Embedded Local Monitoring Board (ELMB), (red) on its left. [12]

Every 24 tube section of a multilayer is equipped with a mezzanine board, which houses the frontend electronics to read out these 24 channels. Its main components are three Amplifier, Shaper and Discriminator (ASD) [13] chips and one Atlas Muon Time to digital converter (AMT) [14] chip, both specially designed for the ATLAS muon spectrometer.

The ASD chip performs amplification and conditioning on the charge signal from each of eight tubes, and generates a digital pulse at the time, the first ionization electrons from the tube reach the wire. The pulse width is configurable either correlated to the amplitude or to the Time Over Threshold (TOT) of the analog charge signal.

The AMT chip then digitizes the time that elapsed in between the muon trigger signal and the ASD output pulse, and thus determines the drift time of the electrons for these 24 channels.

One MDT chamber houses up to 18 mezzanine cards, that are all read out by a single Chamber Service Module (CSM) [15], which receives the trigger information and sends the digitized data upstream the data acquisition chain.
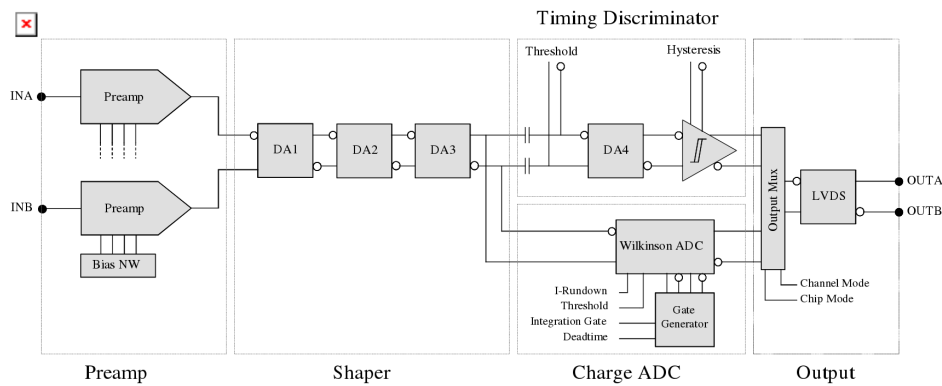
Figure 2.8: Scheme of the MDT frontend electronics [17]

2.2   Limitations of the MDT muon detectors

Up to a certain hit rate the ATLAS MDT detectors perform very well, providing a precise muon track measurement better than 100 μm all over their large surface. Nevertheless there are intrinsic rate limitations of the technology.

1. The maximum electron drift time for ionizations close to the tube walls lies around 700 ns. A muon crossing the tube close to the central wire generates primary electrons over the whole radius range. Therefore a 800 ns deadtime is applied by the electronics after each hit, to prevent the generation of multiple hits from a single muon due to those additional electrons. If another particle crosses the tube during that time, the electrons arriving within the deadtime will not generate a new hit, and its drifttime cannot be reconstructed.

   This behavior has been investigated with a Mezzanine card and periodic signal stimulus by an arbitrary waveform generator and a coupling capacitor, using the circuit in figure 2.9. As long as the time in between stimuli is smaller than the sum of an adjustable and an additional constant intrinsic deadtime, the output follows the input with slope one. For stimuli faster than the total deadtime, every second input pulse is missed. See figure 2.10 for the results on this measurements. The effective deadtime varies between 201 ns and 813 ns, depending on the setup configuration. Naturally for events that follow a non-uniform but poissonian distribution, events will begin to get lost well below the deadtime threshold.

   Be τ the electronics deadtime following an accepted hit, R the true hit rate, and R_m the measured hit rate, including lost hits due to the preceding hits deadtime. A hit during the deadtime does

not extend the deadtime, accordingly it is just ignored. Assuming a poissonian distribution for the hits, the true hit rate calculates [16] from the measured hit rate as

$$R = \frac{R_m}{1 - \tau R_m} \tag{2.2}$$

or for R_m as a function of R

$$R_m = \frac{1}{\frac{1}{R} + \tau} = \frac{R}{1 + R\tau} \tag{2.3}$$
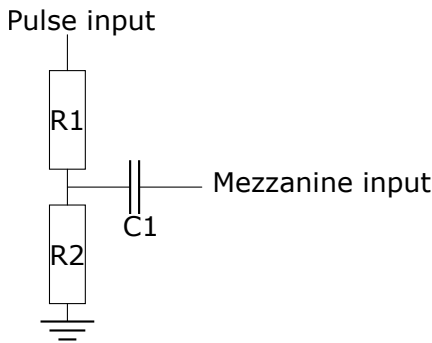
Figure 2.9: Schema of the circuit to induce defined charge pulses into the mezzanine card frontend electronics. R1 and R2 form a voltage divider with a sum of 50 Ohms to terminate the input signal properly. The charge induced is defined by the height of the voltage pulse and the value of the coupling capacitor C1.
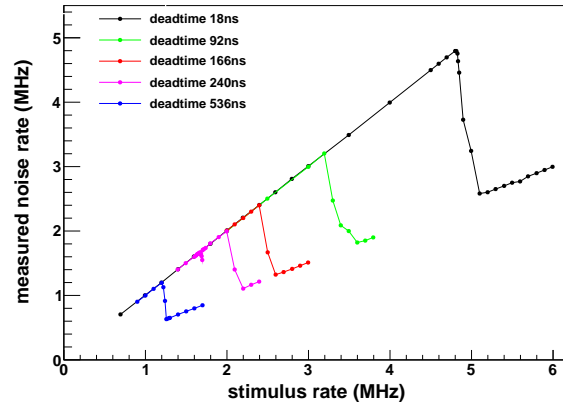
Figure 2.10: Detected input rate vs. stimulus input rate for a MDT mezzanine card with periodic signals, injected via capacitive coupling to one input channel. Different deadtime configurations result in different cutoff frequencies, beyond every second input pulse is not recognized by the electronics.

2. The nominal gain factor for the electron amplification close to the anode wire of the MDT tubes is 2×10^4. As the number of primary electrons created by a minimal ionizing particle is around 300 per cm at 3 bar absolute pressure, the electronic signal induced on the wire and fed through the amplifier stages is large enough to cross the threshold voltage and the hit is detected. The equivalent amount of positive ions generated close to the central wire in the amplification region needs to cross the tube in opposite direction as the electrons, to be neutralized at the tube wall as illustrated in figure 2.11. As the drift velocity of the ions is much lower than the electron drift velocity, this takes about 4 ms for tubes with 3 cm diameter.

During this time, the ion charge distorts the electric field within the tube, shielding the area outside the expanding ion ring. At tube radii intervals, where the rt-relation is not linear, the drift velocity is depending on the electric field, and thus temporarily not in agreement with the nominal rt-relation. This leads to a degradation of spatial resolution in these areas at the presence of space charge. As for 30 mm MDT chambers, the non-linearity is most distinct for radii r > 7 mm, here the effect on the spatial resolution is increasingly significant for hit rates above few hundred Hz/cm^2. This behavior has been investigated within the CERN Gamma Irradiation Facility (GIF) see figure 2.12.

3. The above mentioned shielding effect of the ion cloud produced at high hit rates also affects the avalanche electron multiplication at the anode wire. The higher the hit rate, the lower the
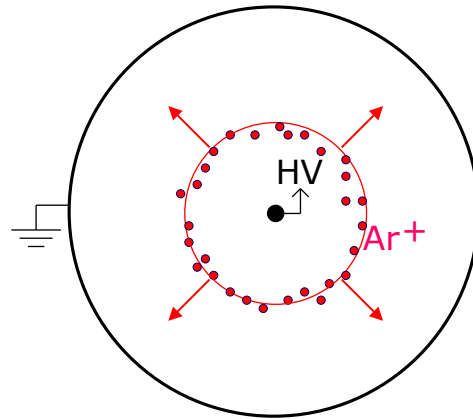
Figure 2.11: Slow drifting ion ring as remnant of the avalanche ionization process close to the central high voltage wire.
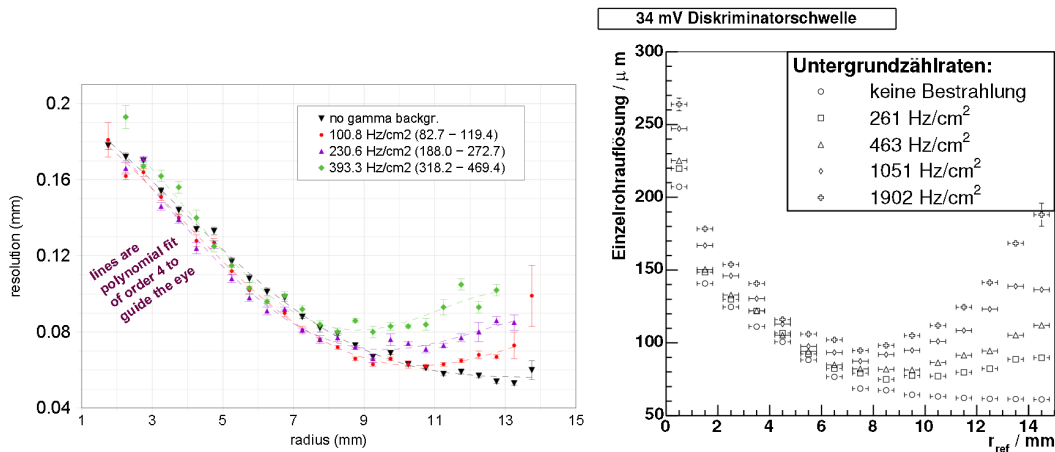
Figure 2.12: Degradation of the MDT spatial resolution with irradiation rate, tested during different irradiation campaigns within the CERN Gamma Irradiation Facility (GIF). The left plot shows the result for a MDT single tube spatial resolution for high energy muons, using a barrel MDT chamber for the reconstruction of the reference track [18]. The right plot shows similar MDT resolution results from the GIF, where silicon strip detectors were used to measure the muon reference tracks [19]. Both measurements show the degradation of spatial resolution with increasing gamma irradiation rate, especially for large radii > 7.5 mm.

gas amplification, and thus the electronic signals on the ASD chip. Signals passing the wire at small distances tend to be overall small as fewer primary electron participate in the signal beginning [20], as illustrated in figure 2.14. Here the gain reduction effect has the largest impact, as the low signals might not cross the electronics threshold anymore.

In addition the rise time of the analog signal has a finite value of 15 ns [13], so lower signals lead to a delayed crossing of the ASD discriminator threshold, see figure 2.13. This effect is called time slewing and is discussed in detail in chapter A.1.4.
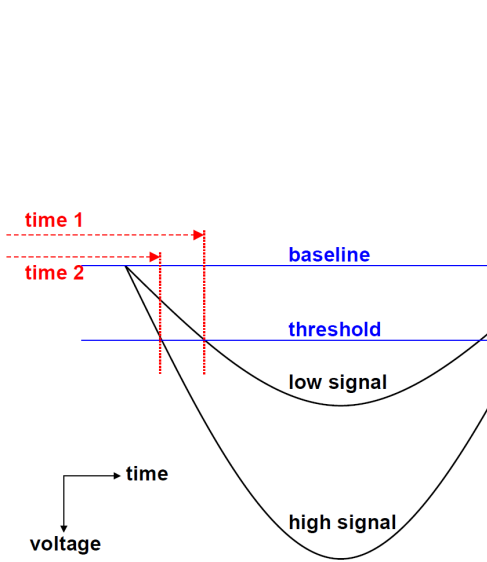
Figure 2.13: Time Slewing effect for small signals, compared to a (fixed) discriminator threshold. Signals with low amplitude tend to be detected later than high signals [21].
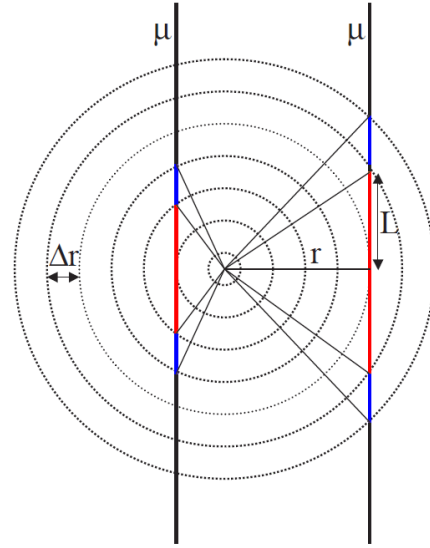
Figure 2.14: Geometric explanation for smaller signals at small drift radii. For tracks close to the wire, the charge clusters arrive scattered in time, resulting in a low and broad signal. Electron clusters from tracks far from the wire concentrate in time, resulting in a large and short electric signal [21].

Up to the first long shutdown period of the LHC in 2013 and 2014, the accelerator delivered luminosities of several 10^{33}cm^{-2}s^{-1} to the ATLAS experiment. The average hit rate within all detectors has also been measured. Figure 2.15 shows hit rate values for the small wheel detectors at an average luminosity of 10^{33}cm^{-2}s^{-1} and $\sqrt{s} = 8$ TeV. The hit rates for the innermost MDT tubes reach up to 40 Hz/cm^2, which is well below the rates, that cause a decrease of tracking resolution as indicated in figure 2.12. The discrepancy in between simulation and measurement lies within the boundaries that were shown in figure 1.16 in chapter 1.4.

Nevertheless if these rates are extrapolated to the luminosities, that are expected as a result of the future LHC upgrades, parts of the small wheel MDT systems see hit rates above their capabilities. Picking an example luminosity value of 3×10^{34}cm^{-2}s^{-1} and $\sqrt{s} = 14$ TeV, the expected hit rates are summarized in figure 2.16. The yellow box indicates the maximum tolerable rate of 200 to 300 kHz/tube. In this case, not only the CSC detectors within the inner part of the small wheels, but also the MDT systems for radii in between 200 and 300 cm suffer from the high hit rate.

With decreasing spatial resolution, the tracking efficiency of the MDT chambers deteriorates as well. Figure 2.17 shows the resulting muon efficiency for a single layer of tubes (solid), and for a chamber of two multilayers with 4 tube layers each, as a function of the hit rate per tube. At luminosities beyond the design value, the chamber tracking efficiency shows a rapid decline down to unacceptable
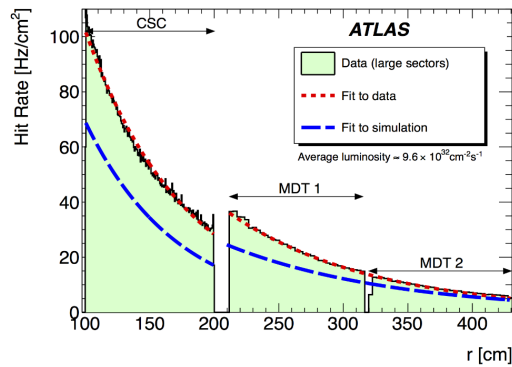
Figure 2.15: Measured hit rates in the small wheel tracking detectors during a run with an average luminosity of 10^{33}cm^{-2}s^{-1}. The jump of rate in between MDT and CSC measurements is caused by chamber efficiency to background hits. The measured rate lies above the value of an initial simulation. [8]
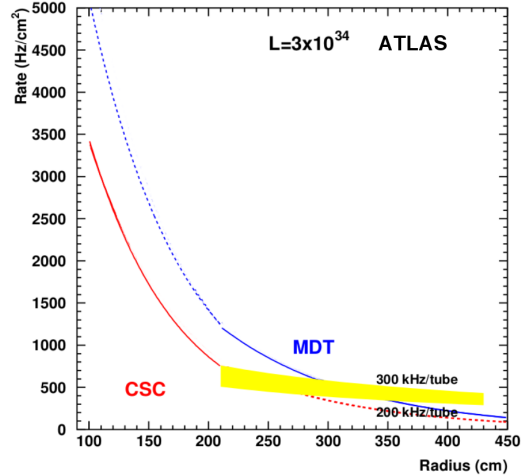
Figure 2.16: Small Wheel hit rates, extrapolated to a luminosity of 3×10^{34}cm^{-2}s^{-1} and $\sqrt{s} = 14$ TeV, which lies within the expected values of future ATLAS operation. For radii between 200 cm and 300 cm the rate is well above the MDT capabilities [8].

values.

In summary, the MDT detector technology chosen as tracking system for most parts of the ATLAS muon spectrometer works well and reliably for particle hit rates up to values expected at LHC design luminosity. Even after future luminosity upgrades, the MDT chambers in the ALTAS barrel section and the outer end caps will perform well. Only the MDT chambers within the small wheel stations will be stressed beyond their capabilities, and will therefore be replaced.

2.3   sMDT design criteria

All the limitations of the MDT detector design at high irradiation rates mentioned in the last section, can be massively reduced by a reduction of the tube diameter from 30 mm to 15 mm. This section covers the advantages of detectors built from small Monitored Drift Tubes (sMDT) compared to 30 mm tubes.

With a reduction of the outer tube diameter to 15 mm and keeping the same mechanical construction, including the 400 μm wall width, the active tube radius is reduced to 7.1 mm. This has several consequences on the performance of a single tube.

1. The maximum drift time for electrons is reduced by a factor of about 3.5 to ~180 ns, allowing a reduced deadtime configuration for the chamber electronics, intrinsically reducing the occupancy and increasing the rate-capability of the tube.

2. As described in section 2.2, the negative effect of space charges on the detector resolution is most present for radii with non-linear rt-relation (resulting in a non-constant electron drift velocity). As the rt-relation below 7.1 mm is relatively linear, space charges present at high hit rates affect the spatial resolution less (see figure 2.18).

3. The ion drift time is reduced by a factor of four, down to a value of around 1 ms, reducing the presence of space charges even more.
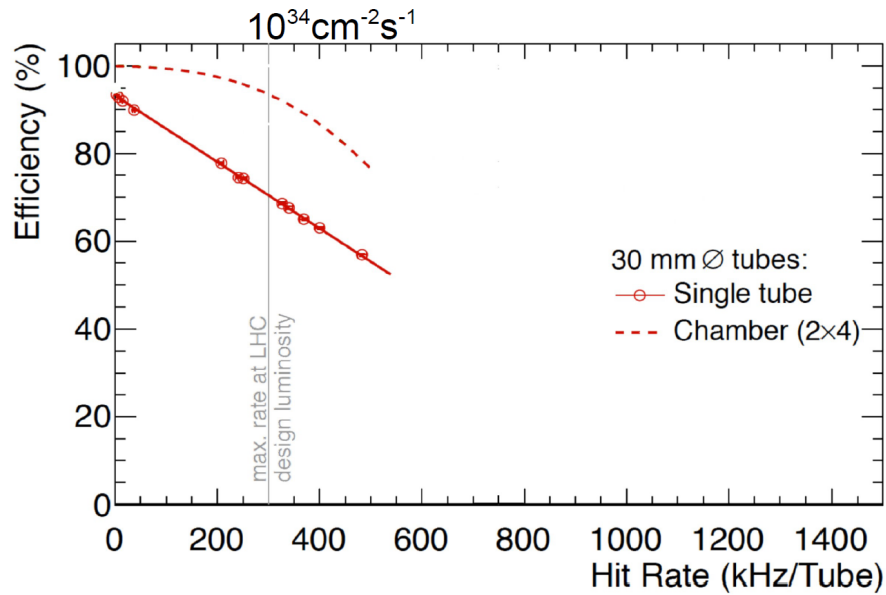
Figure 2.17: Reduction of tracking efficiency for a 2x4 layer MDT chamber with increasing hit rates. Data are taken from test beam measurements. The line indicating "max. rate at LHC design luminosity" is referred to an instantaneous luminosity of $1 \times 10^{34} \mathrm{cm}^{-2}\mathrm{s}^{-1}$ [8].
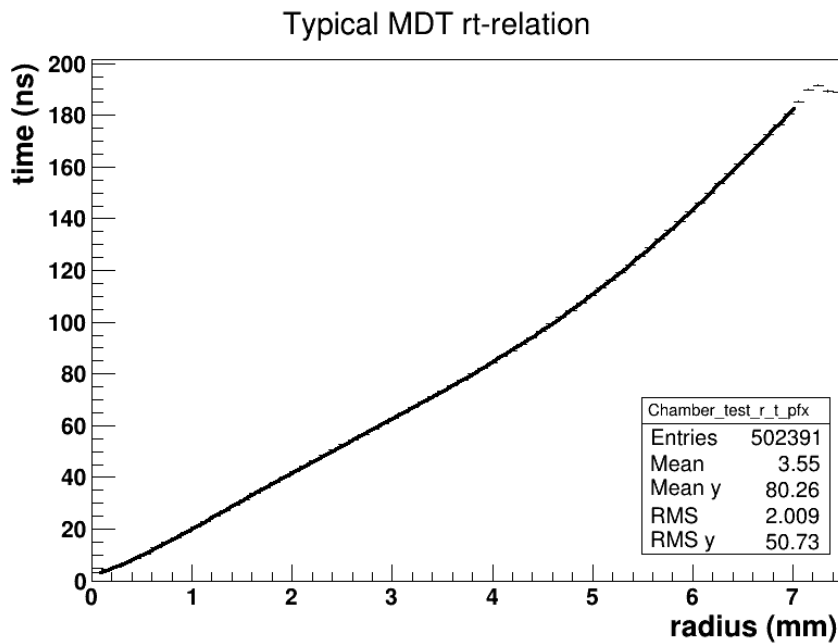
Figure 2.18: Mostly linear rt-relation of 15 mm diameter sMDT drifttubes.

4. Cutting down the tube radius to one half also reduces the effective area of a tube of same length by a factor of two. At a given areal hit rate, this results in half the hit rate per tube. Together with the above mentioned factor of 3.5 due to reduced drift time, the effective reduction factor in occupancy is 7.

To keep the electric field configuration and gas gain unchanged, the nominal high voltage for sMDT tubes needs to be reduced with respect to 30 mm tubes, according to equation. 2.1. Table 2.1 summarizes operational and constructive parameters for MDT and sMDT tubes.

	30 mm MDT	15 mm sMDT
Anode wire diameter (μm)	50	
Drift gas composition	Ar:CO_2 93:7	
Absolute pressure (mbar)	3000	
Inner tube radius (mm)	14.2	7.1
High Voltage (V)	3080	2730
Maximum electron drift time (ns)	680	180
Maximum Ion drift time (ms)	4	1

Table 2.1: Operational parameters for 30 mm MDT and 15 mm sMDT tubes

Figure 2.19 overlays measured drift time spectra for MDT and sMDT tubes. Up to 180 ns both distributions are equal, but the sMDT spectrum excludes the non-uniform distribution for large drift radii, indicating a field-dependency of the drift velocity.
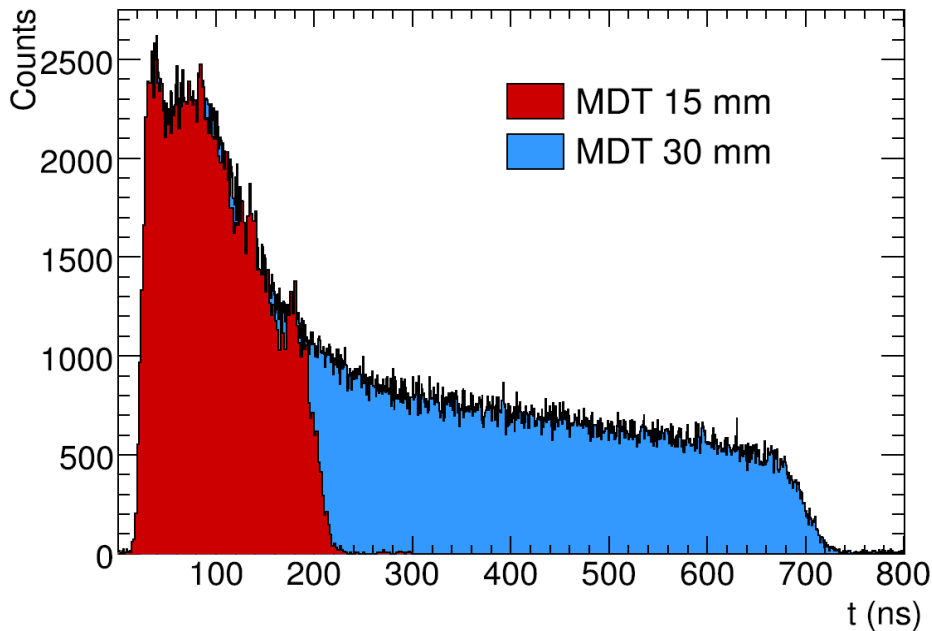
Figure 2.19: Overlay of typical drift time spectra of 30 mm MDT and 15 mm sMDT drifttubes [22].

Several sMDT prototype chambers of different size - up to the full size of a potential inner chamber for an upgraded ATLAS Small Wheel - have been built [22] and tested intensively in muon test beam conditions and high-rate irradiation with γ-particles [23]. These measurements clearly show the expected positive effects on occupancy, resolution and efficiency, which are also in agreement with GARFIELD [24] simulations.

Figure 2.20 shows results on sMDT measurements within the CERN Gamma Irradiation Facility (GIF). A multiple layer chamber was irradiated by 662 keV γ particles emerging from a ^{137}Cs, while triggering the readout electronics by cosmic muons. The radius measurements of the irradiated layers were compared with reference tracks, fitted onto the measurements of unirradiated layers. Efficiency is defined by the percentage of cosmic muon hits where the position of the muon passage measured by the irradiated layers lies within a certain window around the reference track. The figure also shows the performance of 30 mm tubes for reference, as well as a calculation of the tracking efficiencies where at least a certain number n of a multilayer chamber with m tube layers must match the criteria.
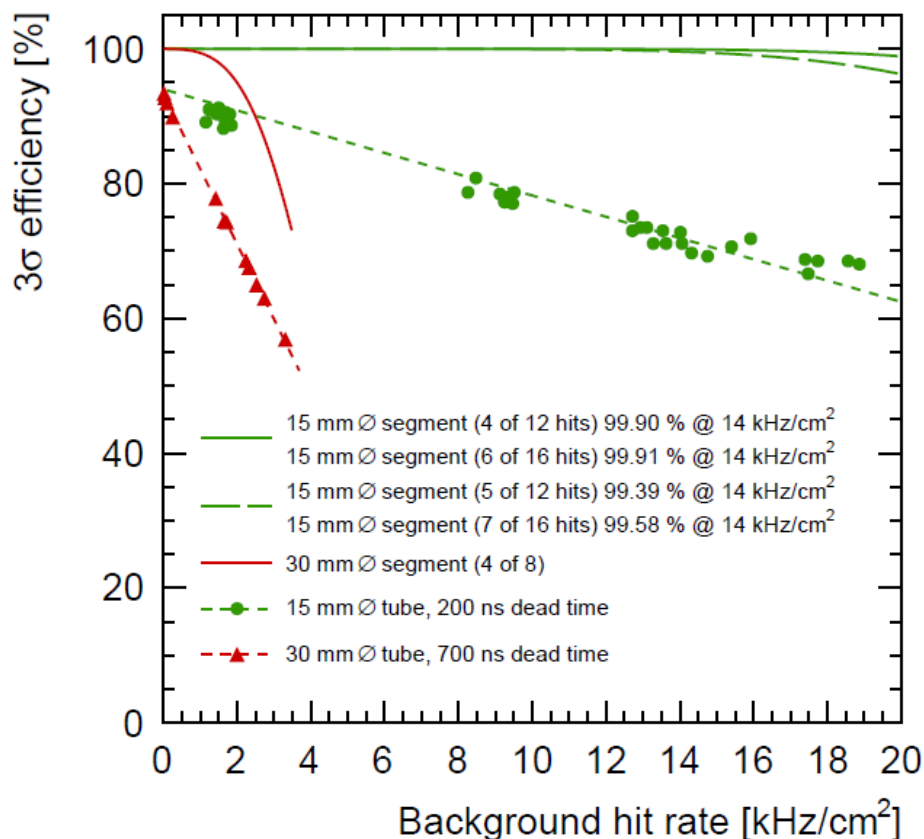
Figure 2.20: Tracking efficiency for 30 mm and 15 mm tubes at increasing rates for single tubes and chambers, measured under γ irradiation at the CERN GIF facility [23].

As the mean energy of cosmic muons lies around 4 GeV [25], with broad side bands towards higher and lower energy, scattering of low-energy muons within the detector material has a negative influence on the measured resolution and efficiency.

Measurements within the CERN SPS H8 beam line with 140 GeV muons match better the scenario of a high-energy experiment like the LHC. The SPS beam lines also were the testing environment for several of the present ATLAS systems.

Muons there are produced by the decay of pions, emerging from a target irradiated by the 450 GeV SPS primary proton beam. The spatial resolutions in figure 2.21 were obtained by exposing a 16-layer sMDT prototype chamber to these high-energy muons.

The particle flux background within the ATLAS cavern not only includes γ-particles, but also high-energy protons and neutrons [9]. The investigation of the sMDT detectors response on these is not covered by the measurements mentioned above. Nevertheless this is necessary, as the ionization of
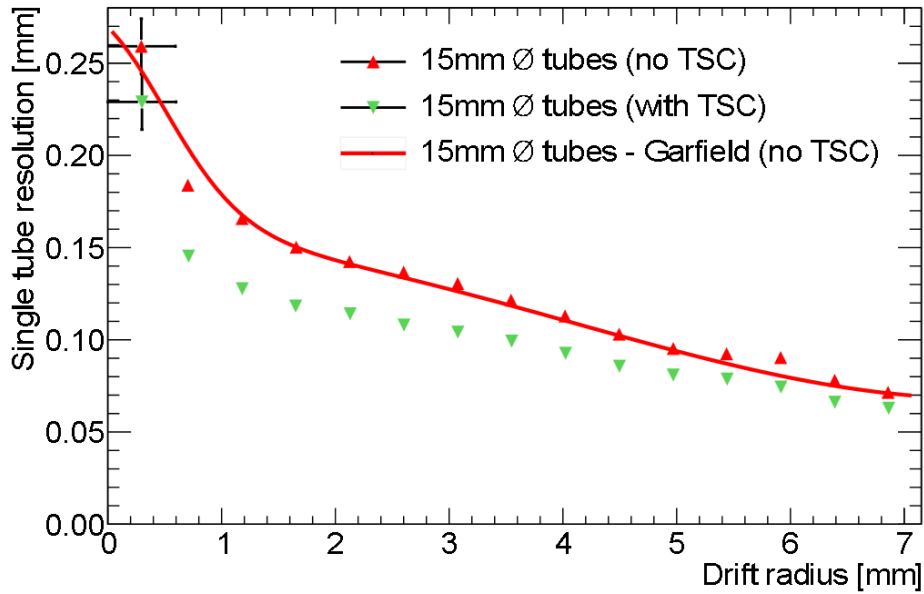
Figure 2.21: Spatial resolution of a sMDT prototype chamber measured at the CERN SPS H8 beam line, using 140 MeV muons [23]. The term TSC refers to time slewing correction, described in appendix A.1.4.

γ-particles differs from the evenly and densely distributed electrons created by protons or by nuclei from neutron recoils.

Therefore a special designed sMDT prototype has been investigated under proton and neutron irradiation at the Tandem facility of the Meier-Leibnitz-Laboratory in Garching, Germany. The following chapters cover these measurements, as well as simulations and results.

The sMDT technology was considered and developed for the ATLAS New Small Wheel upgrade, motivating the studies of this thesis.

In early 2012, the ATLAS muon community decided in favor of Micromegas detectors and small strips Thin Gap Chambers (sTGC) as an alternative choice to be used for the New Small Wheels. Nevertheless, several sMDT chambers will be installed within the ATLAS experiment, covering areas of the muon spectrometer that are uninstrumented or poorly covered so far.

2.4   MLL tandem accelerator facility Garching/Munich

This section describes the tandem accelerator facility of the Meier-Leibnitz-Laboratory, located in Garching, Germany, built in 1970 and continuously expanded since then. In this work it was used to provide high-rate proton and neutron irradiation environments, to investigate detector pulse shapes and muon tracking detectors under these conditions.
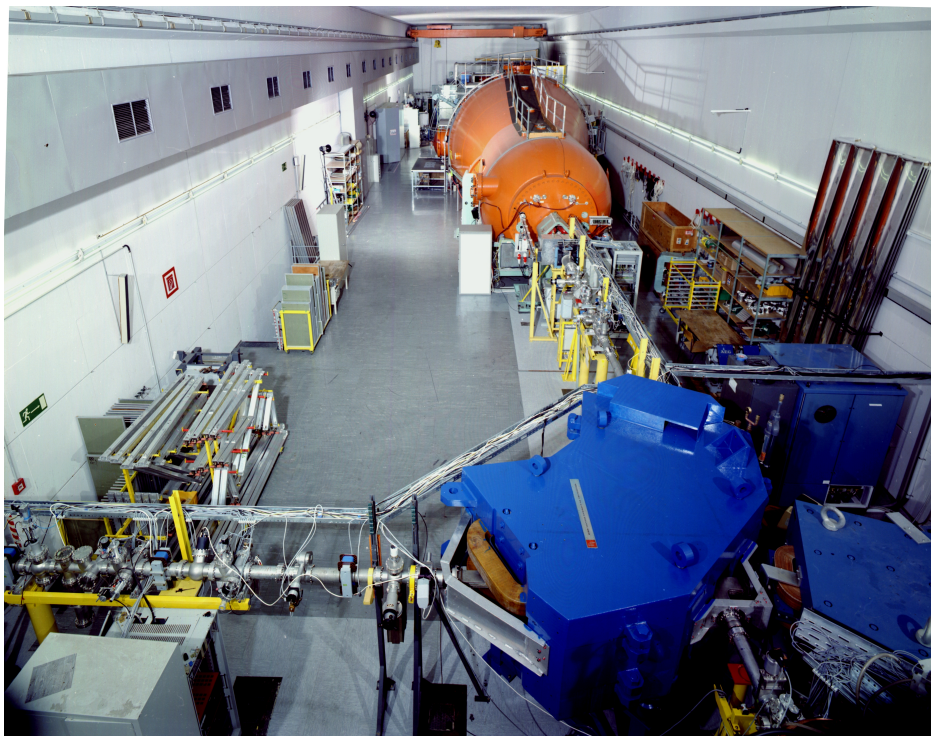
Figure 2.22: The Tandem accelerator hall with the main pressurized accelerator tank (orange), and the analyzing magnet (blue) for ion charge selection and energy stabilization.

The main component of the accelerator is a 25 m long tandem tank, operatable at up to 15 MV terminal voltage. It accelerates charged particles using a static electric field. Due to the two-staged acceleration with the help of a thin stripper foil it is possible to produce e.g. protons of up to 30 MeV. This is achieved by removing electrons from negatively charged ions at the intermediate step for an additional repelling acceleration within the second half of the accelerator, as pictured in figure 2.23. Using this static chain, it is possible to generate high-energy protons or ions at very high rates of up to several μA of DC beam current.

An additional pair of magnet coils, driven by a function generator and current power amplifier, allows to wobble the beam in the horizontal axis at high frequency. During the sMDT measurements, it was driven at a rate of 628 Hz, resulting in an effective beam spot size of 7 x 0.5 cm^2 at the detector surface. The wobbling frequency is limited by eddy currents induced in the beam pipe, which reduce the field strength experienced by the protons.

Figure 2.24 shows the effective proton beamspot without and with wobbling, which is visible due to the temporary installation of a transparent and scintillating tile after the thin Kapton[1] exit window in the center of the end flange of the accelerator.

The beam was wobbled using a symmetric sawtooth function. Completing one period took 1.59 ms, and the beam width was around 2 cm, occupying already 28 % of the beam window. Together with

---

[1]Kapton is a polyimide film developed by DuPont and is a registered trademark
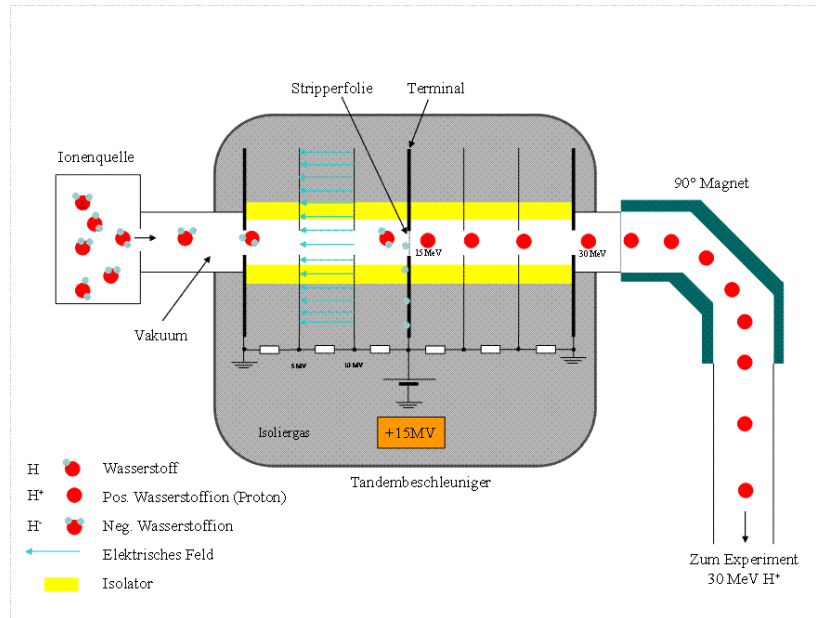
Figure 2.23: Illustration of the two-staged acceleration process by removing (stripping) electrons of the nuclei at the intermediate acceleration step. [28]
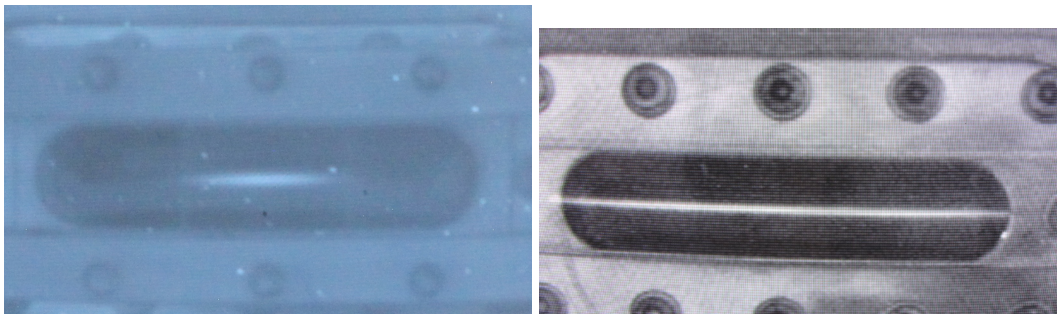
Figure 2.24: Proton beamspot without wobbling at the experiment location, visualized by the illumination of scintillation material (left). The steady beamspot is already intentionally de-focused in the horizontal axis to a width of 2 cm. The right image shows the effective beamspot with activated wobbling, resulting in a full-width irradiation along the flange window.

an ion drift time of 1 ms, there is only a short time during the wobbling cycle, where not the complete irradiated area contains drifting ions. This happens during the turning point of the beam spot at the edges of the irradiated area. The total coverage with ions over time, and with this the probability for a muon to suffer from the space charge effects is above 94 %, as explained in figure 2.25.
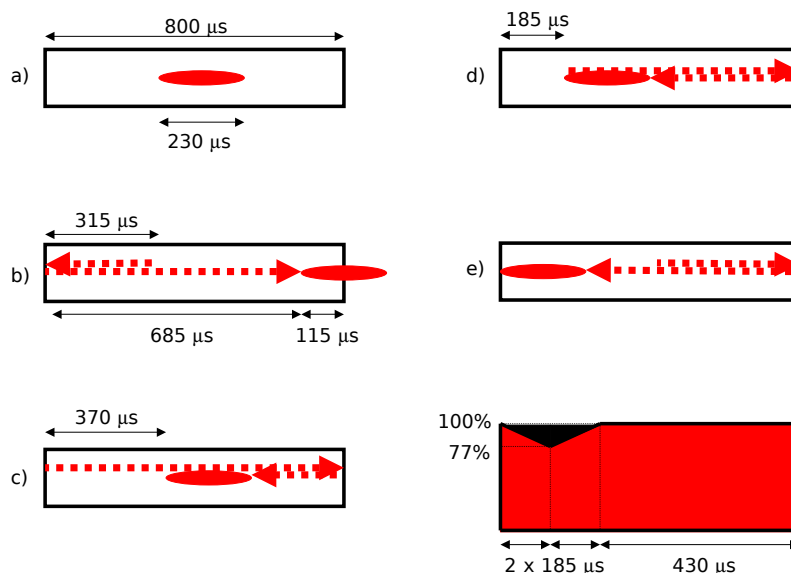
Figure 2.25: Illustration of the irradiated areas coverage with ions causing space charge effects. All sizes are transformed into times for a constant beam spot movement of 628 Hz. The dotted area is the tail of ions with 1 ms length. a) Size of the beam window and beam spot in the time domain. b) Beam spot turning point on the right border. c) Beginning of the time interval without full ion coverage. d) Transition from growing to shrinking unirradiated area. e) Full coverage with ions again. The lower right plot width corresponds to a half period of the beam movement. The red area represents the probability of a cosmic muon to hit a tube section under the influence of space charge, whereas the black triangle corresponds to the small gap in the ion effect. The total ion coverage over a full wobble cycle is greater than 94 %.

It has to be mentioned, that this irradiation pattern is different from a completely random position of irradiating particles at the same rate. Since the protons enter the detector at very close distance to the previous one, the space charge effects in between them are maximized.
The beam guiding system of the accelerator features a set of three available beam absorbers that are made of micro perforated metal plates that are insertable into the beam. These absorbers have a geometric absorber-to-hole ratio of 1000, 1000 and 33. Combinations of these filters result in a rate higher than expected by plain multiplication of the absorption values, because a second micro hole in the path of an ion due to geometric overlap does not reduce the particle rate any further. Nevertheless it is possible to reduce the beam currents down to a level of kHz with help of these devices in spite of a larger necessary current that is needed to operate the accelerator at stable conditions.

2.5   15 mm sMDT chamber irradiation with 20 MeV protons at high rate

This section describes the proton irradiation measurements on a 46-tube sMDT prototype chamber, performed in September and October 2012. The chamber has been constructed by Max-Planck-Institute Munich (MPI), and the measurements have been performed in collaboration.
Detailed descriptions on the used analysis methods are discussed in the appendix A.1.

During the beamtime, several different proton irradiation rates have been set up, and it was possible to take the data sets at a cosmic muon trigger rate around 1 Hz. The focus was put on irradiation rates within the expectation of High Luminosity LHC (below 20 kHz/cm^2, including safety factors), therefore the measurement points in the lower end of the rate spectrum were allowed to gather more statistics than the ones on the higher end.

To determine the proton rate, a scintillation counter has been placed temporarily in front of the sMDT detector. Its output pulses have been counted by a CAEN NIM scaler module N1145.

date	proton rate (kHz)	proton flux density (kHz/cm^2)	number of muon triggers
2012/10/02	0	0	94311
2012/10/10	20	1.9	32473
2012/10/06	60	5.7	56388
2012/10/07	100	9.8	57045
2012/10/05	160	15	86223
2012/10/08	200	19	61712
2012/10/09	330	31	12281
2012/10/08	1400	133	16083
2012/10/08	2800	266	10807

Table 2.2: List of runs taken within the tandem accelerator beamtime in fall 2012. The measurement points up to 31 kHz/cm^2 are relevant for the investigation of space charge effects, whereas the measurement points at 1400 and 2800 kHz absolute value were taken to determine the influence of high trigger rate values on the sMDT chamber electronics.

2.5.1 Detector and trigger layout

Picture 2.26 shows a schematic layout of the investigated detector, as well as the segmented scintillation counters that were used to trigger on cosmic muons that cross the sMDT chamber.
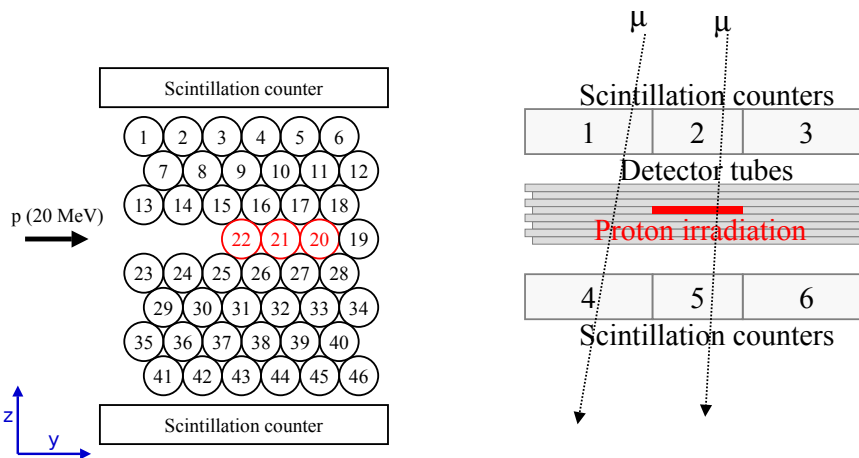
Figure 2.26: Schematic side view on the detector tubes and numbering scheme (left) and segmentation of the trigger scintillators (right). The red area illustrates the irradiated section of the fourth tube layer. The central scintillators have a width of 7 cm, the outer ones 10 cm each.

The detector is made of eight layers of sMDT tubes, six tubes deep each. Only one layer was irradiated by protons, with the other seven layers providing a precise reference track prediction for cosmic

muons.

The irradiated fourth layer is missing the two leftmost tubes for proton accessibility, but in fact short dummy tubes were glued in, to preserve mechanical stiffness of the chamber. These dummy tubes do not extend to the central, irradiated part of the detector (see figure 2.29). Using this geometry, the first tubes hit by protons (Numbers 22, 21 and 20 in figure 2.26) are fully covered by the acceptance of the reference layers above and below. This allows for the investigation of muon tracks through the irradiated tubes at full geometric acceptance for cosmic muons.

Figure 2.26 also shows the three-fold segmentation of the trigger scintillators along the tubes. As the signal of each scintillator was also recorded using a Time-to-Digital-Converter (TDC) module, it is possible to identify the scintillators hit. This allows to distinguish between muons, that either passed through the irradiated region of the tubes within the fourth layer (like the combination of signals from scintillator two and five) or not (like the combination of the scintillators one and four).

This information allows to separately investigate the irradiated tube performance for effects that depend on either only the absolute hit-rate (unirradiated sections), or both the hit-rate and the space charge effects (irradiated section). This separation becomes important for the reduction of detector efficiency with increasing hit-rate.

Figure 2.27 illustrates the hit-distribution for the nine different possible pairwise combinations of the six scintillators. The "Road ID" is defined by the scintillator hit combinations in figure 2.28.
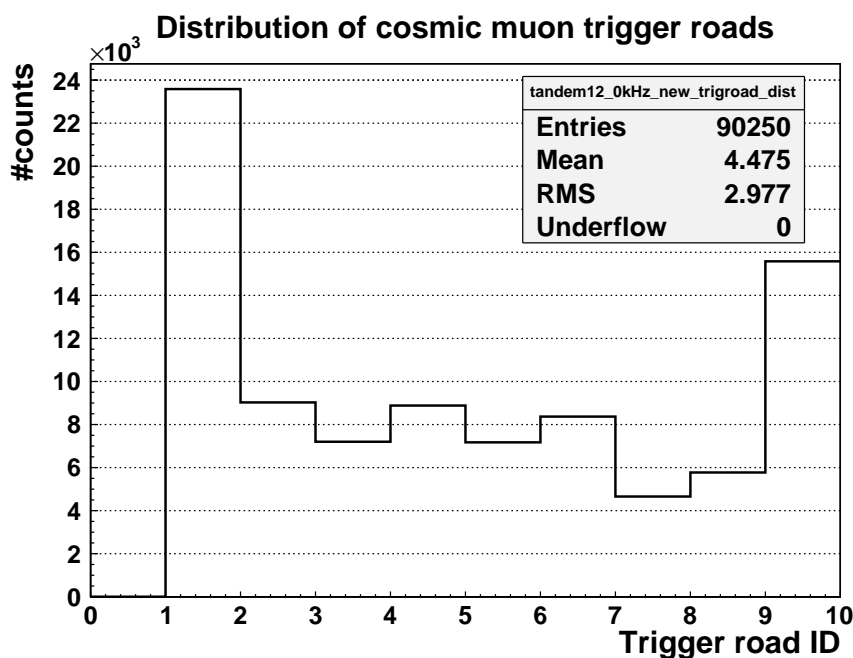
Figure 2.27: Distribution of the different possible upper and lower scintillator combinations

Road IDs one and nine are favored, due to the larger area and thus acceptance of the scintillators one, three, four and six. This also leads to the lower occupancy for road ID five, which uses small width scintillators only.

Trigger road IDs three and seven also utilize large scintillation counters, but are geometrically limited to non-perpendicular cosmic muon tracks. Since the impact angle of cosmic muons roughly follows a $\cos^2\theta$ distribution [25], the occurrence of these IDs is suppressed.

The remaining asymmetric distribution is expected to result from an imperfect geometric alignment of the scintillators. The high voltage supplies for the six photomultiplier tubes attached to the scin-

tillating blocks has been tuned individually - nevertheless different qualities of the light guide gluing and variations in between the tubes themselves also account for the asymmetric distribution.

In the following, events in the trigger configuration road three, five and seven will be counted as crossing the irradiated tube section. Trigger roads one and nine define muon hits within the unirradiated tube sections left and right of the irradiation spot. The remaining trigger configurations are omitted, as due to the coarse segmentation it is not possible to determine, whether or not the track coordinate along the tube axis lies within the irradiation spot.
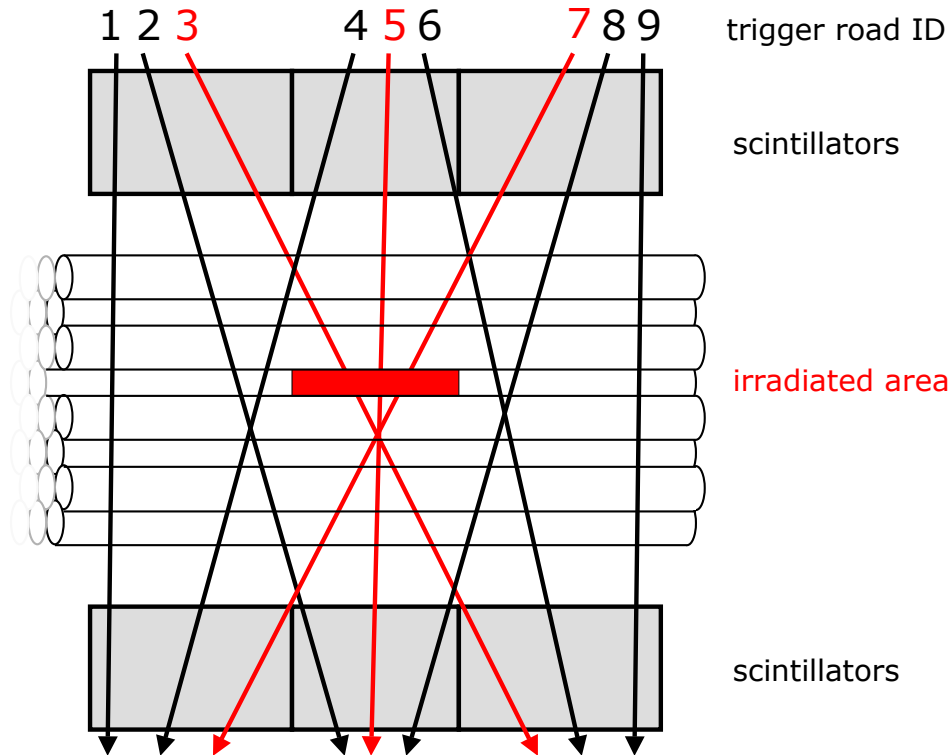
Figure 2.28: Definition of trigger "road" IDs by the combination of hit scintillators. Roads 3, 5 and 7 cover the irradiated tube section of the fourth layer.

Figure 2.29 shows a photograph of the experimental setup with the end of the beam line. Besides the sMDT chamber itself with the cut-out section along the outer tubes of the fourth layer, the triggering scintillators and photomultiplier tubes can be seen, both wrapped in black light-tight insulation tape.

2.5.2   Computer simulation of proton irradiation

For a prediction of the proton range within the detector as well as the ionization within the gas volume of the tubes, it was necessary to perform a numerical simulation for the protons. The program package SRIM-2013/TRIM [29] has been used for the simulation and visualization.

The package supports the composition of different target layers in a planar geometry. The assumption of a planar geometry for the detector tubes is only true for particles hitting the tubes horizontally at half height. For protons that are scattered at an angle, tube wall thicknesses are underestimated and paths within the gas volume are overestimated. Nevertheless this simplified geometry is considered acceptable for a qualitative analysis, as the incident protons hit the detector tubes already horizontally with a vertically moderate sized beam spot below 5 mm of height.

The simulation calculates the path and energy loss of 20 MeV protons passing the different material layers of the detector. This includes a ΔE of 170 keV within 50 μm of Kapton foil, which is the
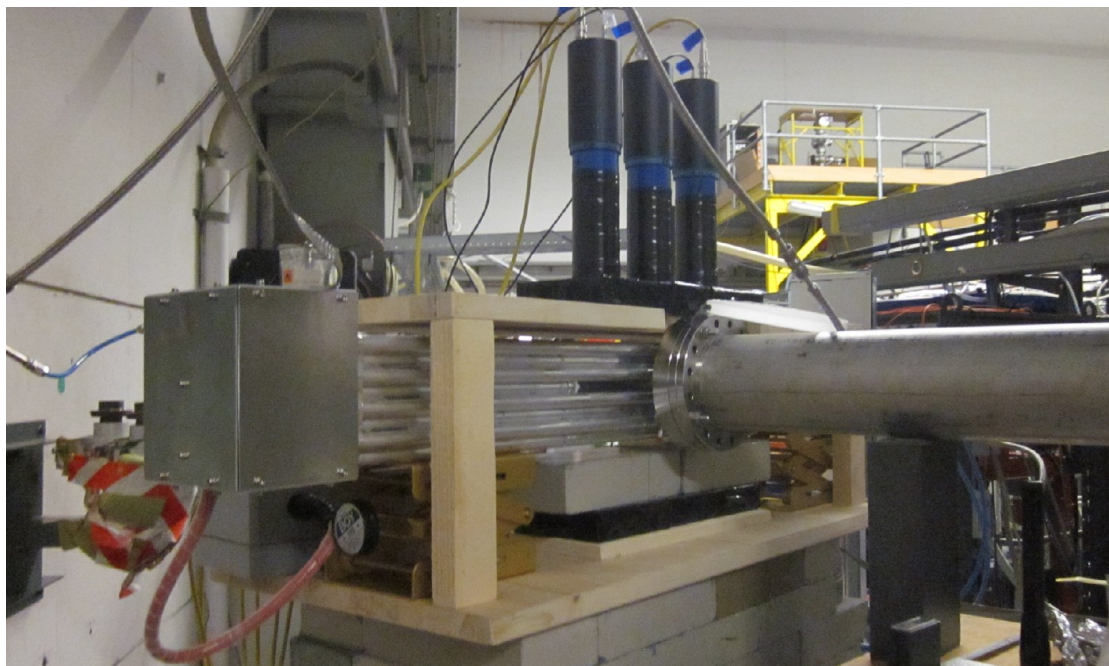
Figure 2.29: The experimental setup, showing the sMDT chamber with its cutout region, trigger scintillators and photomultiplier tubes wrapped in black light insulation tape, and the end flange of the accelerator system. Hidden is the kapton exit window at the end of the beamline.

exit window of the accelerator system, 277 keV in 100 mm of air and then three tubes with 400 μm aluminum wall and 14,2 mm of argon gas at 3 bar absolute pressure. The presence of 7% CO_2 in the gas mixture is neglected. It turned out, that all protons are stopped within three tubes, which is confirmed by the measurements in chapter 2.5.4. Figure 2.30 illustrates several example tracks for protons entering the tubes of the irradiated layer.
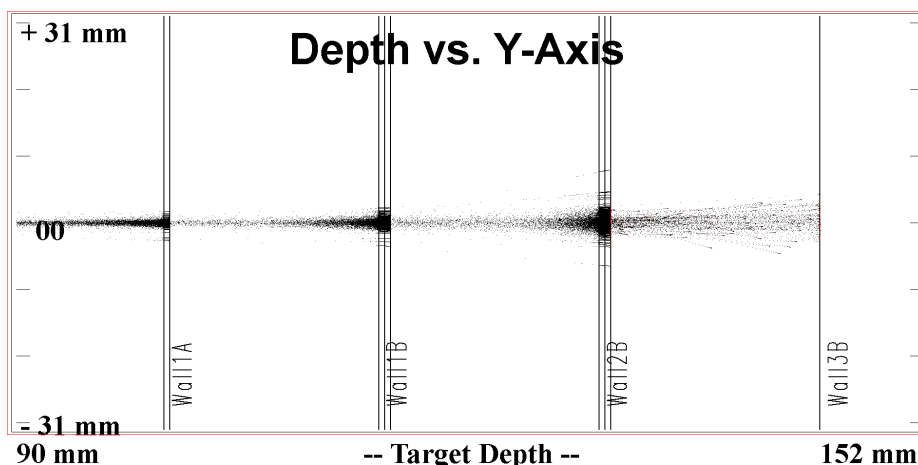
Figure 2.30: Simulated horizontal proton trajectories within the planar geometry of air, aluminum and argon.

The incident protons are mostly stopped either within the entry wall of the third tube, or within its gas volume, as can be seen in figure 2.32. It also shows a close up of the entry wall of the third tube, where most of the proton tracks end.

The series of figures 2.33 illustrates the proton energy loss $\frac{dE}{dx}$ for the different material layers in the order of crossing. Within the air layer and the first two gas layers, the energy loss with target depth is nearly constant. The integral energy loss of the protons within each layer can be calculated by
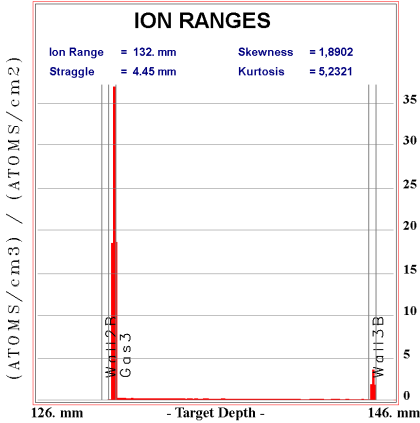
Figure 2.31: Range of the simulated protons. Most protons are stopped within the entry wall of the third sMDT tube. Nearly all of the remaining protons are stopped within the third gas volume, depositing their remaining energy in the active volume of the third tube
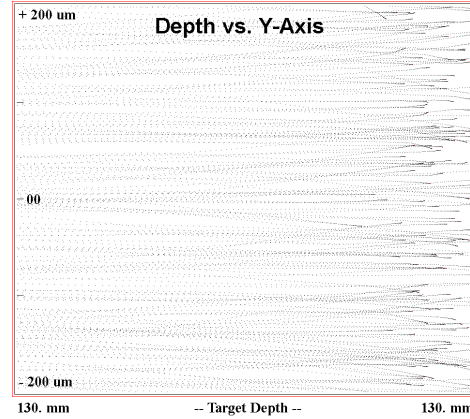
Figure 2.32: Examples of simulated trajectories of protons within the entry wall of the third tube. Most of them are stopped before exiting the wall.

$$\Delta E = \int_{x0}^{x1} \frac{dE}{dx} dx \qquad (2.4)$$

For the regular shapes in the active volume of the first and second tube, this simplifies to the product of mean energy loss value and the target depth.

The protons that are not stopped within the third entry wall lose most of their energy within the third gas volume. The proton hit rate in the third tube is no longer equal to the chamber irradiation rate. In addition the amount of ionization in the third tube is hardly predictable due to the variation of remaining proton energy. This is why the third tube in the irradiated layer is furthermore excluded from the analysis of irradiation effects, and the tubes that are considered irradiated are the leftmost two tubes with the IDs 21 and 22 in the numbering scheme in figure 2.26.

Table 2.3 lists all layer parameters and the energy loss obtained from the simulation. Note, that the energy loss of a muon in the ATLAS experiment is around 25 keV, and the ionization of compton electrons during the irradiation in the CERN Gamma Irradiation Facility reaches up to 662 keV.

The distribution of the remaining proton energy after entering the third gas volume is illustrated in figure 2.34. As most of these are then stopped completely, the ionization energy reaches up to 2.5 MeV, again making this tube incomparable to the other two, where the energy loss lies below 10 % of this value.

2.5.3   Data acquisition electronics and supplies

The 46 tube sMDT test chamber has been designed to be fully compatible to the electronics that the standard ATLAS MDT chambers are equipped with. It therefore makes use of three standard MDT mezzanine cards as frontend electronics, dedicated to the four tubes of the irradiated layer and the upper and lower parts of the detector that serve as reference track layers.

One Chamber Service Module (CSM) is used to read the data from the three mezzanine cards. It is connected to a modified FILAR [30] card within a pc that is running the "mtonline"[2] program package to acquire the events.

The scintillator trigger signals were received by CAEN Discriminator modules N845. Logic modules CAEN N455 were responsible for the OR-link in between scintillators of the same layer, and the

---

[2]Developed by F. Rauscher
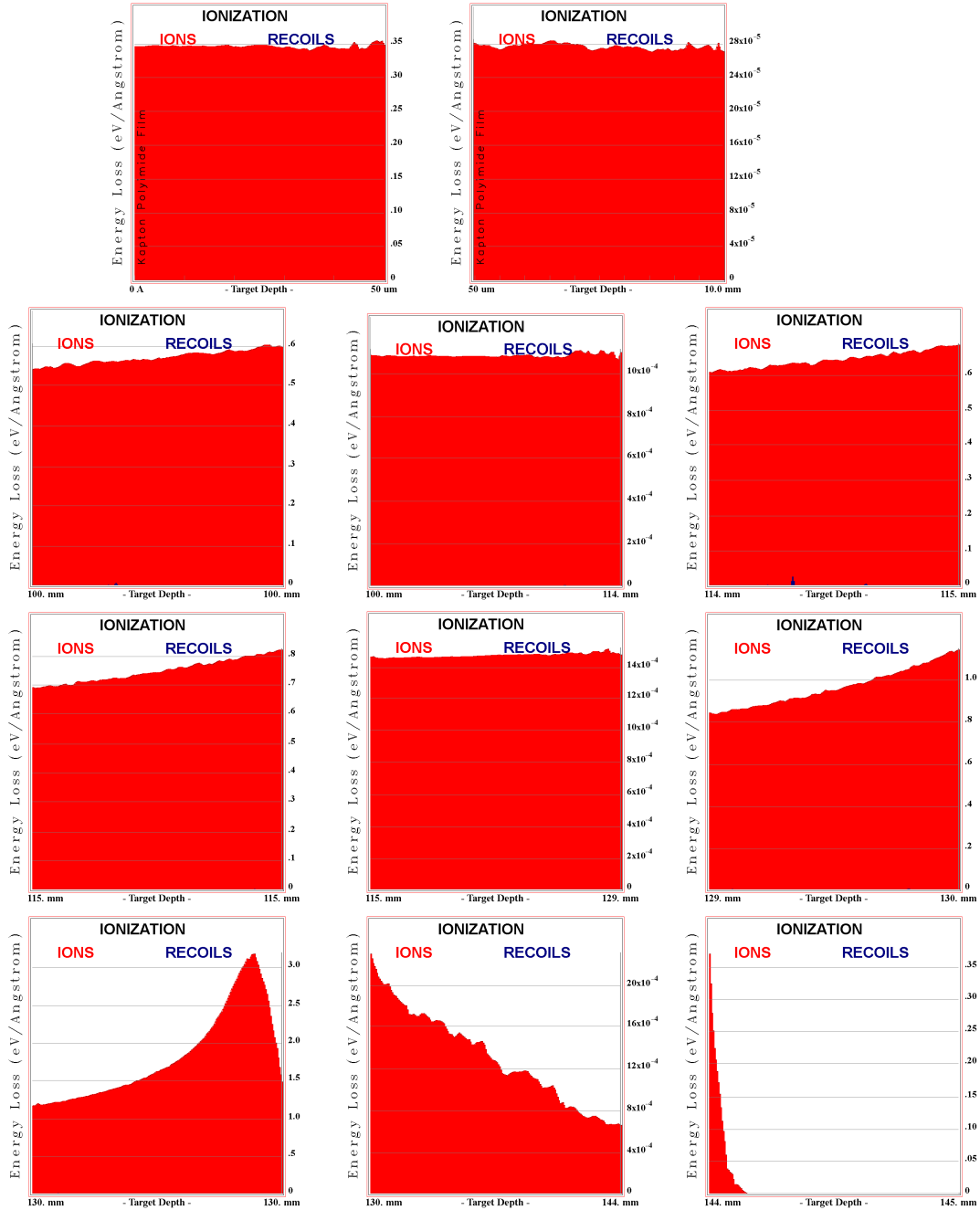
Figure 2.33: Proton energy loss $\frac{dE}{dx}$ for the different detector layers according to simulation. Note the different y-axis scaling. First row includes kapton and air, the following rows include aluminum entry wall, argon and exit wall each.

	thickness (mm)	density ($\frac{g}{cm^3}$)	ΔE (keV)
Kapton	0.05	1.42	170
Air	100	0.0012	277
Aluminum	0.4	2.7	2282
Argon @3 bar	14.2	0.005352	151
Aluminum	0.4	2.7	2568
Aluminum	0.4	2.7	2983
Argon @3 bar	14.2	0.005352	209
Aluminum	0.4	2.7	3850
Aluminum	0.4	2.7	7212
Argon @3 bar	14.2	0.005352	rest
Aluminum	0.4	2.7	rest

Table 2.3: List of simulated detector layers, including their thickness, density and average proton energy loss.
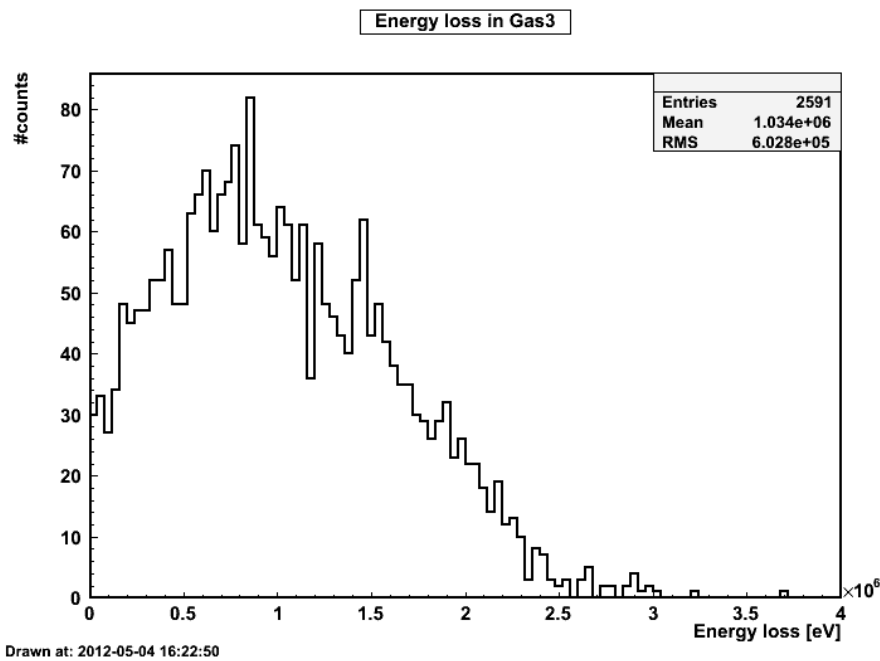
Figure 2.34: Remaining energy distribution of protons entering the third tube, according to SRIM simulations.
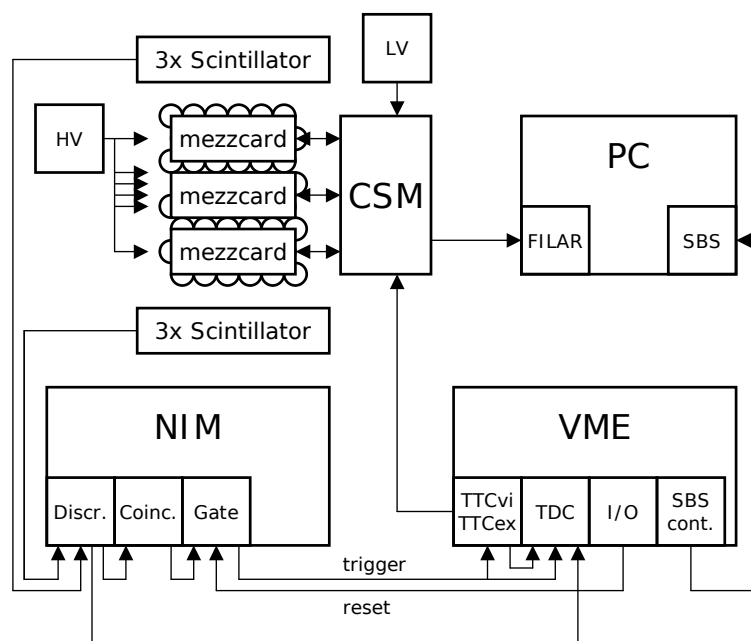
Figure 2.35: Schema of the data acquisition infrastructure used during the measurements.

AND-logic for both layers that forms the final trigger signal. To prevent triggers during data readout from the modules, the trigger signal was fed through a gate unit CAEN N93B, which was set to infinite pulse duration. This prevents the pass-through of further triggers, until the reset signal of the unit is assigned by the readout pc via a VME input/output unit CAEN V977.

High Voltage (HV) for the sMDT tubes was supplied by three Iseg SHQ 224M units, providing six HV channels in total. The four tubes of the irradiated layer were powered independently, whereas the upper and lower reference layers were powered by a single high voltage channel each.

The necessary Ar/CO_2 gas mixture of 93%/7% for the detector was provided by means of a pre-mixed bottle, pressure-regulation valves[3] and gas flow controllers[4].

As the MDT electronic used is designed to measure synchronously with the 40.08 MHz LHC bunch crossing clock, its signal to start drifttime measurements only initiates with the next clock rising edge after the cosmic muon trigger. This adds an uncertainty (jitter) of up to 25 ns. To compensate for this, the time difference in between cosmic muon trigger and the following MDT trigger signal generated by the TTCvi module is also measured by a TDC channel. For details on this correction, refer to appendix A.1.1.

2.5.4 Detector occupancy and signal heights

Figure 2.36 summarizes the track parameters for successfully reconstructed straight muon tracks, with the parametrization $y(z) = a \times z + b$ in the y-z-coordinate system from figure 2.26. The distribution of the track y-coordinate offset b matches well the width of chamber and triggering scintillators. The distribution of the track slope a includes tracks with the maximum geometrically possible angle. The absence of reconstructed tracks around $a \pm 0.57$ can be explained by the geometric impossibility to reconstruct tracks under an angle of 30 degrees with an arrangement of tube layers displaced by half a diameter, as the muon passes all tubes on the same side of the wire,

---

[3] MKS Baratron®
[4] Brooks Model No. 5850

resulting in two ambiguous track fit solutions.

Figure 2.36: Distribution of the reconstructed muon track parameters offset and slope. The irregularity in the left third of the offset distribution matches the missing tubes in this area.

With the chamber being six tubes wide, the expectation for a single tube to be hit by a homogeneously distributed cosmic muon trigger is around one sixth or ∼17 %. This does not include the lower occupancy for tubes close to the chamber edge, where due to geometric constraints the occupancy goes down to one half.

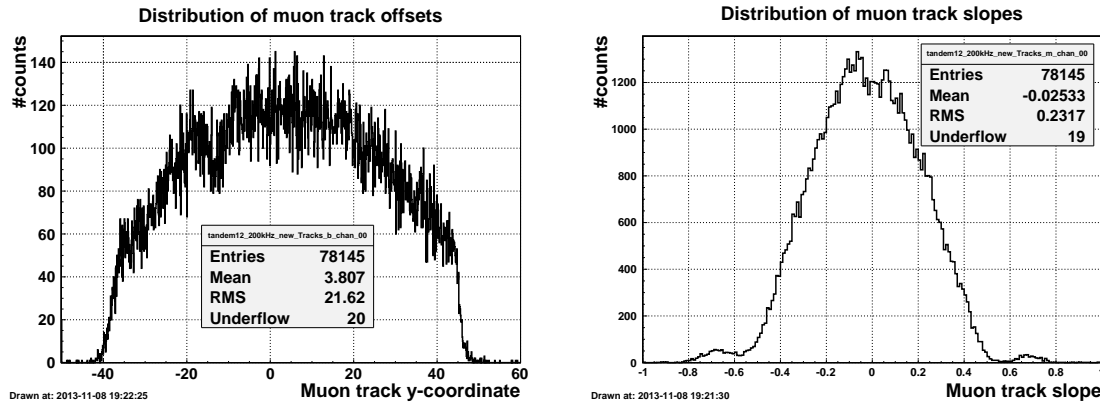Figure 2.37 shows an overlay of the 46 tubes occupancies for all irradiation levels. Tubes on the layer borders show a reduced participation in triggers, due to geometric constraints for inclined muon tracks. Tube number 2 is not equipped with a wire, and therefore shows zero hits. Tube 45 suffers from low efficiency.
The figure shows clearly, that the proton beam hits the fourth layer. The tubes 20 to 22 show an increased participation in cosmic muon events due to the increasing probability for coincidence of a muon trigger and a proton hit in the irradiated tubes. It can be seen, that the adjacent layers directly above and below the irradiated layer (tube 13 up to 28) also show slightly increased hit activity for the higher irradiation datasets. These hits are a result of secondary particles created within the irradiated tube walls, δ-electrons or protons scattered at a very large angle. In addition, aluminum atoms within the irradiated tube walls can become activated by nuclear reactions, which results in unstable aluminum isotopes with short half-lifes, emitting beta and gamma particles.

The increased occupancy of the irradiated tubes through random coincidences of muon tracks with proton hits is also visible in the drifttime spectrum of the irradiated tubes, like in figure 2.38, that shows measured drifttimes for the irradiated tube number 22 at a proton rate of 200 kHz. The drift-time spectrum for the cosmic muons sits on top of a uniform distribution for measured times of uncorrelated proton hits. Nevertheless, this is not a problem for the analysis, as the tracks defined by the unirradiated reference layers defines a radius and thus a drifttime prediction, against which the time measurements of the irradiated tube along the muon track are compared. Random proton hits are in this way effectively sorted out, and only affect the measurement if they precede the cosmic muon hit by less than the electronic deadtime that follows each hit, which in this case prevents the detection of the muon signal.
As mentioned, the MDT electronic not only measures the drifttime for each hit and channel, but also the signal height or, more precisely, the integral charge of the signal rising edge. This information is necessary in the experiment for best tracking performance, to compensate for time slewing effects, which are in detail discussed in appendix A.1.4.
Figure 2.40 shows the measured ADC spectra of tube 22 without and with different proton irradiation.
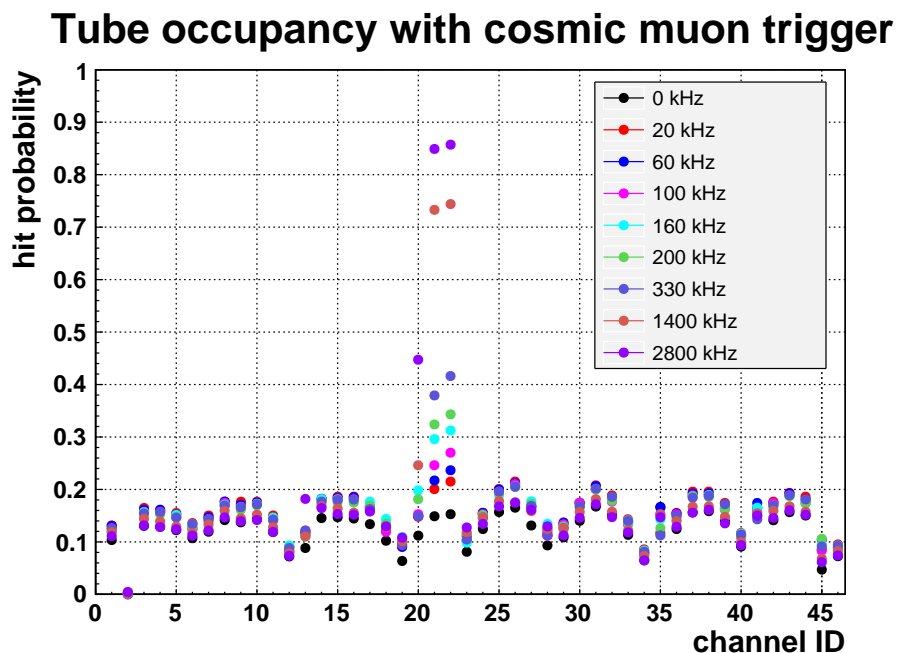
Figure 2.37: Probability for a tube to measure a hit at different proton irradiation levels. At increasing proton hit rate, the probability for a proton hit to occur in coincidence with a cosmic muon trigger rises. Due to the geometric inefficiencies of the chamber on the trigger borders, the plot illustrates also the 6-layer structure of the chamber.
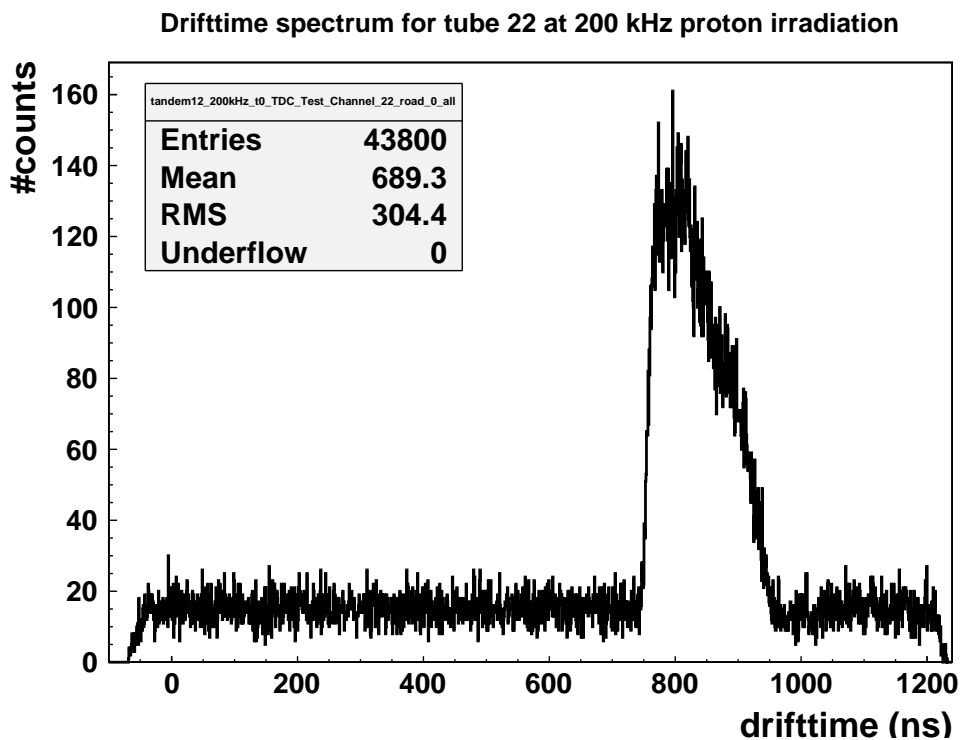
Figure 2.38: Drifttime spectrum for tube 22 at 200 kHz proton irradiation rate. The spectrum for the cosmic muon drifttimes sits on top of a uniform background of randomly coincident proton hits.

It must be noted, that the ADC units in which the ASD chips measure the charge on the mezzanine cards is not linear, especially for high values. See the transfer function for the non-linear amplifier stage in figure 2.39.

DA3 Transfer Curve
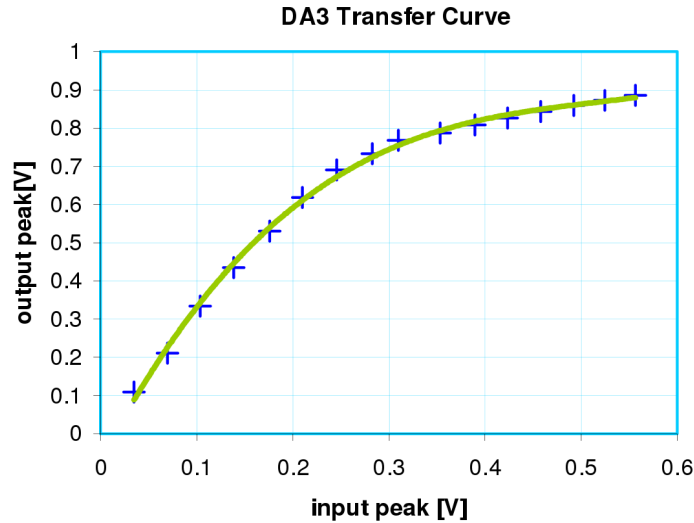
Figure 2.39: Transfer functions for the ASD chip compressing, non-linear differential amplifier stage prior to analog-to-digital conversion. [17]

No cuts to select cosmic muons are applied, so in the case of proton irradiation, in addition to the energy loss distribution for the cosmic muons, a high value peak for the contribution of the proton energy loss is visible around channel 180.

Figure 2.40 also shows, that the position of the cosmic muon peak and the proton peak shifts towards lower values in case of increasing proton irradiation. For the highest irradiation, the space charge effect of the protons leads to a large shift of the proton peak almost out of the ADC dynamic range.

To investigate the space charge effect on the signal height of cosmic muons, in figure 2.41 cuts are applied to select hits belonging to a reconstructed track. With increasing proton irradiation rate, the cosmic muon peak shifts towards the left and, beginning at 60 kHz irradiation rate, out of the dynamic range of the ADC.

The sMDT chamber layout allows to power the tubes of the irradiated layer independently, and in this way to monitor the current drawn of each of these tubes. The electrical current that is drawn from the tubes high voltage supply is the product of particle hit rate and the gas gain, weighted with the number of primary charges, each particle generates.

$$I_{\text{HV}} = \text{Gain} \times \frac{\text{Rate} \times \Delta E}{E_{\text{ionization}}} \tag{2.5}$$

Assuming a constant gas gain, the electrical current should follow the proton irradiation rate linearly. Measured currents for different irradiation rates are shown in figure 2.42. It is clearly visible, that the drawn current approaches a saturation value. This is the result of the reduction of gas gain.

Assuming an average energy of 30 eV to create an Argon ion-electron pair allows to calculate the effective gas gain as shown in figure 2.43. Effects that capture primary electrons during their drift are neglected in this calculation. Without irradiation the gas gain is close to the nominal value of 2×10^4. It shows a gain reduction of an order of magnitude for few MHz proton hit rate.

Nevertheless the effect on the muons passing the tube is believed to be less pronounced, as the sweeping motion of the proton beam lets the protons enter the tube volume very close to each other, maximizing the space charge effect onto each other.
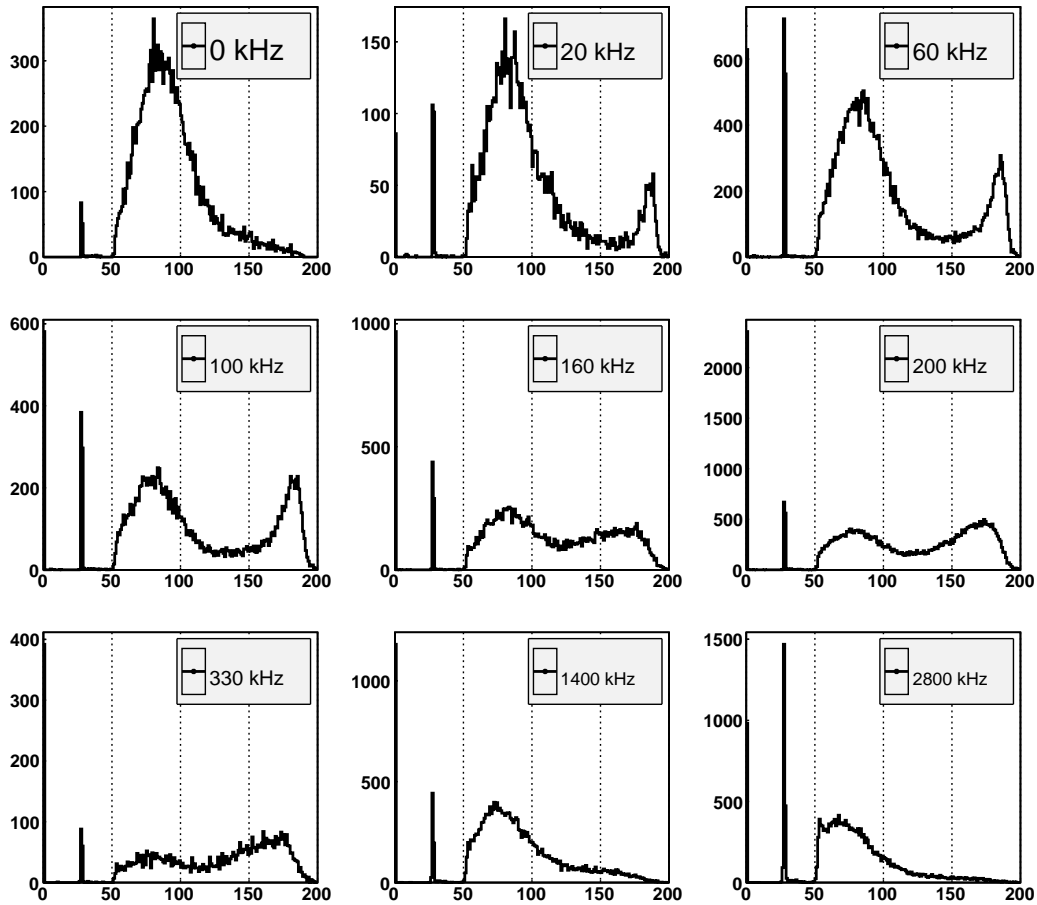
Figure 2.40: ADC spectra for all hits within the irradiated tube 22, for the different irradiation settings. With increasing rate up to 100 kHz, the peak of coincident protons grows around ADC value 180. A further increase of proton hit rate reduces the gas gain in the tube, shifting both muon and proton signals towards lower values and out of the dynamic range of the ADC at 50 counts. For the highest irradiation rates of 1400 kHz and more, the muon peak has shifted completely out of the ADC range, and even the proton signal is truncated on its lower end.
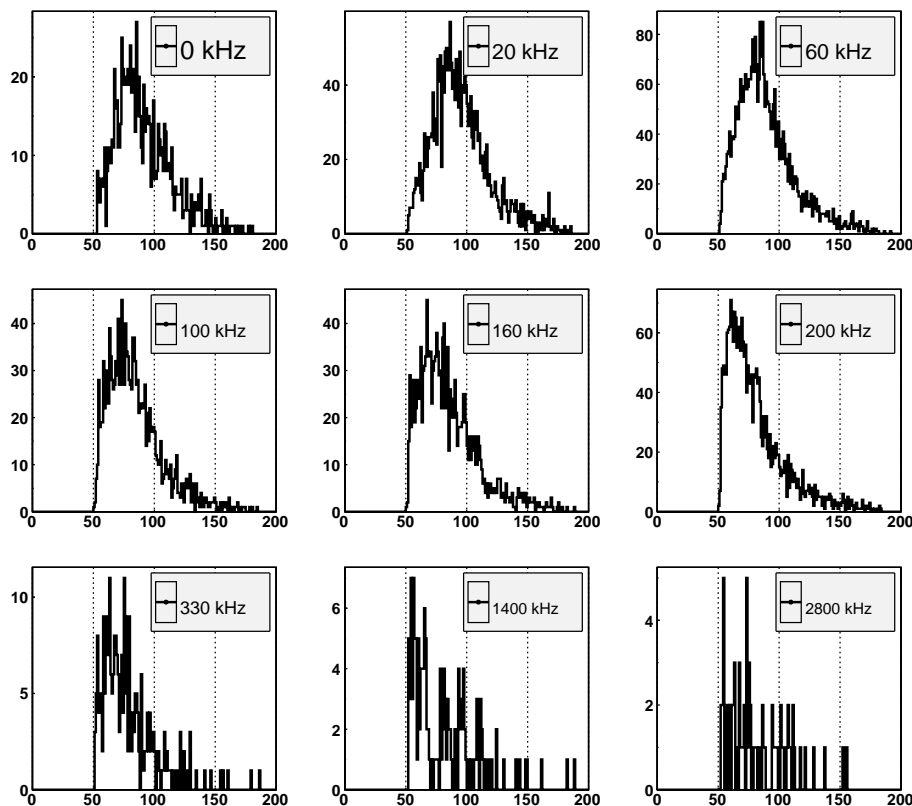
Figure 2.41: ADC count spectra for hits, that could be matched to a cosmic muon track in tube 22. With increasing irradiation rates, the spectrum shifts to lower values due to gain reduction by space charge effects. For the highest irradiation values, the muon signal shifts almost completely out of the ADC dynamic range.
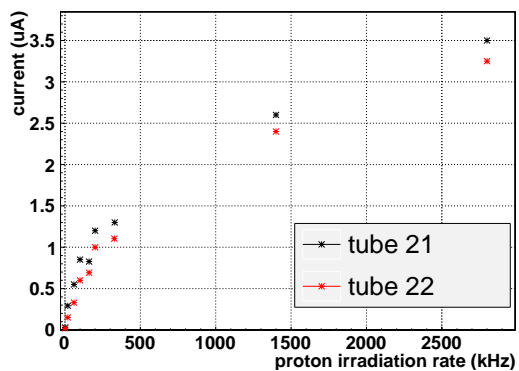
Figure 2.42: Current drawn by the first (tube 22) and second (tube 21) tube hit by protons for different irradiation rates. The non-linear behavior for high rates indicates a drop of the gas gain.
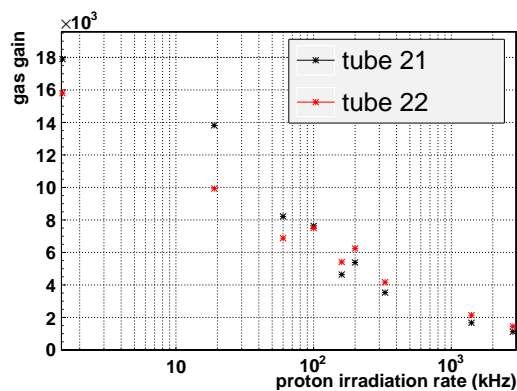
Figure 2.43: sMDT gas gain for protons at different irradiation rates, calculated from the current drawn by each tube

2.5.5 Spatial resolution

The unirradiated reference layers of the sMDT chamber were used to monitor the cosmic muon tracks. Comparing this track prediction with radius measurements in the irradiated layer determines the tubes spatial resolution as a function of irradiation rate.
The methods used to obtain the spatial resolution, also using time slewing compensation, are described in detail in appendix A.1.3.

Figure 2.44 shows the obtained radius-dependent spatial resolution of the sMDT tubes in the irradiated section, for up to 200 kHz proton irradiation rate. Limited availability of statistics did not allow to determine the resolution for the two highest investigated rates of 1400 kHz and 2800 kHz.
The obtained resolutions are within the expectations of measurements with 30 mm tubes, as mentioned in chapter 2.2, but omitting the heavily affected tube radii above 8 mm. The impact of the proton irradiation on the single tube spatial resolution is pronounced for radii lower than 1 mm, where gain drop effects increase the probability of missing small signals below the discriminator threshold. Above 6 mm, the slightly non linear rt-relation for 15 mm sMDT tubes at large radii also affects the electron drift velocity via space charge effects. Nevertheless the impact is limited, and the resolution in the outer tube regions is better than 200 μm for 200 kHz proton irradiation, corresponding to 19 kHz/cm^2.

The mean single tube spatial resolution over all tube radii is shown in figure 2.45, as a function of irradiation rate. Up to 200 kHz the resolution is affected only moderately to a value of (164.6 $\pm$ 3.1)μm.
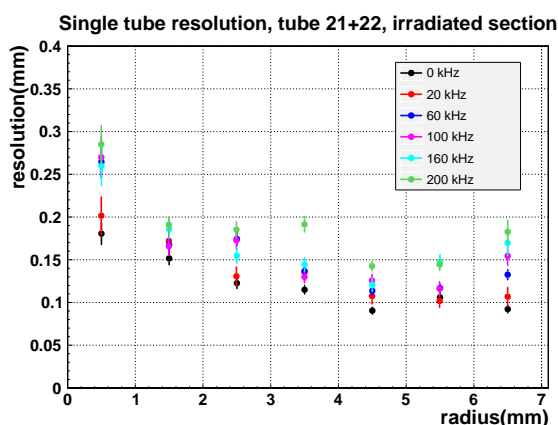
Figure 2.44: Radius-dependent single tube resolution with time slewing correction for tubes 21 and 22 at different proton irradiation levels. Limited statistics for the runs above 200 kHz proton rate do not allow to measure the resolution precise enough.
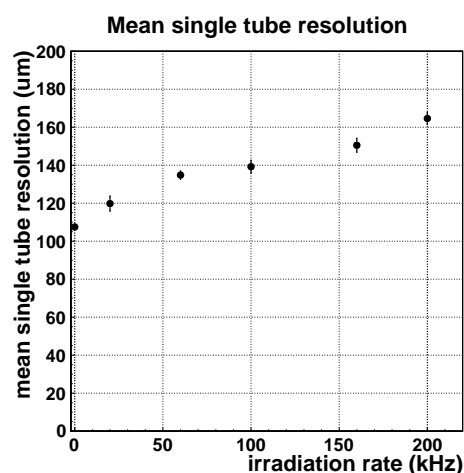
Figure 2.45: Tube 21 and 22 spatial resolution as a function of proton irradiation rate. The value is obtained from the radius-dependent distribution by means of a constant fit.

### 2.5.6 Detection efficiency

To judge the tracking capabilities of the detector system, an efficiency criterion is defined counting the amount of tracks crossing a tube, where the residual Δr is smaller than three times the spatial resolution of the tube, taking into account the variation of the resolution with drift radius[5]. This

---

[5]As the spatial resolution of the sMDT chamber changes slightly with irradiation rate, the definition fixes the spatial resolution to be used to calculate the 3-σ-efficiency to the one obtained in the case of no irradiation. It is necessary to

number, divided by the total amount of tracks crossing the tube, is called "3-σ-efficiency."

$$\varepsilon_{3\sigma} = \frac{N_{\text{tracks}}\big|_{(|\Delta r| < 3\sigma(r))}}{N_{\text{tracks}}} \tag{2.6}$$

Figure 2.46 illustrates this method. It is clear, that this number would ideally be one, but several mechanisms prevent this, including δ-electrons, space charge and electronics effects. These will be discussed later within this chapter.
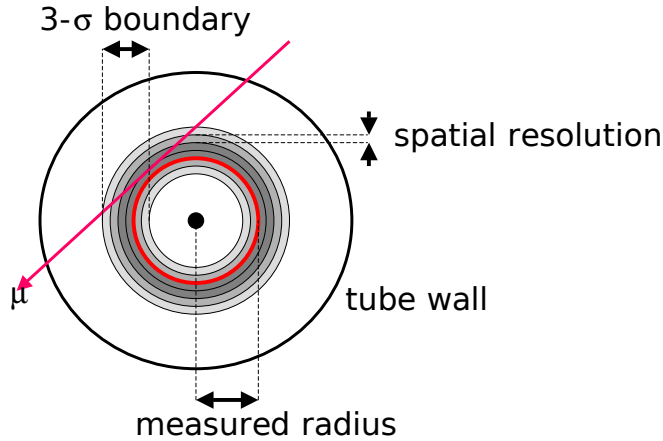
Figure 2.46: Schematic drawing of the allowed region for a muon measurement, defined by the reference track, to account for the 3-σ-efficiency.

An example for the 3-σ efficiency as a function of tube radius, together with the horizontal fit function to determine the average value is shown in figure 2.47, for tube 21 at 60 kHz proton irradiation rate. The distribution shows a variation over radius, with a significant decrease close to the tube wall, where the size of the 3-σ window is limited by the wall itself. In addition, the number of primary electrons is minimal for tracks close to the wall, due to the short muon path within the active volume of the tube. The mean value without proton irradiation for all 46 tubes lies between 92 and 94%, slightly below another measurement [23] on sMDT detectors of $(96.3 \pm 0.1)\%$, where high energy muons (up to 160 GeV) from the CERN SPS beam line have been used. Due to the relativistic rise in the Bethe-Bloch curve, these show a higher ionization and are less affected by scattering processes than cosmic muons.

As the number of tracks used to determine the efficiency is usually large, the errors in this counting experiment are determined by the binomial distribution error [25]

$$\Delta\varepsilon = \sqrt{\frac{\varepsilon \cdot (1 - \varepsilon)}{N}} \tag{2.7}$$

Figures 2.48 and 2.49 show the measured efficiency of selected tubes of the unirradiated and irradiated tube sections respectively. Dominantly, only the efficiency of the tubes of the irradiated layer is affected. Both, unirradiated and irradiated sections show a steady decrease of efficiency with increasing irradiation rate, whereas the effect on the irradiated tube section is more pronounced.

The limiting factor in absence of irradiation is dominantly the occurrence of δ-electrons. In this case, an electron hit by a muon is accelerated enough, to ionize itself gas molecules along its track. When this track passes the tube closer to the anode wire than the muon, the muon signal is masked by the

---

decide for a resolution reference, since for example using a worsening resolution with increasing irradiation rates would also broaden the 3-σ window, and therefore increase the efficiency.
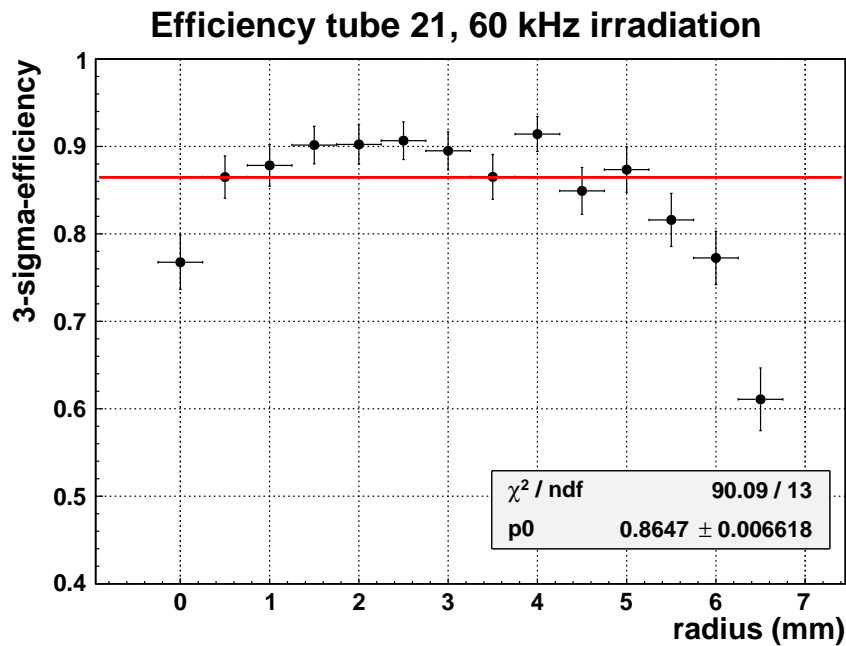
Figure 2.47: Radius-dependent 3-sigma-efficiency for tube 21 at 60 kHz proton irradiation rate, together with the average value, determined by means of a constant fit.
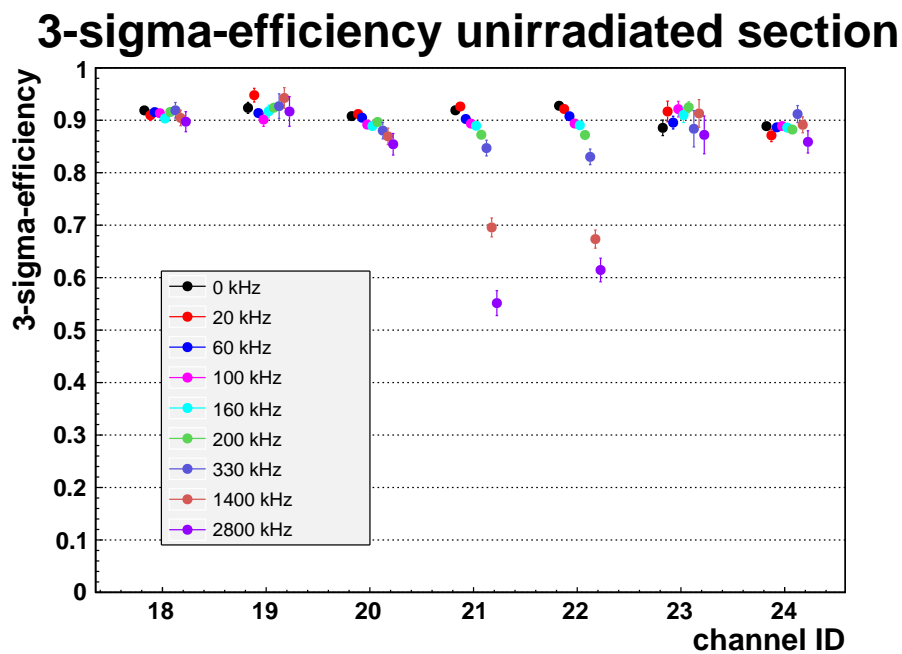
Figure 2.48: 3-sigma-efficiency for the unirradiated section of tubes 18 to 24 at different proton irradiation levels. The drop in efficiency is due to electronics deadtime effects and signal shape variations at increasing irradiation rate.
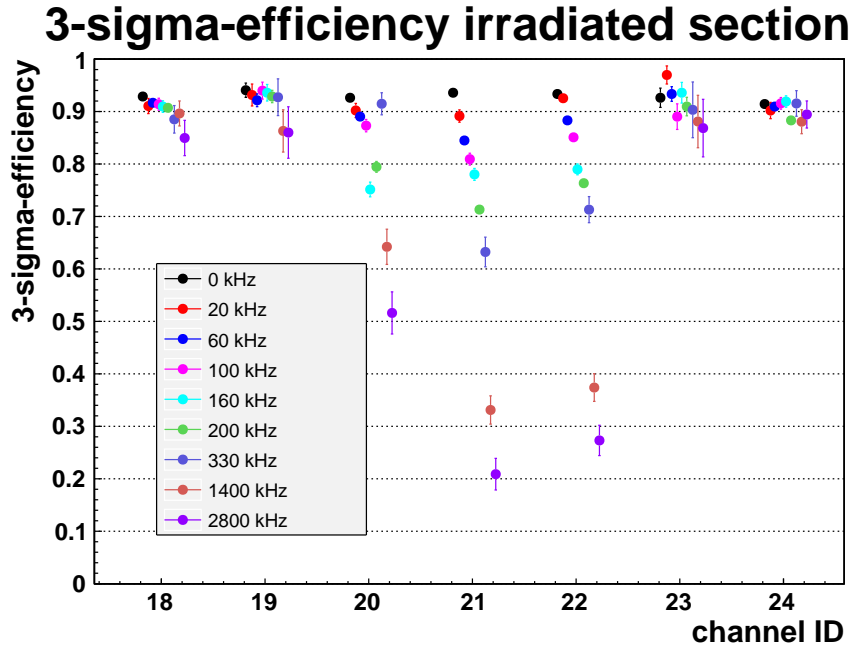
Figure 2.49: 3-sigma-efficiency of cosmic muons traversing the irradiated section of tubes 18 through 24 at different proton irradiation levels. Apart from electronics effects in figure 2.48, the space charge produced by the protons decreases the efficiency further.

preceding δ-electron signal. This reduced drifttime can then not be matched to the muon track, and the 3-σ-criterion fails. This effect is responsible for the baseline efficiency at zero irradiation.

At the presence of background irradiation, even in unirradiated sections of the tubes, the readout electronics has an influence on the tube efficiency. Each hit that is registered by the electronics is followed by a programmable deadtime with a minimum value of 201 ns. A muon hit is lost, if it falls into this deadtime window, caused by a preceding background hit.

In the irradiated tube sections, the space charge effects can either modify the electron drift velocity or the amplification field in a way, that the muon hit is completely missed, or its driftradius is incorrectly calculated, which leads to a failure of the 3-σ-criterion.

Now the different efficiencies can be disentangled as follows.
In absence of irradiation, the dominant source of inefficiency is the effect of δ-electrons. It can be extracted from the measurements without proton irradiation:

$$\varepsilon_{0\,\text{kHz}} = \varepsilon_\delta \qquad (2.8)$$

Focusing on the unirradiated sections of the tubes during proton irradiation, the efficiency is additionally affected by electronics deadtime effects, so the resulting efficiency can be considered as the product of δ-electron-efficiency and electronics-efficiency:

$$\varepsilon_{\text{unirr}} = \varepsilon_\delta \times \varepsilon_{\text{electronics}} \qquad (2.9)$$

In addition to the above effects, the irradiated section of the tubes is affected by space charge effects, so here the resulting efficiency is considered as the product of all three components:

$$\varepsilon_{\text{irr}} = \varepsilon_\delta \times \varepsilon_{\text{electronics}} \times \varepsilon_{\text{space charge}} \qquad (2.10)$$

$\varepsilon_{0\,\text{kHz}}$, $\varepsilon_{\text{unirr}}$ and ε_{irr} can be extracted from the measurements, and thus it is possible to distinguish the different influences from electronics effects $\varepsilon_{\text{electronics}}$ and space charge influence $\varepsilon_{\text{space charge}}$, considering a constant ε_δ of 92%.

Equation 2.3 in chapter 2.2 describes the measured rate R_m as a function of the real hit rate R, due to the presence of a deadtime τ:

$$R_m = \frac{1}{\frac{1}{R} + \tau}$$

The average probability P for the detector electronics being busy at any point in time is derived by the multiplication of the measurement rate R_m with the deadtime τ

$$P = R_m \tau = \frac{\tau}{\frac{1}{R} + \tau} \tag{2.11}$$

The electronics efficiency is the probability for the detector to not be busy and therefore:

$$\varepsilon_{\text{electronics}} = 1 - P = 1 - \frac{\tau}{\frac{1}{R} + \tau} \tag{2.12}$$

which calculates as

$$\varepsilon_{\text{electronics}} = \frac{R_m}{R} = \frac{1}{1 + R\tau} \tag{2.13}$$

in agreement with equation 2.3 in chapter 2.2.
Figure 2.50 shows the efficiency measurement for the unirradiated tube section, including δ-electron effects and electronics effects as described in equation 2.9. Therefore $\varepsilon = \frac{\varepsilon_\delta}{1+R\tau}$ has been chosen as fit function, with $\varepsilon_\delta = 0.92$ and τ as free parameter.
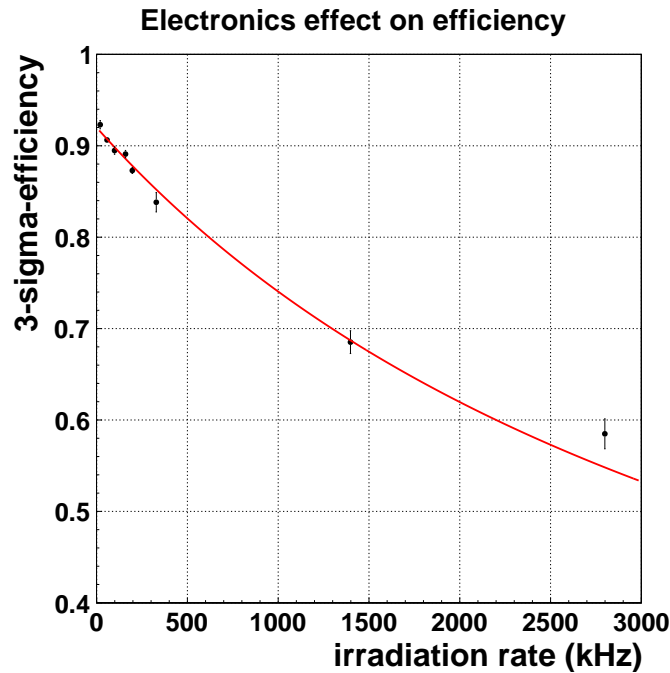
Figure 2.50: 3-σ-Efficiency measured for the unirradiated sections of tubes 21 and 22. Overlayed is the fit function from equation 2.13, with an effective deadtime of 242 ns and also including a δ-electron efficiency of 0.92.

The fit to the measured efficiency returns a deadtime of $\tau = 242$ ns, which is larger than the configured deadtime of 201 ns.

The bipolar pulse shaping electronics of each channel introduces a signal of opposite (positive) polarity following each hit (see chapter 2.7). If a (negative) muon signal occurs during this time window, the resulting signal fed to the discriminator is an overlay of both, the signal and the preceding "overshoot" pulse. This reduced pulse height may not pass the discriminator threshold, and thus the hit is missed. This results in an additional signal height dependent deadtime, which adds up to the configured value for a larger effective deadtime.

The influence due to the space charge effects is disentangled from the efficiency measurement in the irradiated tube sections as described in equation 2.10. The result is shown in figure 2.51. Taking into account the exponential gain drop behavior from figure 2.43, an exponential fit function has been chosen to consider the saturating space charge effect due to the increasing gain drop with increasing irradiation rate. The fit returns

$$\varepsilon_{\text{space charge}} = 0.405 + 0.524 \times e^{-0.0170 \times R} \tag{2.14}$$

With R in units of $\frac{\text{kHz}}{\text{cm}^2}$, and including again the δ-electron efficiency of 0.92.
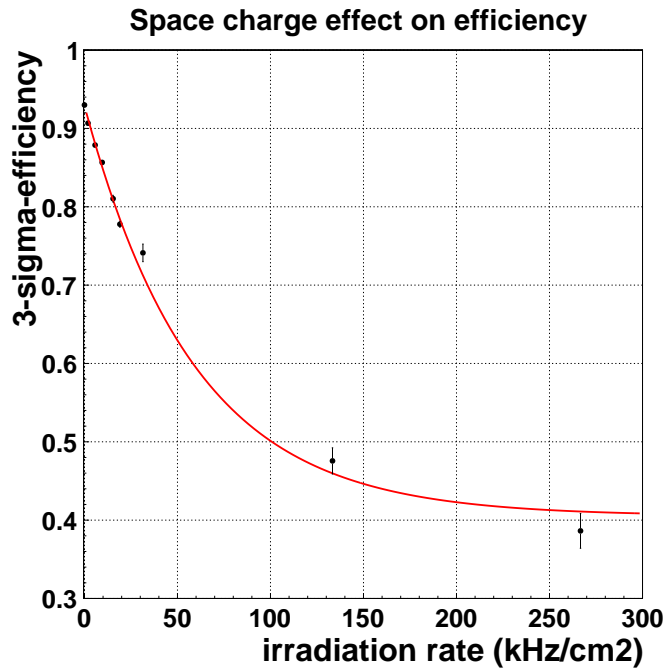
Figure 2.51: Disentangled exponential saturating drop of the 3-σ-efficiency due to space charge effects, including the rate-independent probability for δ-electrons. Note that for the space charge effect, rate-per-area is the relevant value, and the x-axis label is based on an irradiated tube area of 10.5 cm^2. The fit function is listed in equation 2.14

.

2.5.7   Comparison with measurements at the CERN Gamma Irradiation Facility

A prototype chamber of sMDT tubes has been tested [31] within the before mentioned Gamma Irradiation Facility (GIF) at CERN. Here, tubes of 0.95 m length have been irradiated almost homogeneously with 662 keV γ-particles at high rates.

Using the separation methods on the measurements with local proton irradiation introduced in chapter 2.5.6, it is possible to compare both measurements by extrapolating the tandem measurements onto homogeneously irradiated tubes. The effective efficiency is a weighted product of electronics effects depending on the **rate per tube**, and space charge effects, depending on the **rate per area**. It calculates as

$$\varepsilon = \varepsilon_\delta \times \varepsilon_{\text{electronics}}(R_{\text{absolute}}) \times \varepsilon_{\text{space charge}}(R_{\text{per area}}) \tag{2.15}$$

Figure 2.52 shows the overlay of the GIF efficiency measurements with the tandem measurements, extrapolated to a homogeneous irradiation of the 0.95 m tubes. The curve resulting from the combination of electronics and space charge effect matches very well the GIF measurement points for higher irradiation rates. Each line includes the efficiency on δ-electrons separately.

It must also be noted that there are potential differences in between the two measurements. The amount of ionization caused by photons and protons is different. The proton simulation studies from chapter 2.5.2 reveal an energy deposition of 150 keV or more within the gas, whereas GIF measurements [32] suggest a much lower primary mean ionization of around 25 keV per photon.

In addition the protons hit the tubes relatively close by due to the sweeping nature of the (defocused) proton beam, whereas the photons hit the tube at random positions.

Nevertheless the combination of the results validates the accomplished separation of electronics and space charge effects, and allows precise extrapolation for various (absolute and per-rate) irradiation scenarios.

Figure 2.52: Comparison of proton irradiation efficiencies with measurements [32] at the CERN Gamma Irradiation Facility (GIF). The proton measurements separation of electronics (dashed line) and space charge effects (dash-dotted line) allows weighting and extrapolation (solid line) to the GIF measurements, where tubes of 95 cm length were irradiated homogeneously for a total area of 142.5 cm^2 per tube.

2.6 sMDT chamber irradiation with high energy neutrons

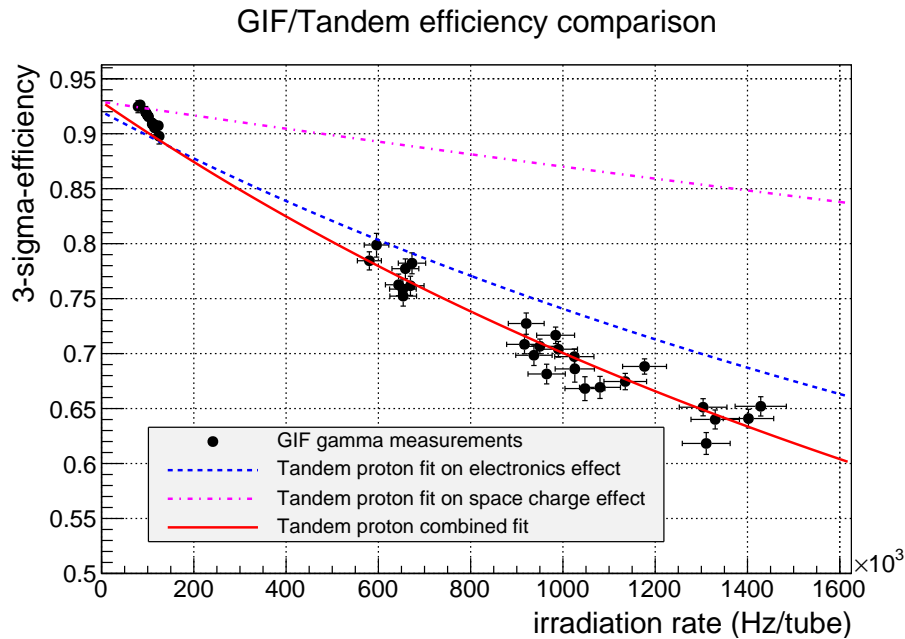The main background hit rate in the region of the ATLAS small wheel detectors is composed of photons and neutrons [9]. The MLL tandem accelerator facility that was used to generate protons as described in the previous chapter, can also be configured to generate high energy neutrons. The tests described in this chapter were all performed during the beam time in November 2011.

Neutrons are generated by deuteron breakup in the nuclear potential of beryllium. As the deuteron has to penetrate the coulomb wall, low Z materials are advantageous. By use of 20 MeV deuteron ions, neutrons are generated with a Gaussian like energy distribution peaking at 11 MeV and with a FWHM of 10 MeV. The beryllium target was located on the inner wall of the beam pipe end flange, made of aluminum. According to [33], with 1 μA of deuteron ion beam up to 10^7 n/cm^2 are produced within an angular region of $\pm 30°$.

Neutron rates were measured with liquid scintillator detectors using pulse shape analysis, as well as with BF$_3$ counters. The different irradiation rates during the measurements were achieved by regulation of the deuteron beam current.

The beryllium target was mounted on an electrically isolated flange, so the deuteron ion beam current was simply measured as the electrical current flowing from the flange to the accelerator ground.

Neutrons are not the only contribution to the irradiation field. In addition to the primary neutron flux, a large number of photons is emitted not only by the beryllium target, but also by neutron irradiated material. This is the result of nuclear reactions where neutrons activate for example aluminum atoms, like the ^{27}Al(n, γ) reaction.

Both neutrons and photons contribute to the hit rate in the detector under test, and a complete disentanglement turns out difficult. Therefore in the following chapter all irradiation sets that were analyzed show the result of a mixed irradiation field. In addition, the detector tubes are known to have different detection efficiencies on neutrons and photons. The efficiency of 30 mm MDT tubes on MeV neutrons has been determined in [34] as $(3.99 \pm 0.21) \times 10^{-4}$, compared to a photon efficiency of 0.92×10^{-2} for 662 keV γ-particles [21]. The value for the photon efficiency has been measured for a single photon energy, so additional systematic uncertainties must be assumed due to the γ energy spectrum during irradiation.

In addition to the already introduced values of spatial resolution and track reconstruction efficiency, this chapter will also cover the occurrence of electronic crosstalk between channels of single ASD chips, and the neutron induced failure of data acquisition hardware.

2.6.1 Experimental setup

Due to the high particle flux within the experimental area, it was not possible to trigger on cosmic muons with just two scintillation counters. In fact, a stack of five scintillators was necessary, to reduce the random coincidence to an acceptable level. Most of the runs were then taken at a muon trigger rate of 2 to 4 Hz. Without irradiation and after a cool down period of nine days, the trigger rate of the setup settled around 1.3 Hz. The accidental coincident triggers not correlated to a cosmic muon are later sorted out, as it is not possible to fit a straight track onto them.

sMDT readout was performed the same way as during proton irradiation, except for the trigger configuration, that now includes more layers and no segmentation along the tube axis.

The total amount of current drawn by 46 tubes of the detector was monitored over the whole period with a time resolution better than 10 seconds, using the RS232 serial output of the iseg SHQ 224M power supply.

During a similar experiment, the neutron flux created by the deuteron-breakup reaction has been measured, as a function of distance [33], showing a $\frac{1}{r^2}$ distribution, see figure 2.54.
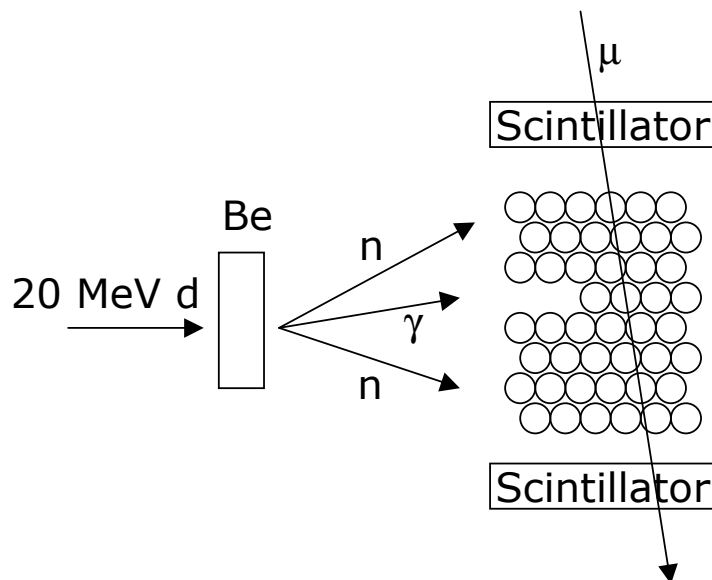
Figure 2.53: Neutrons are generated by the nuclear breakup of deuterons on a beryllium target.
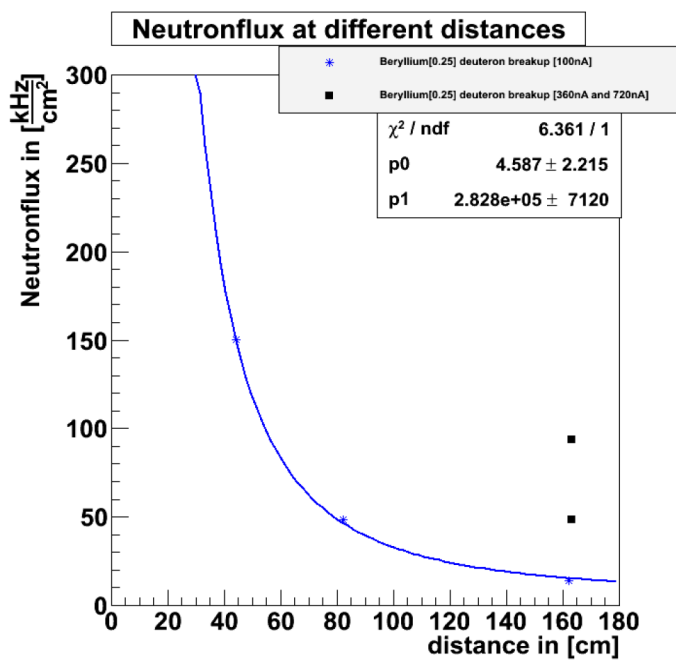
Figure 2.54: Neutron flux as a function of distance from the beryllium target. The neutron rate follows a $\frac{1}{r^2}$ law with increasing distance from the target [33]. The black measurement points above the curve result from measurements at higher irradiation rates.

The angular distribution of the neutrons has been measured using a BF_3 counter with known efficiency, that is insensitive to γ-radiation. The results can be obtained from figure 2.55. Without additional shielding, the neutron rate has a maximum in forward direction, with tails to large angles, dropping to 50 % around 25 degrees. Lead shielding reduces the absolute neutron rate and additionally flattens the angular distribution, due to scattering of the neutrons in the absorber material.
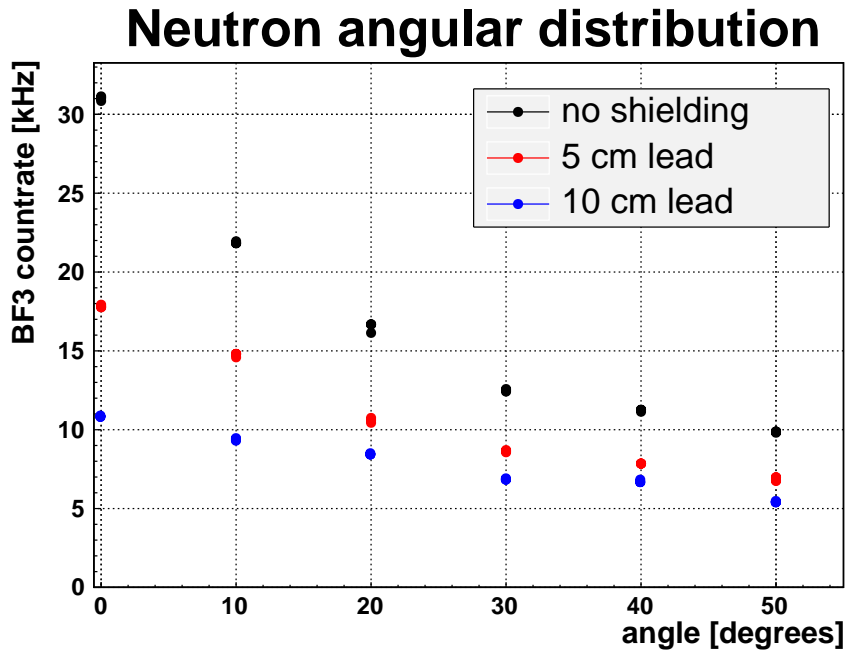
Figure 2.55: Angular distribution of neutrons for different lead shielding thicknesses. The values were measured with a BF3-counter.

The distance in between beryllium target and the sMDT detector was approximately 0.75 m.

It must be noted, that during the measurement, another detector system under test was located in between the accelerator system and the sMDT chamber, causing additional scattering of neutrons, absorption and (n, γ) reactions.

2.6.2   Hit rate and chamber current for several different radiation compositions

As already mentioned, during the neutron irradiation measurements the irradiated areas were not as well defined as during proton irradiation. More likely, a homogeneous irradiation of the complete sMDT chamber can be assumed. In addition, it was not possible to place a scintillation counter in front of the detector to determine the hit rate, due to the mixed composition of neutrons and photons, and the different detection efficiency of scintillator material and detector.

A different approach has been chosen to determine the hit rate within the detector, using the detector itself, which then includes all efficiencies. So the real particle flux was accordingly higher than detected.

The MDT and thus the sMDT prototype chamber electronics allows the insertion of random triggers at typically 5 kHz. Each of these triggers opens a time window of defined length, during which hits within each tube are recognized. The width of the time window is determined to be 1.275 μs by the total width of the full TDC time spectrum using random noise triggers. Counting these events with at least one hit and dividing this number through the total active window length returns a hit rate.
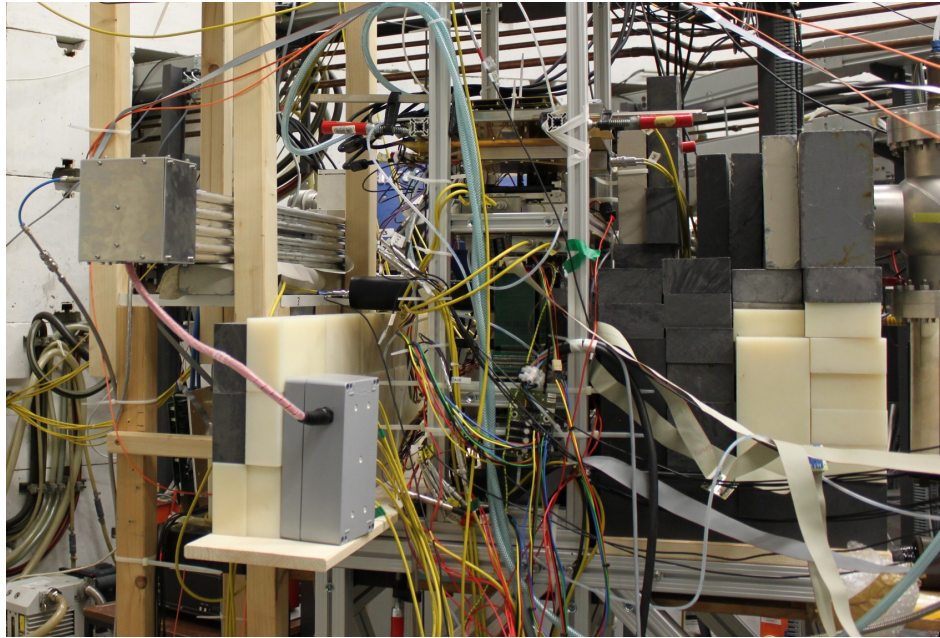
Figure 2.56: Experimental setup for the neutron irradiation of the sMDT prototype chamber, side view. On the right, the accelerator beam pipe is visible, with the end flange hidden behind shielding bricks. On the left, the sMDT chamber can be seen, together with its high voltage distribution box.
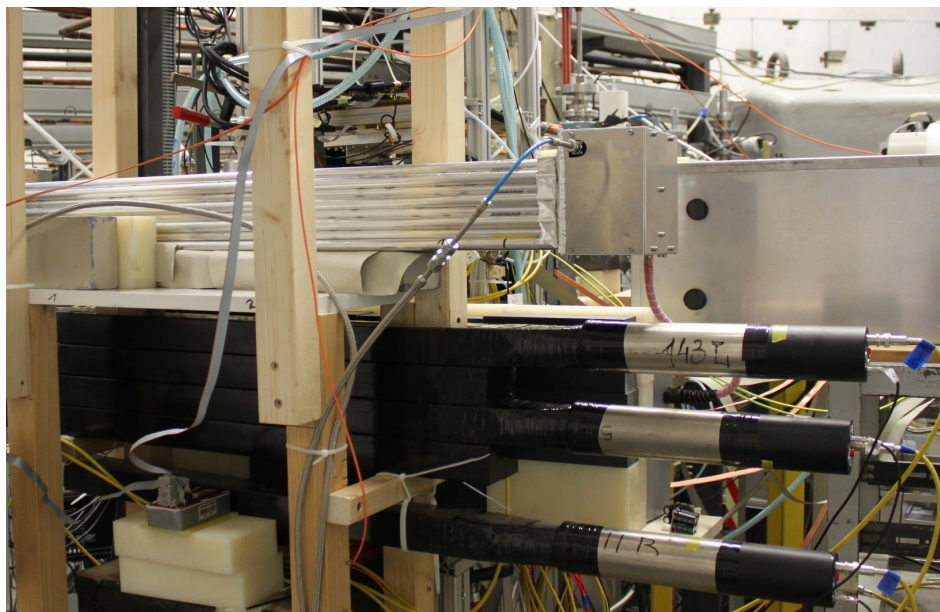
Figure 2.57: Experimental setup from the back. The sMDT chamber is visible, together with the stack of five trigger scintillators below.

A correction is applied to the hit rate R for hits that occur within the electronics dead time of 201 ns after each hit, using the same formula as in chapter 2.2

$$R = \frac{R_m}{1 - R_m \times 201 \text{ ns}}$$
(2.16)

For the following measurement of detector hit rates, the lowest of the three mezzanine cards in the setup was chosen, as all of its channels were connected to tubes.

An additional way of measuring the irradiation density is the amount of current drawn, that is proportional to the particle hit rate and has already been defined in equation 2.5.

To investigate the contribution of photons and neutrons to the total rate, two different absorber materials were placed in between the beryllium target and the detector. These are

1. A single layer of lead bricks with a thickness of 5 cm. Due to its dense and heavy nuclei it mostly absorbs photons, whereas neutrons are less affected, see figure 2.55.

2. Either two or four layers of bricks made of borated plastic with a thickness of 5 cm each. Due to their low density and light nuclei, mostly hydrocarbons, the photon absorption is very low. In contrast the high content of hydrogen atoms allows a maximum kinematic transfer of momentum from the neutrons. The additional presence of boron atoms with a high capture cross section for thermal neutrons makes this material a reasonable neutron absorber.

Figure 2.58 shows the measured hitrates per tube, averaged over the mentioned mezzanine card as a function of deuteron beam current, making use of different shielding arrangements. The current drawn by the chamber in each of these configurations is summarized in figure 2.59
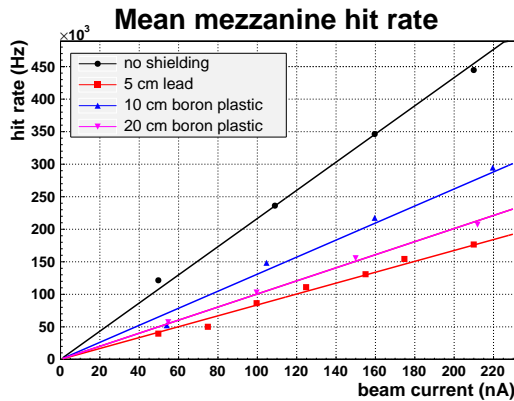
Figure 2.58: Single tube hit rate measured with the sMDT chamber as a function of deuteron beam current. Different shielding arrangements were used to enrich the particle flux with either photons or neutrons.
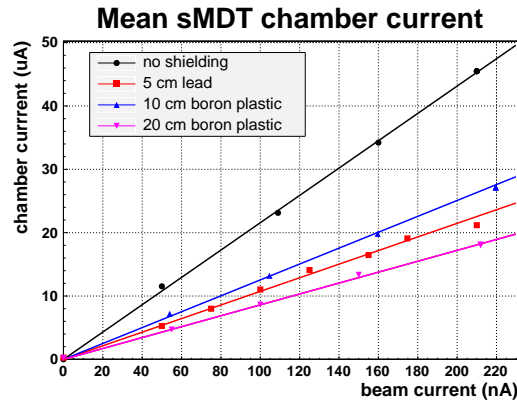
Figure 2.59: Current drawn by the sMDT chamber as a function of deuteron beam current for the different shielding arrangements.

In addition, two BF_3 counter detectors were used to measure the neutron flux at the experimental location. One BF_3 counter [6] was placed in forward direction at zero degrees at a distance of 2.40 m from the beryllium target. The second one was placed upstream from the target next to the beam pipe under a small angle, counting only backscattered neutrons. These devices contain BF_3 as detection gas in a proportional tube counter. Due to the large capture cross section for thermal neutrons and the massive surrounding with paraffin as moderator, these devices are also sensitive to fast neutrons with calibrated efficiency. The $n_{\text{thermal}} +^{10} B \rightarrow^7 Li + \alpha$ with an energy yield of around 1 MeV allows to operate the proportional counter in a γ insensitive mode. The effective sensitive area is 0.34 cm^2 [34], allowing to estimate the neutron flux from the BF_3 count rate.

---

[6]Studsvik model 2202 D

The measured rates can be obtained from figure 2.60. Using 20 cm of boron plastic, the neutron intensity can be reduced by a factor of 5.9.

Count rates from the upstream BF_3 detector indicate that neutrons are scattered back from absorber material, flange, detector under test and the cavern walls. Lead as absorber increases the number of backscattered neutrons, whereas boron plastic bricks capture neutrons and therefore only neutrons that are scattered within the flange remain as main contribution, independent from the plastic absorber thickness.
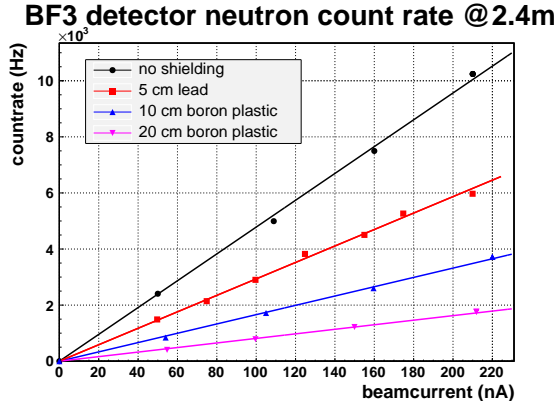
Figure 2.60: Count rate of a neutron-only sensitive BF3 detector in the accelerator axis at 2.4 m distance from the beryllium target.
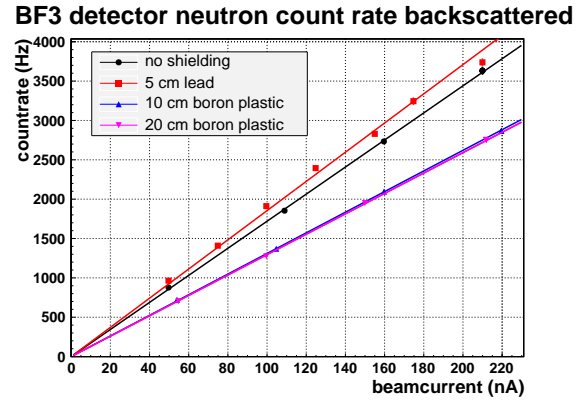
Figure 2.61: BF3 detector count rate in the accelerator upstream direction, detecting backscattered neutrons only.

The measured hit rates Rm_{all} show a linear behavior up to very high rates of several hundred kHz per tube. This expected behavior justifies the hit rate measurement method. The highest rate is measured in absence of any absorbing material.

The following table lists the linear increase of the measured hit rate, chamber current and hit rate of the forward BF_3 counter with deuteron beam current.

Absorber material	Rm_{all} (Hz/nA)	current (μA/nA)	BF_3 neutron count rate (Hz/nA)
no absorber	2171.2 ± 1.1	0.2095 ± 0.0007	47.82 ± 0.18
5 cm lead	837.1 ± 0.5	0.1036 ± 0.0005	29.34 ± 0.13
10 cm boron plastic	1309.6 ± 0.8	0.1198 ± 0.0005	16.60 ± 0.07
20 cm boron plastic	1011.5 ± 0.7	0.0857 ± 0.0002	8.12 ± 0.13

Table 2.4: Fitted linear increase of the measured sMDT hit rate per tube Rm_{all}, chamber current with deuteron beam current and BF3 detector neutron count rate for different absorber configurations.

2.6.3 Irradiation flux composition and detection efficiencies

Previous measurements [33] indicate, that at 1 μA deuteron beam current, the neutron flux density at 30 cm distance from the target is $10^7 \frac{n}{cm^2 s}$. A quadratic declining extrapolation to 0.75 m distance at 100 nA beam current returns $1.6 \times 10^5 \frac{n}{cm^2 s}$.

The BF_3 measurement for 100 nA beam current at 2.40 m distance from the target is $4.8 \times 10^3 \frac{1}{s}$. Together with an experimentally determined calibration factor of $\frac{5}{3}$ and the BF_3 active area of 0.34 cm^2, the neutron flux density at a distance of 0.75 m is obtained.

$$F_{BF_3}@0.75m = 2.41 \times 10^5 \frac{n}{cm^2 s}$$

Nevertheless a systematic uncertainty of ~50% on the BF_3 counter measurement must be assumed, due to the detector response to the broad neutron energy spectrum and aging effects of the device. This uncertainty dominates all up following measurements and calculations, based on the neutron rate measured with the BF_3 counter.

The deviation from the preceding measurement is then considered to be within the BF_3 calibration and neutron scattering conditions during the different experiments.

Weighting the neutron flux for a 95 cm sMDT tube at 0.75 m distance from the target with a factor of 0.7 due to linear approximating the measurements in figure 2.55 from 0 to 30 degrees, returns the expected average neutron flux density $\bar{F}_{neutron}$ at the sMDT location

$$\bar{F}_{neutron} = F_{BF_3}@0.75m \times 0.7$$

and with a tube length of 95 cm and 1.5 cm diameter

$$R_{neutron} = \bar{F}_{neutron} \times 142.5 \text{ cm}^2$$

the expected neutron hit rate $R_{neutron}$ for a single sMDT tube. Table 2.5 summarizes the neutron flux from the BF_3 measurement with different absorber configurations, interpolated to the sMDT detector position and the corresponding neutron hit rates.

Absorber material	$\bar{F}_{neutron}$ ($\frac{1}{cm^2s}$)	$R_{neutron}$ ($\frac{1}{s}$)
no absorber	1.7×10^5	2.4×10^7
5 cm lead	1.0×10^5	1.5×10^7
10 cm boron plastic	5.8×10^4	8.3×10^6
20 cm boron plastic	2.9×10^4	4.1×10^6

Table 2.5: Expected neutron flux density $\bar{F}_{neutron}$ and hit rate $R_{neutron}$ for the sMDT tubes at 100 nA beam current, interpolated from BF_3 counter measurements, including a geometric weighting factor of 0.7 and BF_3 calibration values. A systematic uncertainty of ~50% must be assumed due to the BF_3 counter calibration.

Figure 2.62 shows the normalized sMDT ADC spectra for tube number 22 and no additional shielding at different irradiation rates. Since no deviation in shape is observed for irradiation rates up to 200 nA deuteron beam current, it can be concluded that there is no relevant gain drop effect due to space charge.

The same ADC spectra but for different shielding configurations at a fixed deuteron beam current of 200 nA are shown in figure 2.63, again normalized for the main peak. For the different shielding material configurations, a clear variation is visible in the upper end of the spectrum for very high[7] signals. These represent the high-charge signals generated by neutron recoil nuclei, whereas the broader spectrum up to this threshold represent the hits due to gamma irradiation. Note, that the latter also includes photons from (n, γ) reactions.

Counting the integral content for the signals above ADC channel 187 allows for an approximation of the measured neutron to gamma ratio. The neutron hit rate detected by a sMDT tube $\tilde{R}_{m, neutron}$ is calculated by the ratio and the absolute hit rate $R_{m, all}$

$$\tilde{R}_{m, neutron} = \frac{N_{ADC, neutron}}{N_{ADC, all}} \times R_{m, all}$$

---

[7]Note the strong non-linear response of the ASD chip for the charge digitization from figure 2.39.
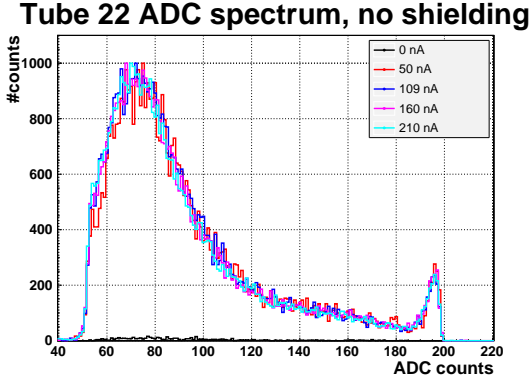
Figure 2.62: Measured ADC spectrum for tube 22 for different irradiation rates. The overlaid spectra represent different deuteron beam currents, and are scaled in y to match in height. No variation of the peak position is visible, even at maximum irradiation rate, giving no indication for gain drop effects due to space charge effects inside the tube.
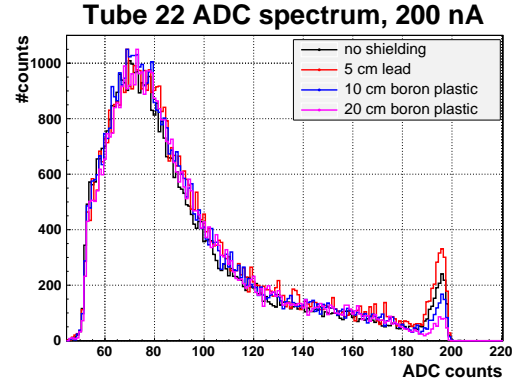
Figure 2.63: Measured ADC spectrum for tube 22 at different shielding configurations. The spectra are scaled in y to match in height. No variation in the main peak position is observed, but the portion of entries in the upper end of the ADC dynamic range changes with the shielding composition. 5 cm of lead increase the share of highly ionizing particles, whereas an increasing thickness of boron plastic shielding reduces the share.

The comparison with the BF_3 counter neutron flux measurement $R_{neutron}$ allows to calculate the sMDT tubes neutron detection efficiency.

$$\varepsilon_{neutron} = \frac{\tilde{R}_{m, neutron}}{R_{neutron}}$$

Table 2.6 summarizes the values of neutron content and neutron detection efficiency.

Absorber material	$N_{ADC, all}$	$N_{ADC, neutron}$	neutron share	$\varepsilon_{neutron}$
no absorber	48110	1654	3.44 %	3.1×10^{-4}
5 cm lead	20390	912	4.47 %	2.6×10^{-4}
10 cm boron plastic	31490	662	2.10 %	3.3×10^{-4}
20 cm boron plastic	24180	283	1.17 %	2.9×10^{-4}
average value				$(3.0 \pm 0.3) \times 10^{-4}$

Table 2.6: Share of neutron signals in the sMDT ADC spectrum range above 187 ADC counts for different absorber configurations and effective sMDT neutron detection efficiencies $\varepsilon_{neutron}$, using the sMDT hit rates from table 2.4 and the neutron flux $R_{neutron}$ from table 2.5. Note the additional uncertainty due to the BF_3 counter calibration.

Due to the low statistics within the ADC spectra, the average value over all shielding geometries for the neutron detection efficiency is calculated, and used for the further considerations. Its value is $\bar{\varepsilon}_{neutron} = (3.0 \pm 0.3) \times 10^{-4}$, which differs slightly from the value of $(3.99 \pm 0.21) \times 10^{-4}$ for 30 mm MDT tubes [34]. Part of this is explainable also by the smaller sMDT diameter, resulting in a reduced neutron path within the gas volume, which results in a reduced probability of argon nuclear recoil reactions.

The sMDT detection efficiency on γ-particles is expected to vary less on the tube diameter, as most of the reactions happen in the aluminum tube walls, which are of the same thickness as the 30 mm MDT tube walls.

With this average value for neutron detection efficiency, the neutron count rate $R_{m,\ neutron}$ can be again calculated from the total count rate $R_{m,\ all}$

$$R_{m,\ neutron} = \bar{\varepsilon}_{neutron} \times R_{neutron}$$

and the remaining detected hits are attributed to γ hits.

$$R_{m,\ \gamma} = R_{m,\ all} - R_{m,\ neutron}$$

Using a γ efficiency of 0.92×10^{-2} [21], the γ fluence can be calculated from the γ hit rate

$$\bar{F}_\gamma = \frac{R_{m,\ \gamma}}{142.5\ \text{cm}^2 \times \varepsilon_\gamma}$$

Table 2.7 summarizes the detected rates, separated for neutrons and gammas in the case of 100 nA deuteron beam current, as well as the extrapolated neutron and γ fluences. Still, a weighting factor of 0.7 is included to account for the particle angular distribution along the 95 cm tubes.

Absorber material	$R_{m,\ neutron}\ \left(\frac{1}{s}\right)$	$R_{m,\ \gamma}\ \left(\frac{1}{s}\right)$	$\bar{F}_{neutron}\ \left(\frac{1}{cm^2 s}\right)$	$\bar{F}_\gamma\ \left(\frac{1}{cm^2 s}\right)$
no absorber	7.1 kHz	210 kHz	1.7×10^5	1.6×10^5
5 cm lead	4.3 kHz	79.4 kHz	1.0×10^5	6.1×10^4
10 cm boron plastic	2.5 kHz	128 kHz	5.8×10^4	9.8×10^4
20 cm boron plastic	1.2 kHz	99.8 kHz	2.9×10^4	7.6×10^4

Table 2.7: Measured neutron and γ hit rates and fluences for different shielding configurations. Note the additional uncertainty due to the BF_3 counter calibration and inaccurate photon detection efficiency.

This picture fits well into the expectation of gamma or neutron flux enrichment by the addition of either plastic absorber material or lead. Nevertheless this enrichment is not possible infinitely well. For example 5 cm lead are expected to remove 92 % [35] of gamma particles in the energy range around 1 MeV. The measurement shows only a reduction by 62 %, so the γ flux is again enriched by particles emerging from (n, γ) reactions. On the other hand the plastic absorber material not only removes neutrons, but also γ particles.

The current drawn by the irradiated chamber also shows a linear behavior with increasing deuteron beam currents, but with slightly different weighting. The use of lead shielding, which enriches the neutron content in the particle flux, has a higher impact on the drawn current, as on the particles counted. This implies that on average, a neutron hit creates more primary charges within a sMDT tube than a photon hit, due to the highly ionizing recoil nuclei, in agreement with the ADC measurements.

As a result of material activation by neutron capture, after switch off of the accelerator the particle flux in the experimental area, and thus the hit rate in the sMDT chamber is not zero at once. The decay of activated nuclei can be visualized by the electrical current, drawn by the detector tubes. Depending on the neutron flux and duration, the current drops immediately to a value of roughly 10 %, and then exponentially to the quiescent value of few hundred nA with a half life of around 6 minutes, as pictured in figure 2.64. ^{28}Al as a potential activated material has only a half life of around 2.2 minutes, so additional isotopes must be produced, for example isotopes of the aluminum alloy elements like manganese, magnesium or silicon, resulting in the observed decay behavior.
As a result of this measurement, it is legitimate to assume that during a series of measurements, no influence from previous higher flux periods has to be accounted for, as several half times pass already

in between measurements, and measurement timescale is at least two orders of magnitude higher.
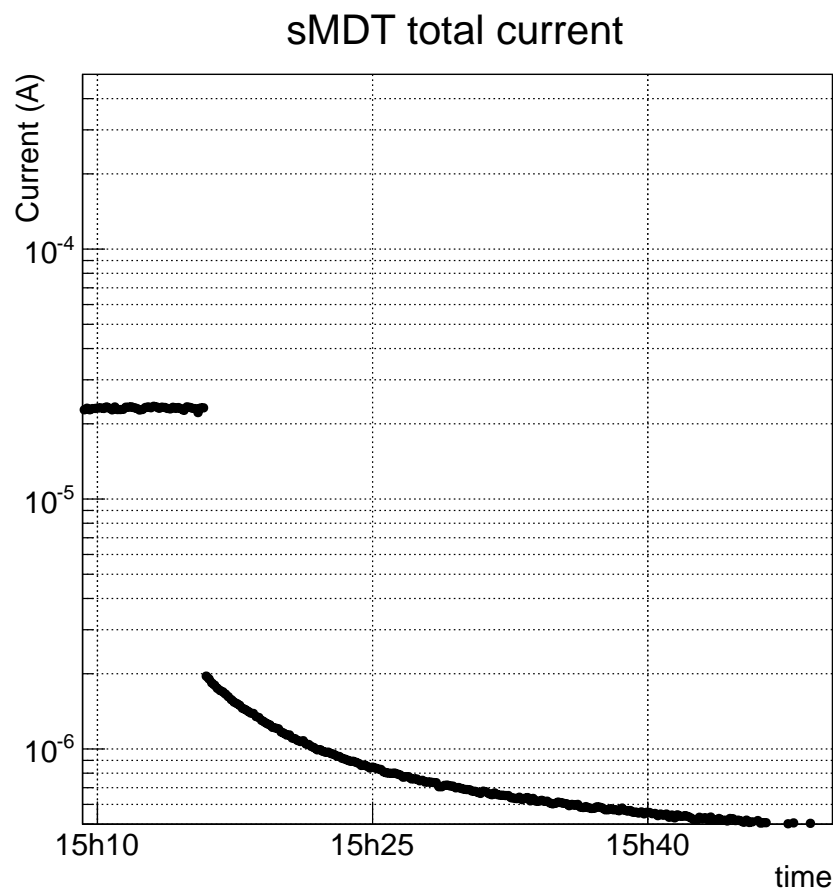
Figure 2.64: Evolution of the current drawn by the sMDT chamber at deactivation of the neutron irradiation in logarithmic scale. The curve immediately drops to about 10 % and then shows an exponential decay of the instable isotopes that were generated by neutron capture processes of the target material, detector vicinity and the chamber itself.

2.6.4 Muon track data analysis

In contrast to the irradiation measurements with a localized proton beam, in this setup all sMDT detector tubes are irradiated simultaneously. In addition the irradiating particle flux is a composition of neutrons and photons, the latter ones being created either within the beryllium target or any activated material in the detector vicinity. The relation between deuteron beam current and effective hit rates, including the different detection efficiencies of neutrons and photons, can be extracted from the previous chapter.

The following runs at different neutron and gamma irradiation levels have been taken and selected for analysis:
Figure 2.65 shows the drift time spectrum for cosmic muons, taken with 150 nA deuteron beam current. It illustrates the high probability of coincident irradiation hits with a cosmic muon trigger, which form the uniform background on top of which the muon drift time spectrum sits.
Investigating the number of tubes hit for each trigger in figure 2.66, it turns out that for the irradiation set of 100 nA deuteron beam current the mean value is around 13, reaching up to above 30, out of

date	deuteron beam current	all tubes current	muon triggers	tracks found
2011/11/07	65 nA	$14.61 \pm 0.02\ \mu A$	20963	10782
2011/11/08	100 nA	$21.90 \pm 0.04\ \mu A$	114903	48615
2011/11/08	150 nA	$33.92 \pm 0.05\ \mu A$	41100	12001
2011/11/09	150 nA	$33.01 \pm 0.02\ \mu A$	48405	13763
2011/11/09	0 nA	$0.4\ \mu A$	99384	54195

Table 2.8: List of neutron irradiation runs taken during November 2011. The high amount of events without reconstructed muon track is the result of a wide geometric acceptance of the trigger system. In addition, during runs at high irradiation levels, the large number of tubes hit may prevent a successful track reconstruction.
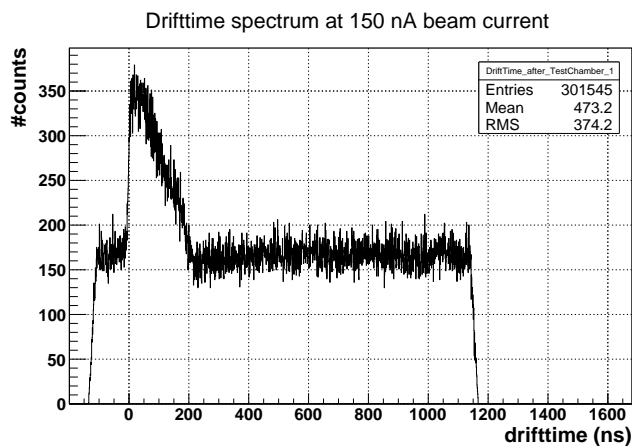

Figure 2.65: Drift time spectrum for all detector tubes at 150 nA beam current. The drift time spectrum for cosmic muons sits on top of a uniform distribution of random coincident irradiation hits.

46 tubes. When sorting out hits with an unreasonable drifttime outside the drifttime spectrum, the distribution becomes a doubly peaked structure as pictured in figure 2.67.

Events within the lower peak most likely belong to false triggers with background hits at a reasonable drifttime. Events with five or more hit tubes have a chance of resulting from a cosmic muon, crossing the six to eight active tube layers, depending on the detector position. The low yield of events with a reasonable number of tubes hit with good timing is the result of coincident triggers in all five scintillator layers, caused by background radiation, as well as the geometric acceptance of the trigger, that is larger than what is covered by the sMDT chamber.
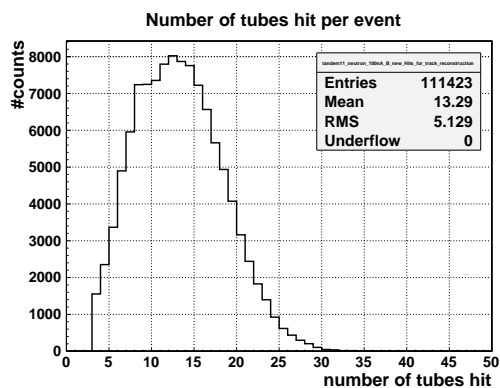
Figure 2.66: Number of tubes that were hit per event at a deuteron beam current of 100 nA.
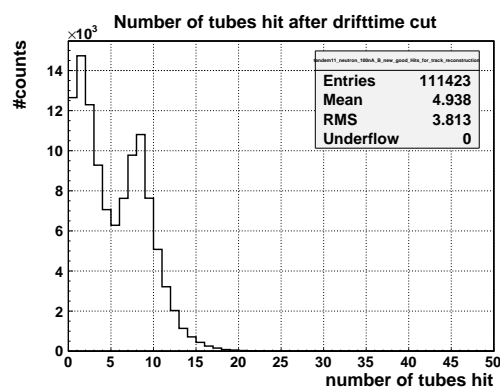
Figure 2.67: Number of tubes hit after a drift time cut, still including background hits that happen to have a reasonable drifttime, accumulating within the left peak.

Figure 2.68 shows the distribution of the track offset and slope parameters for the reconstructed muon trajectories. The y-coordinate distribution is even, and the full width of the detector is covered. The lower occupancy for the leftmost 20 mm is the result of the cut out tubes in this detector region (compare figure 2.29). The additional 15 mm-periodic structure can be explained by the geometric tube wall periodicity. Compared to the proton irradiation measurement in chapter 2.5.4 the distribution of track slopes is much narrower, due to the different geometric trigger configuration, and therefore the detector inefficiency due to the tube walls is more pronounced, as vertical muons hitting walls cross sensitive gas volume only in every second tube layer.
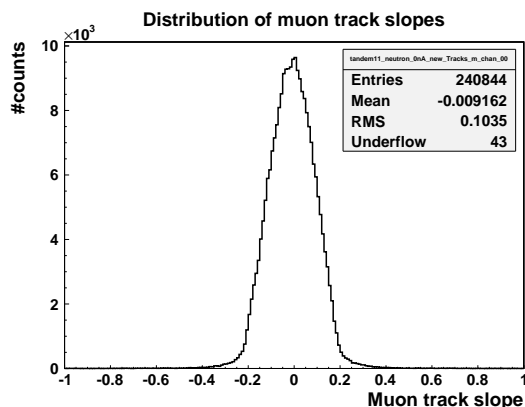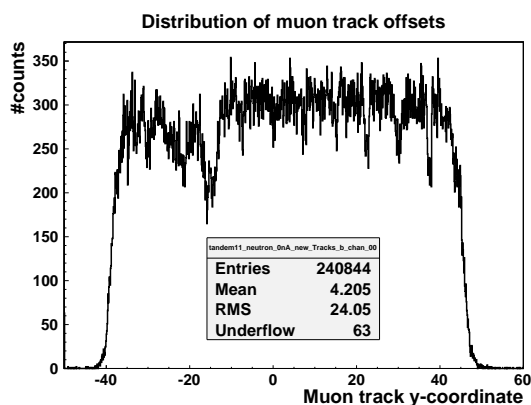
Figure 2.68: Distribution of the reconstructed muon track parameters offset and slope. Again the irregularities in the left third of the offset distribution matches the missing detector tubes in tis area.

The probability for each tube to detect a hit together with a muon trigger is shown in figure 2.69. With increasing irradiation rate the probability for a coincident neutron or γ hit together with a

cosmic muon increases. The occupancy is higher for tubes closer to the beryllium target, partly shielding the other tubes behind: compare the increased occupancy of the tubes 1, 7, 13, 23, 29, 35 and 41 with the numbering scheme in figure 2.26.

Figure 2.69: Detector occupancy at different irradiation levels. Increasing irradiation rate raises the probability for a coincident neutron or γ hit with a cosmic muon trigger. The effect is less pronounced for tubes on the far end of the detector.
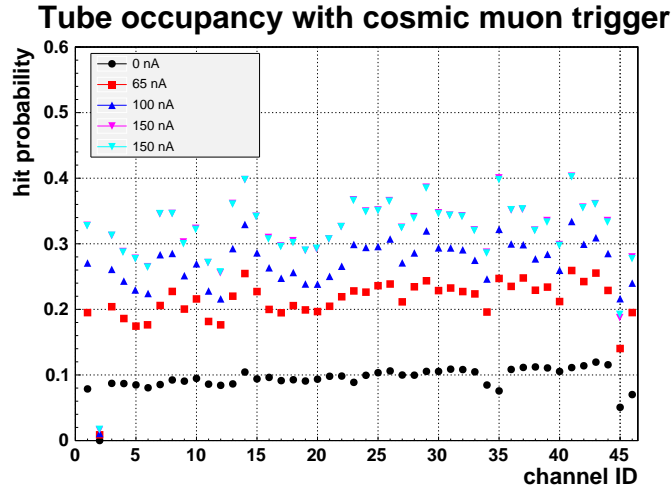
The single tube resolution for this measurement is again calculated iteratively. A single tube layer is excluded from the track fit, and this layer measurement is compared to the reference track. The resulting single tube resolution is used for the reference layers in the following iteration, until a stable value has been reached. See chapter A.1.3 for details, and figure 2.70 for the result.

The 3-σ-efficiency for the irradiated tubes is determined the same way as for the proton irradiation data, except for the fact that the whole chamber was irradiated, and thus no division into irradiated and unirradiated areas of certain tubes is possible.

The efficiency per tube is shown in figure 2.71. The residual determination in top and bottom tube layers relies mostly on track extrapolation, instead of interpolation, resulting in a lower efficiency value. To obtain results that are comparable to the proton irradiation measurements in chapter 2.5.6, the average tube efficiency is calculated for the four inner layers only, including the tube numbers 13 up to 34. See figure 2.72 for these values as a function of deuteron beam current.

Comparing the neutron measurements efficiency with the results from the proton irradiation and GIF measurements, the neutron efficiency value is about 2 to 3 % lower, independent from the irradiation rate. Whether this is the result of the averaging over the inner four layers or a systematic difference in the experiment setup could finally not be found out.

2.6.5 Electronic crosstalk analysis for neutron signals

The ATLAS MDT system ASD chip is designed in such a way, that only 1% of the analog signal on a given channel is coupled to the other channels of the chip [17]. This means, that if a signal on one channel is high enough, the crosstalk signal on the other channels can be above the discriminator threshold, and therefore a hit is registered without a particle crossing the corresponding tube.

This behavior has been investigated using the neutron irradiation data from the rate determination runs that use a random trigger to look for hit channels within a certain time window. For additional investigations of the ASD crosstalk effect see [36] and [37].

Mean single tube resolution
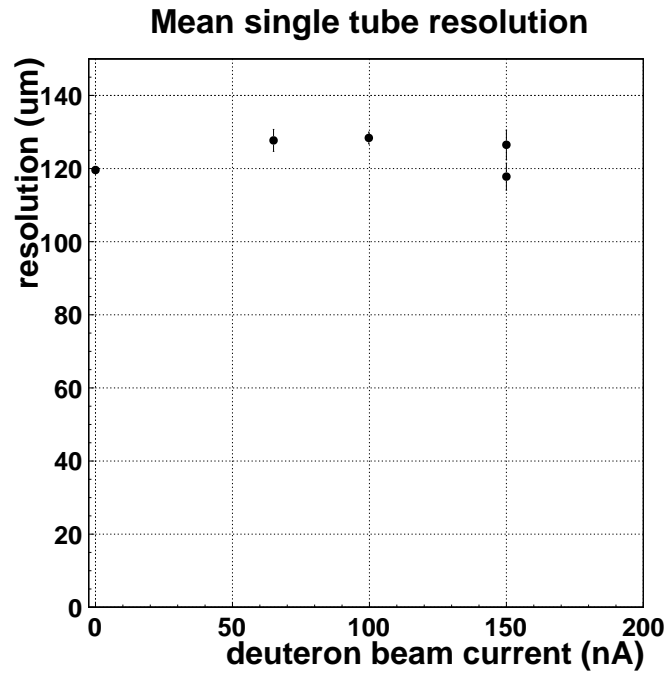
Figure 2.70: Mean single tube resolution of the fourth detector layer for different irradiation levels. The second measurement for 150 nA deuteron beam current shows a significant smaller better resolution value.
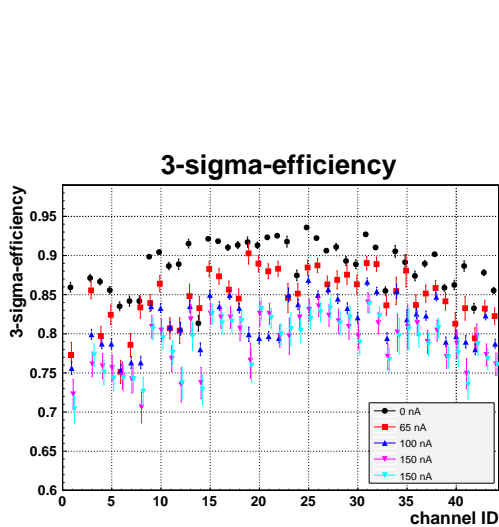
Figure 2.71: 3-σ-efficiency for all detector tubes with increasing deuteron current. The tubes of the outer layers show a reduced efficiency, due to the muon track extrapolation for the residual determination.
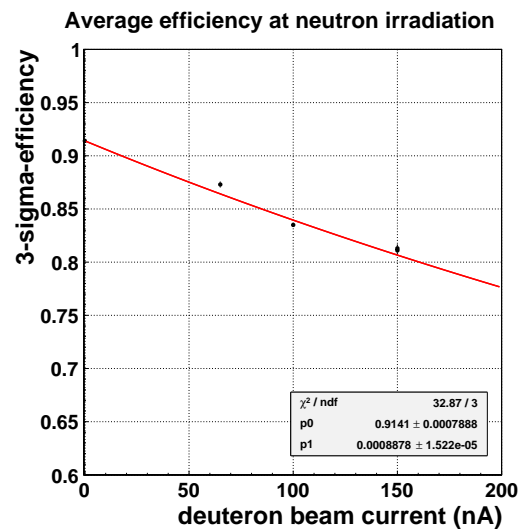
Figure 2.72: Average 3-σ-efficiency for the tubes of the inner four detector layers, determined by means of a horizontal fit from figure 2.71. The fit function drawn is $\varepsilon = \frac{p0}{1+x \cdot p1}$, to account for inefficiency due to deadtime effects, as in figure 2.50. For the corresponding hit rate see table 2.4 in chapter 2.6.2.

One of the three mezzanine cards of the 46 tube sMDT prototype detector is connected only to the four tubes of the fourth detector layer. These four tubes are connected to the channels 4 to 7 on one of the three ASD chips on the card. This leaves the other four channels of this ASD chip unconnected, as well as all channels on the other two ASD chips, and therefore these channels are investigated for crosstalk hits.

Figure 2.73 shows exemplary the number of hits for each of the 24 channels of the relevant mezzanine card on a logarithmic scale. As the channels 0 to 3 are not connected to a tube, it is obvious that the hits in these channels are the result of crosstalk.
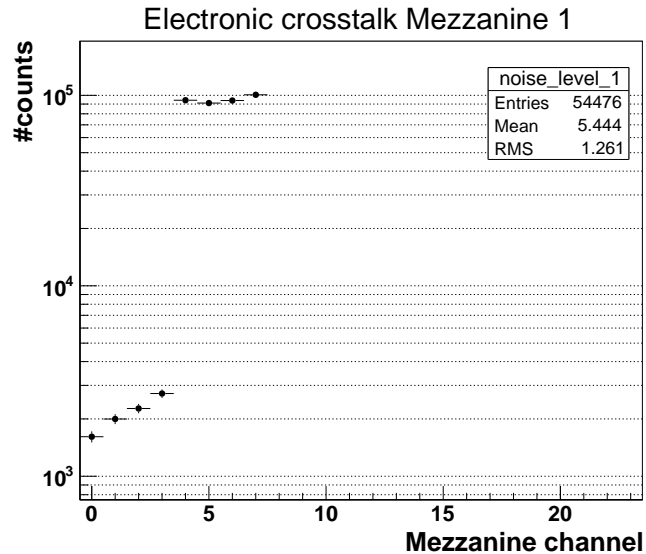
Figure 2.73: Electronic crosstalk within one ASD chip. Signals on channels 4 to 7 induce hits on the unconnected channels 0 to 3 on the same ASD chip.

A first result is, that no crosstalk from one ASD chip to another is found, so the crosstalk is happening only within a single chips die, and not within the pcb traces or the AMT chip.

In the following, a crosstalk probability is defined by the ratio of hits in channel 3 compared to its connected neighboring channel 4.

$$p_{\text{crosstalk}} = \frac{N_{\text{Hits ch. 3}}}{N_{\text{Hits ch. 4}}} \tag{2.17}$$

Figure 2.74 shows the crosstalk probability as a function of irradiation rate and absorber configuration. The crosstalk probability is mostly independent from the irradiation rate which is somehow expected because the fast shaping time of the electronics prevents a pile-up of analog signals at the investigated hit rates below 500 kHz per tube.

The irradiation flux composition on the other hand has a clear influence on the crosstalk probability.

A comparison with the neutron content of the registered hits is calculated in table 2.6. It shows a close correlation of the crosstalk probability with the probability of a hit being caused by a neutron. This observation suggests, that preferably a neutron hit creates enough charge in the tube to fulfill the crosstalk requirement of more than 100 keV [36] in the leading signal edge.

The computers used to control the sMDT chamber and to receive and to store the data from the chambers CSM board were located more than 10 m upstream the experimental location. Nevertheless, since commercial pc hardware is not designed in radiation hard technologies, these computers were
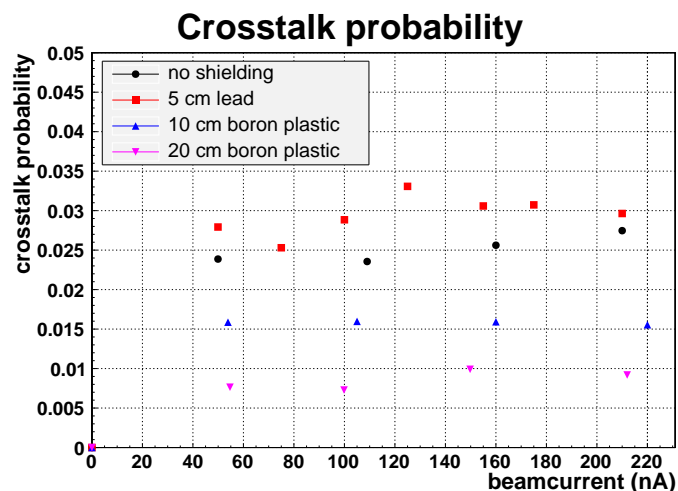
Figure 2.74: Evolution of the crosstalk probability from connected to unconnected channels within a single ASD chip with neutron irradiation rate for different irradiation flux compositions due to different absorber configurations.

found to respond with system crashes and "blue screen" error messages to excessive irradiation rates above 0.5 μA deuteron current.

But even at lower irradiation rates from 200 nA onwards, a corruption of the transmitted data was observable.

An indication for this is the reception of data from unconnected mezzanine cards. Figure 2.75 shows the hits detected during irradiation at 500 nA deuteron beam current, using 5 cm of lead as absorber material. Again, the unconnected ASD channels on the first two mezzanine cards, connected to several CSM channels below 50 show crosstalk on the 10^{-2} level. But additionally events at a 10^{-4} to 10^{-5} level are reported to be received for CSM channels above 71, where no mezzanine card was connected.

The only explanation for this is a corruption of the data words that indicate the origin of the event fragments, changing some values to the observed ones. This of course implies, that also other data words containing for example drift times and signal amplitudes can be the subject of corruptive modification.

This corruption can either happen on the CSM as source of these information, on the optical transmission line, or on the receiving side, the computer with the FILAR card connected to the optical fiber. It is likely, that this corruption appears on the FILAR cards FPGA with the following indication. After the reception of a massive amount of corrupted data, the receiving pc needed to be power cycled to restore the full functionality. Rebooting the machine without power cycle did not solve the issue, as the FILAR card FPGA is only reprogrammed with a power cycle.

Figure 2.75: Hit counts during noise measurement at 500 nA deuteron beam current and 5 cm lead shielding. Only CSM channels 1 to 72 are connected to mezzanine cards. Hits in all other channels are a result of data corruption.

2.7 Analog signal shape analysis for protons, photons and high energy neutrons

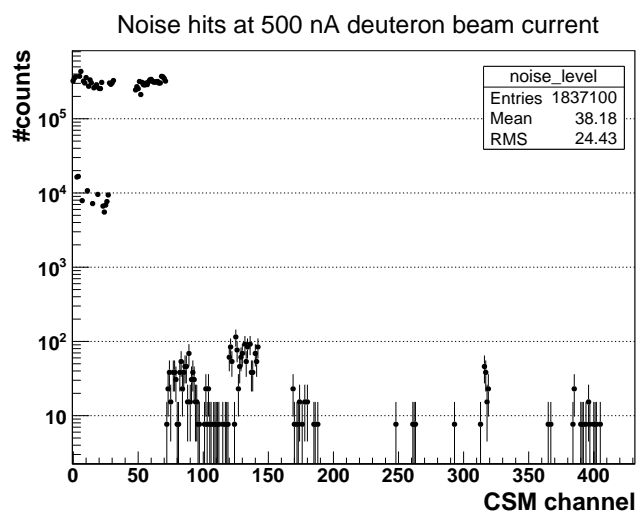The MDT ASD chip offers the possibility, to activate a dedicated output for monitoring of the analog signal of a single channel [17]. The signal is tapped right before the discriminator stage in the analog ASD chain. By installation of a low value resistor ($<$2 Ohm) on a mezzanine card (parts R108, R208 and R308), this output is enabled, and cables can be connected to the corresponding headers, see figure 2.76 The output driver has a relatively high impedance, so the absolute signal height must be interpreted with care and depending on the impedance of the connected equipment.
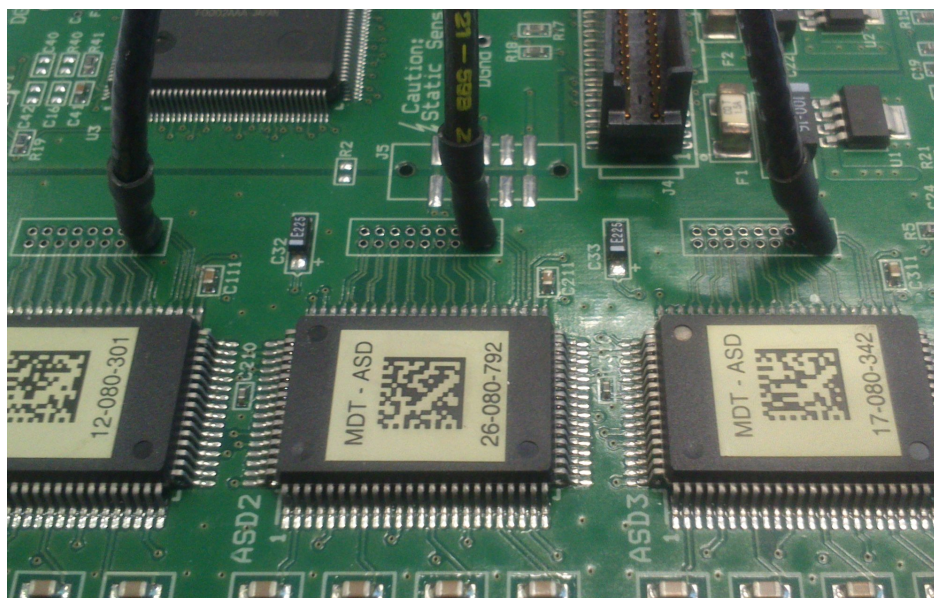
Figure 2.76: Three ASD's analog output headers on a Mezzanine card, soldered to wires for analog pulse shape diagnostics.

The analog output was connected to a fast gigasample flash-ADC VME module[8] to capture (s)MDT waveforms for different irradiation types. For a detailed description of a similar signal chain, see [21].

2.7.1 Neutron and γ pulseshapes

During the neutron irradiation beamtime described in the previous chapter, one of the mezzanine cards has been temporarily exchanged with a card, that contains all necessary modifications to observe the diagnostics analog output of a single channel.

The trigger was configured for the analog signal itself, with a (negative) threshold of 34 mV. See figure 2.77 for a schematic view of the setup. Note that due to the much lower efficiency of the sMDT tubes on neutrons, most signals recorded are γ signals, see chapter 2.6.3 for details.

It was an open debate about the MDT electronics whether the large charge signals that are created by high energy neutron recoil particles could saturate the analog ASD electronics on a long timescale, making the channel insensitive during this time. Aim of the measurements was therefore to search for exceptional long analog pulses in both polarities of the bipolar shaped signal. A typical analog signal waveform is shown in figure 2.78, together with the measurement variables.

The thresholds used for the determination of the (negative) time over threshold were -34 mV, and 25 mV for the positive time over threshold.

---

[8]CAEN v1729

Figure 2.77: Schematic overview of the neutron/γ analog pulse shape digitization setup. The dedicated monitor output of a mezzanine card is split, and fed to a discriminator and fast VME flash-ADC module.
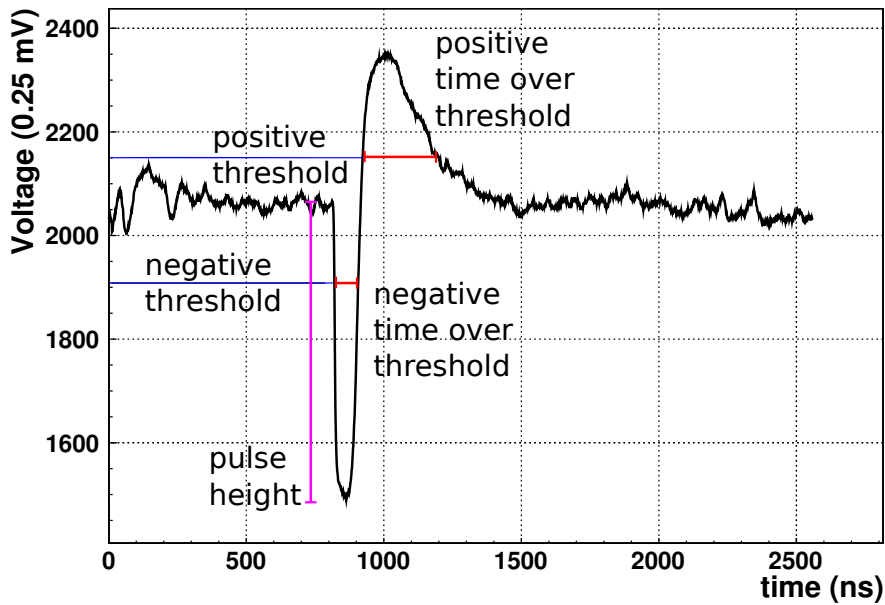
Figure 2.78: Typical examples of an analog signal shape during neutron irradiation. Indicated are also the measurement variables pulse height, time over threshold and positive time over threshold, that are used in the following analysis.

Figure 2.79 shows two more analog waveforms for a large signal with a clipped waveform, and two close-by signals.
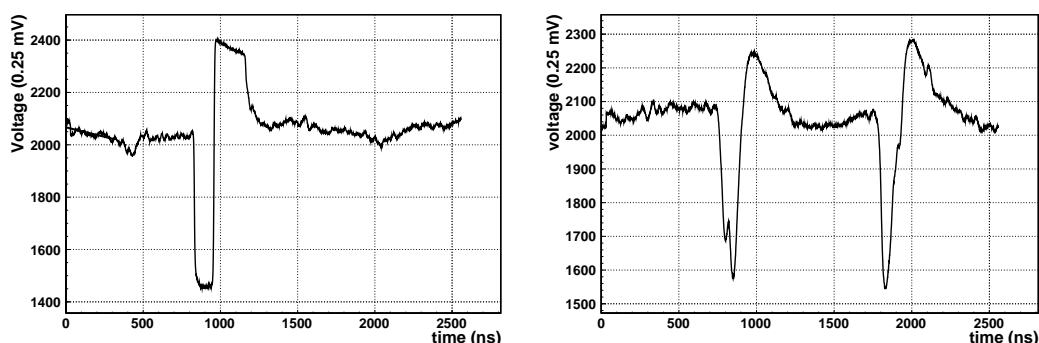
Figure 2.79: Examples of two other categories of analog signal shapes. The first image shows a very large signal, that is clipped by the ASD chip amplifier circuits. The second image shows two close-by signals with a distance of about 1 μs.

Table 2.9 lists the beam intensities at which signal shapes have been captured. Also shown are the resulting sMDT trigger rates.

Deuteron beam current (nA)	rate @34 mV threshold (kHz)	number of captured waveforms
0	1.7	10000
45	89.3	10000
100	206.5	5000
250	457.7	5000

Table 2.9: List of runs taken for neutron signal shape analysis

The trigger rate at 0 nA beam current is the result of noise hits due to the prior activation of the detector material during the beam time. The sMDT HV current exceeded 50 μA for all tubes at 250 nA beam current, and the ISEG SHQ high voltage power supply tripped during a measurement at 500 nA beam current due to overload.

Figure 2.80 shows the histograms for the measured pulse height and time over threshold for negative and positive pulse.
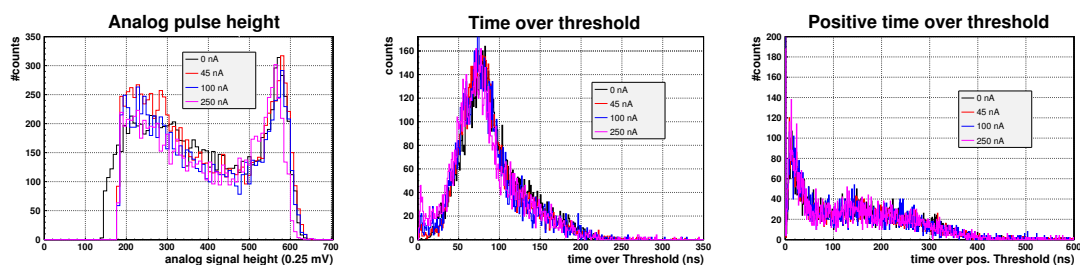
Figure 2.80: Histograms of analog pulse height and width of both polarity signal contributions, as an overlay for different irradiation rates. The run at 0 nA has been taken at alower signal threshold, and this is why the corresponding pulse height histogram has entries at lower values. Apart from that, no difference in shape distribution is perceptible, especially no exceptionally long signals are observed even at highest irradiation rates.

The signal height for 0 nA beam current has been taken at a lower threshold, therefore the histograms

differ on the low end. At 250 nA beam current, a slight reduction of the signal height is observed, again due to gain drop effects.

There is no observable difference for the distribution of pulse duration for both bipolar signal pulses, and therefore no sign of exceptional long signal shapes within the accumulated statistics.

2.7.2   Proton pulseshapes

Not only sMDT signal shapes under neutron and γ irradiation have been recorded, but also the shape of proton signals for both MDT and sMDT tubes.

To trigger on the incident tandem accelerator protons, a scintillator with photomultiplier tube has been placed behind the single (s)MDT tube. Using the same setup with the modified mezzanine card as described in the previous chapter, the pulse shape of proton signals has been captured at different irradiation rates. See figure 2.81 for a scheme.
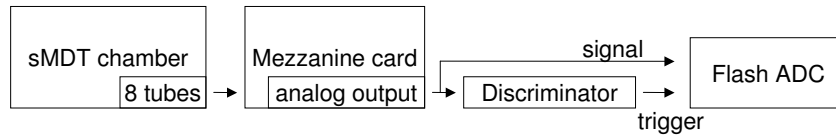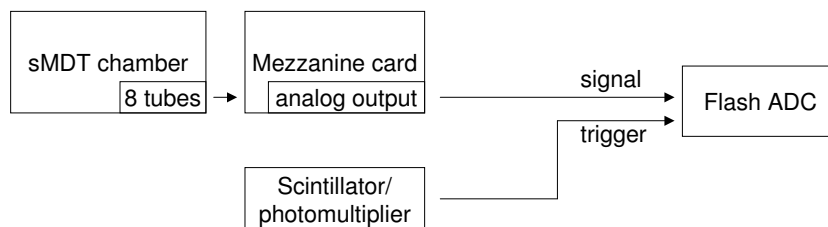

Figure 2.81: Schematic overview of the proton analog pulse shape digitization setup. The dedicated monitor output of a mezzanine card is fed to a fast VME flash-ADC module, whereas a scintillating tile served as trigger.

Figure 2.82 shows the distribution of proton signal heights for both 30 mm and 15 mm tubes at different proton irradiation rates. The proton rate has been measured counting the scintillator signals during a 100 s period. Due to small fluctuations within the accelerator chain, the rates were not absolutely constant, and the values should be considered as more qualitative measurement.

Figure 2.82 shows an overlay of the signal height distributions at different proton irradiation rates for both MDT and sMDT tubes.
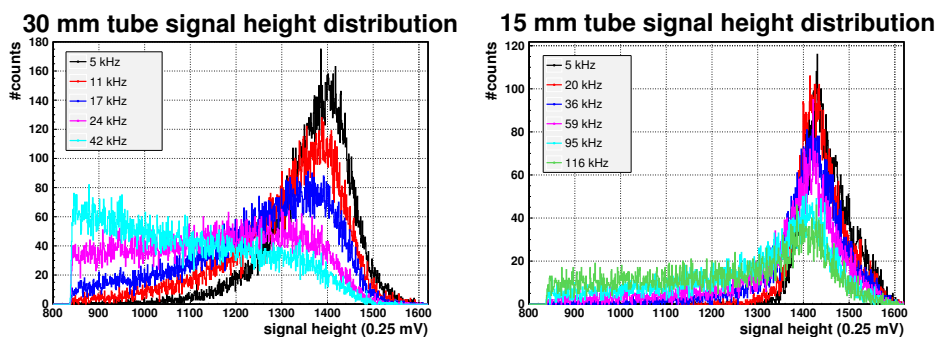
Figure 2.82: Degradation of analog signal height due to gain drop effects for 30 mm tubes (left) and 15 mm tubes (right) at different proton irradiation rates. Note the different color coding, with the much higher rates for 15 mm tubes and a lower gain drop effect at the same time.

The different degradation of gas gain per tube due to ion space charge effects can be clearly observed. While the signal pulse height remains mostly unchanged in the case of 15 mm tubes, with only a small shift of parts of the spectrum towards lower values, the 30 mm tube signals reduce significantly in height, such that the spectrum moves even partly below the signal threshold.

This clearly shows the much higher rate capability of the sMDT detector technology, compared to the 30 mm MDT tubes.

Chapter 3

Development of ATLAS compatible readout electronics for Micromegas detectors

The New Small Wheel (NSW) project has been approved by ATLAS, with Micromegas detectors as the technology foreseen for precision tracking, to be installed during the LHC Long Shutdown 2 (LS2). See figure 3.1 for the present LHC time schedule. Micromegas detectors and the NSW project are introduced in chapter 3.1.
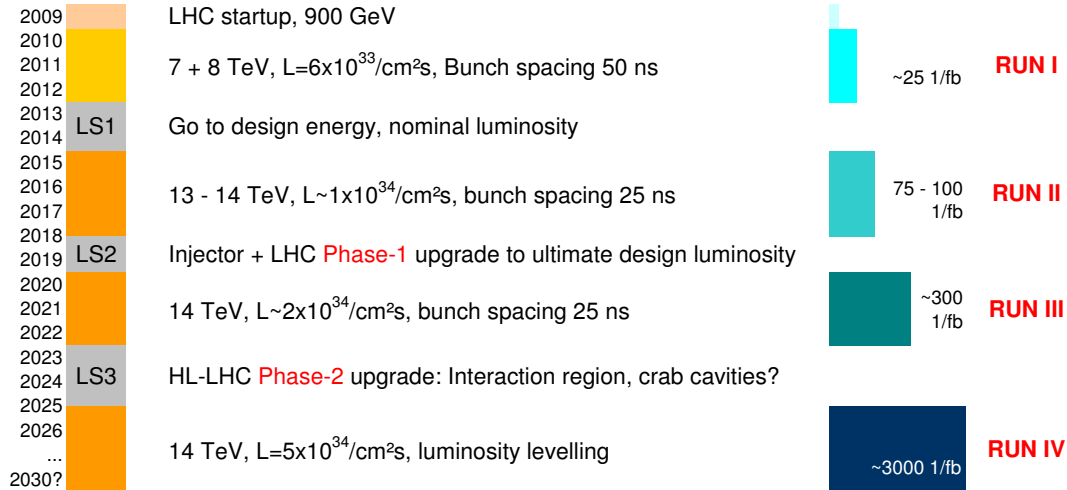
Figure 3.1: LHC upgrade and run period schedule. The installation of the New Small Wheels will take place during the LS2 period.

This schedule offers the opportunity to install a pre-series Micromegas chamber already during the LS1 shutdown period in the available space on a Small Wheel Cathode Strip Chamber. This Micromegas chamber will then be read out together with the other ATLAS subsystems for a combined data analysis during the Run II period. Therefore it is necessary to interface this Micromegas chamber to the ATLAS data taking infrastructure, which allows to compare its measurement with the ATLAS event reconstruction on an event-by-event basis.

For this task, an ATLAS Read Out Driver (ROD) firmware has been developed by the author, that enables the readout of Micromegas detectors and the complete integration into the data stream of all other ATLAS subsystems.

Chapter 3.4 describes this firmwares functionalities, together with the different implemented communication interfaces.

The ROD functionality itself, as well as the integration of the various functional blocks into the system have been designed and performed by the author, whereas the firmware modules for SLINK, DTCC and Ethernet communication have been contributed by other collaborators.

To better understand the infrastructural environment of such a Read Out Driver, the ATLAS trigger and data acquisition system is described in chapter 3.2.

As the ATLAS detector and its electronics have been designed around the late years of the 20st century, significant gain in electronics performance has been achieved by industry, compared to the components used back then. Computing power and resources of programmable logic components have improved dramatically over the last decade, together with a reduction of size, cost and power consumption. This allows an enhancement of readout and data processing functionality at reduced complexity, cost and component count.

The firmware runs on a modern Virtex[1]-6 FPGA, that is housed by a component of the Scalable Readout System (SRS), that has been developed by the RD51 collaboration as a powerful multiple purpose detector data collection and processing tool. The SRS is introduced in chapter 3.3.

---

[1]Trade mark of Xilinx, Inc.

Several experimental test scenarios of the SRS system with the ROD firmware are presented in chapter 3.5.

3.1 Micromegas detectors for the NSW

3.1.1 Working principle of Micromegas detectors

Micromegas detectors were originally proposed by Giomataris, Charpak et al. [38] as high-granularity position-sensitive gaseous detectors for high particle-flux environments. A summary of the working principle is as follows.

The active volume of the detector is separated into a drift volume and an amplification volume by means of a fine porous metal mesh, see figure 3.2.

Two different voltages are applied to the active volume, to create a moderate drift field in between cathode and mesh, and a high amplification field in between mesh and strip anodes. Electrons generated by ionizing particles in the drift region move towards and through the mesh due to the electric field configuration. When the electrons enter the amplification region, an avalanche amplification process starts due to the high electron acceleration by the electric field.

The electric signal of the electron avalanche is picked up by copper strips and fed to readout electronics for further amplification and measurement. The fact that the ions generated during the avalanche process only drift the relatively short distance to the mesh for neutralization, but do not (mostly) enter the drift volume, makes this approach much more high-rate tolerant as traditional drift chamber detectors.
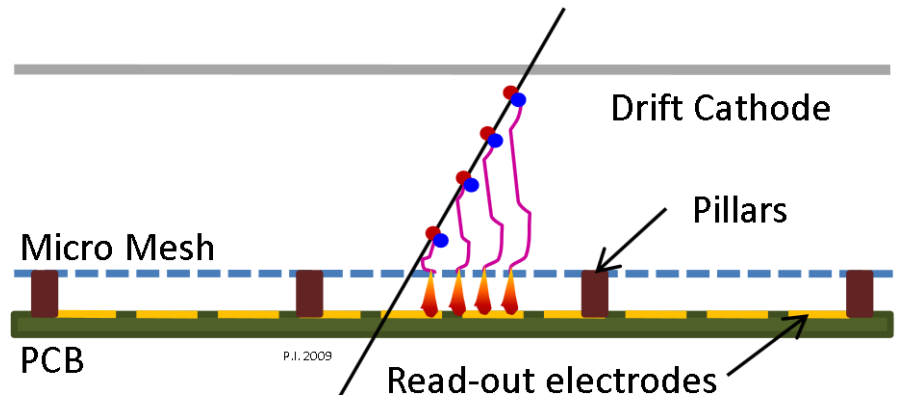
Figure 3.2: Functional principle of Micromegas chambers [8].

In case of a high amount of ionization in the drift region (for example by the stopping of an α-particle or recoil nuclei), the amount of charge generated in the amplification region can be large enough to temporarily create a conductive path between mesh and anode strips, referred to as discharge or spark. Despite being non damaging, this discharge induces a dead time of the detector during the recharge of the mesh capacitance. To cope with this effect, and to improve reliable operation, a modification of the Micromegas layout has been proposed [39] that includes an additional layer of strips, made from highly resistive material. This additional strip layer on top of the copper strips prevents the complete discharge of the mesh capacitance, but maintains the coupling of the signal onto the readout strips below. Figure 3.3 illustrates the concept.

Due to electron diffusion in the drift volume of the Micromegas detector, the charge from a muon hitting the detector perpendicularly is spread over few strips, depending on the drift gap width and
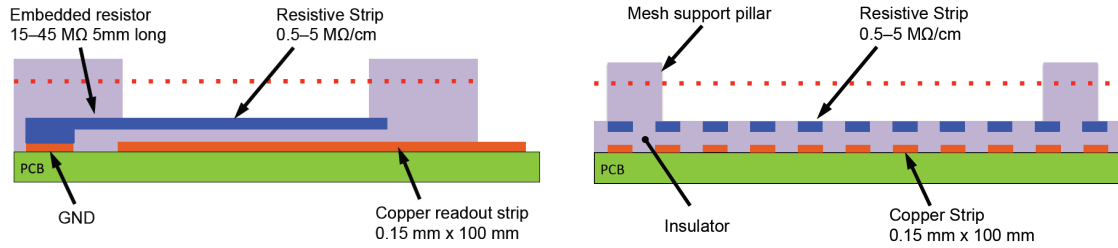
Figure 3.3: Micromegas resistive strip anode layout [39]. The application of an additional layer of strips, made from high resistivity material, prevents the complete discharge of the mesh capacitance in case of a discharge.

strip pitch. In this case, a weighted sum of the charge induced in the different readout strips can be calculated to determine the particle position on a sub strip pitch resolution (centroid method).

With increasing incident angle this resolution degrades, due to the additional geometric spread of the drift electrons over additional strips, as indicated in figure 3.4. This can be corrected for by evaluating the electron drift time on the different strips in a fashion very similar to what is performed within Time Projection Chambers. The method is consequently called micro-TPC mode, or μ-TPC.

The first strips measuring a signal can then be used to calculate the incident point in the readout plane, whereas the later strips, together with the drift velocity of the electrons, can be used to reconstruct the particle angle within a single detector layer.

The combination of both methods, centroid and μ-TPC, ensures a tracking resolution better than 100 μm over a wide range of incident angles at a strip pitch of $\sim$400 μm, as indicated in figure 3.5.
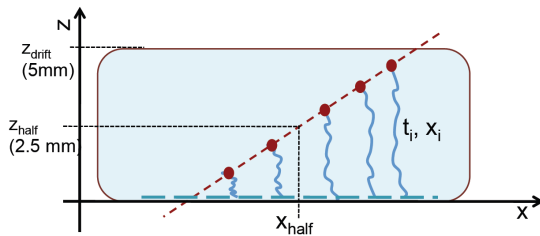
Figure 3.4: Application of a Time Projection Chamber like reconstruction of the track angle by the different arrival time of electrons at the readout plane. [8]
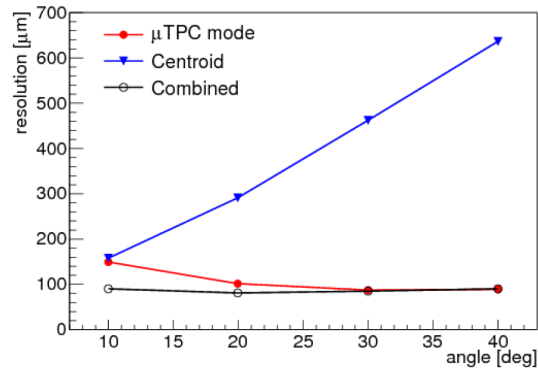
Figure 3.5: Resulting spatial resolution for the combination of centroid and μ-TPC mode over a range of particle incident angles. Using readout planes with $\sim$400 μm strip pitch, a value better than 100 μm can be achieved. [8]

3.1.2 Layout of the New Small Wheels

The New Small Wheels will be built from 16 sectors each, 8 large ones and 8 small ones, overlapping each other for full coverage.

Each sector is a sandwich structure of two times 4 layers Micromegas detectors around a passive spacer, with a sandwich of two times 4 layers of sTGC detectors, see figure 3.6. The two detector technologies work completely independent from each other, allowing a fully redundant readout and triggering for a total of 16 sensitive layers. With the sTGC detectors being the default choice for triggering, they occupy the outer layers in the sector layout for maximum distance and lever arm on

the track angle measurement for triggering.

Each of the Micromegas quadruplet sectors consists of an inner and outer module, with a size of up to 3.1 m^2.

Drift – 10 mm

Spacer – 40 mm

sTGC – 70 mm

Double faced drift – 20 mm

Read-out – 10 mm
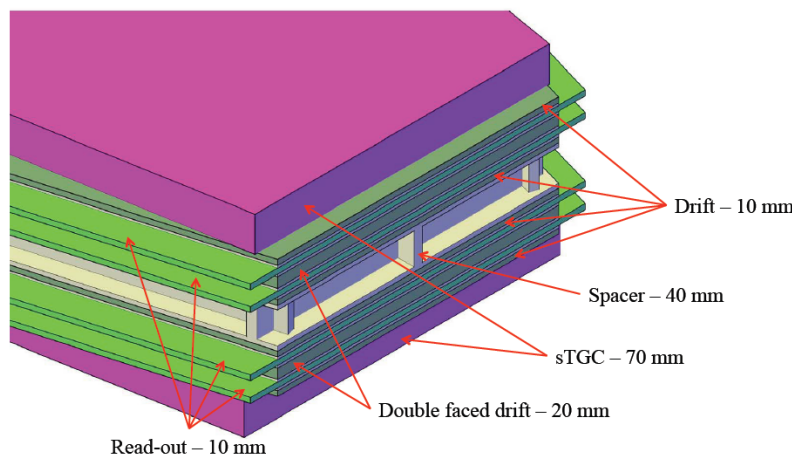
Figure 3.6: Sketch of the different detector layers within each of the 16 wedges per wheel. sTGC detector layout is simplified and the total amount of detection layers per wheel is 16, in which 8 are Micromegas. [8]

The different panels, that together form a quadruplet, mainly consist of standard printed circuit board epoxy-fiberglass laminate of type FR4, glued to a stiffening structure of aluminum honeycomb material. Those FR4 sheets of 0.5 mm thickness can be obtained from the electronics industry, already equipped with the copper strips and alignment markers of high precision.

3.1.3   Readout electronics for the New Small Wheels

The NSW chambers will be equipped with VMM3 frontend electronic chips, a dedicated development of Brookhaven National Laboratory (BNL) for the ATLAS NSW detectors. Micromegas and sTGC detectors make use of the same chip to reduce the development cost, and the chip is designed to serve both technologies equally well. Promising tests have been performed with the predecessor version VMM1 [40] of the chip, and the VMM2 is being produced during the time of writing this thesis.

The VMM2 chip features include 64 input channels with charge-sensitive preamplifier with adjustable gain and shaping time, discriminator and digitization of peak amplitude and timing. The on-chip digitization and extraction of relevant pulse parameters allows an effective zero suppression and minimization of bandwidth at high count rates.

A scheme of a Micromegas layer, equipped with the different electronics components is shown in figure 3.7.

The time schedule for the NSW development, construction and commissioning is shown in figure 3.8. The construction of the modules zero at the different construction sites is foreseen for the second half of 2014, followed by the series production in 2015 and 2016. The New Small Wheels are planned to be installed in ATLAS in the end of 2018, followed by one year of commissioning.

3.2   The ATLAS trigger and data acquisition system

Within the ATLAS detector, particle bunches collide at a rate of 40 MHz. At the run conditions up to 2013, an average of 21 particle interactions [6] happened per bunch crossing (pile up), resulting in nearly 1 GHz of particle interaction rate. Since the raw data rate of the detector at this frequency is

Figure 3.7: Single Micromegas plane with electronics board arrangement. [8]

Figure 3.8: Schedule for the construction, installation and commissioning of the New Small Wheels.
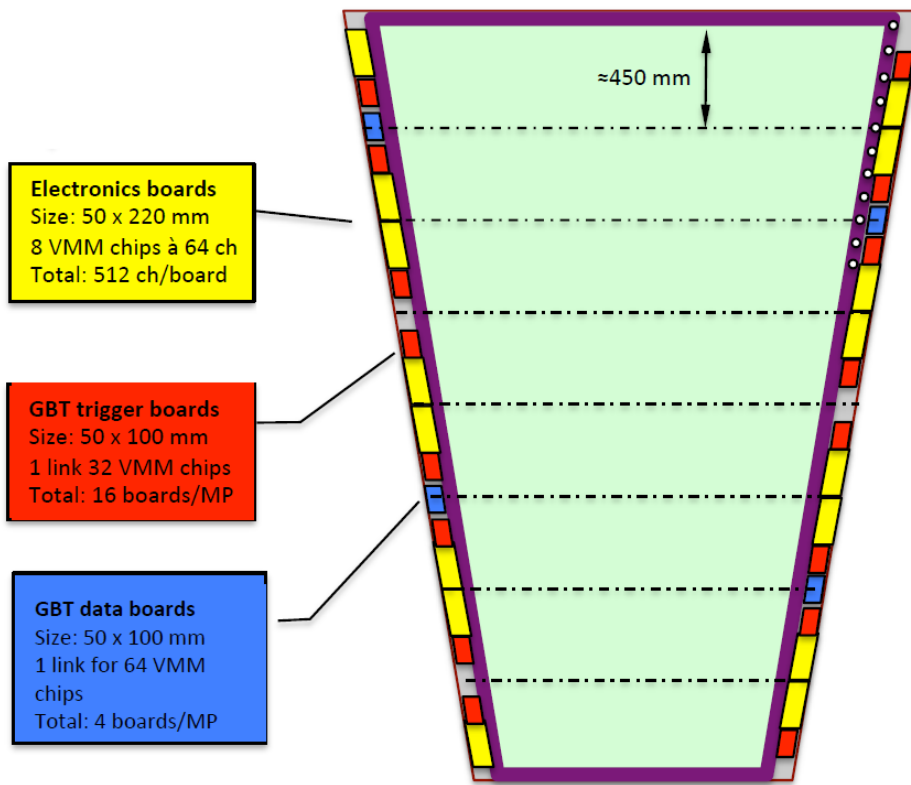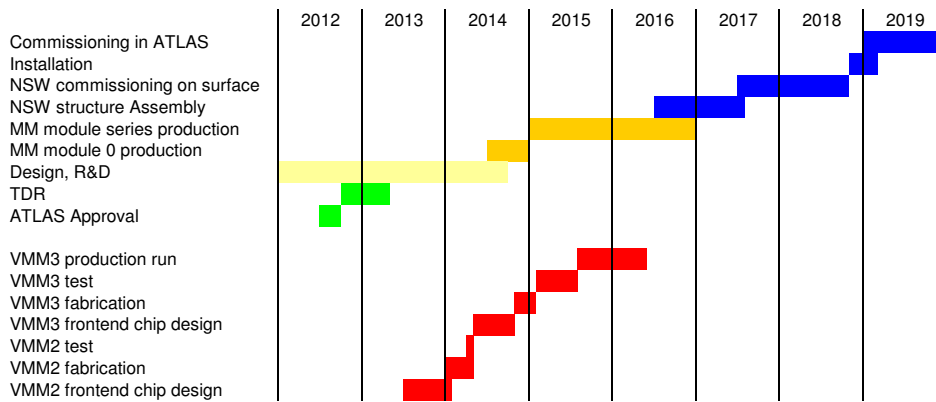
in the range of TBytes/s and thus far too much to be stored completely, the ATLAS experiment uses three stages of triggering mechanisms, to reduce this data rate to a manageable level.

To keep track on the different data from the various subdetectors, passing several stages of processing, a unique set of numbers is introduced to each event.

The following section roughly describes how the ATLAS data acquisition system works, see figure 3.9 for a simplified model.
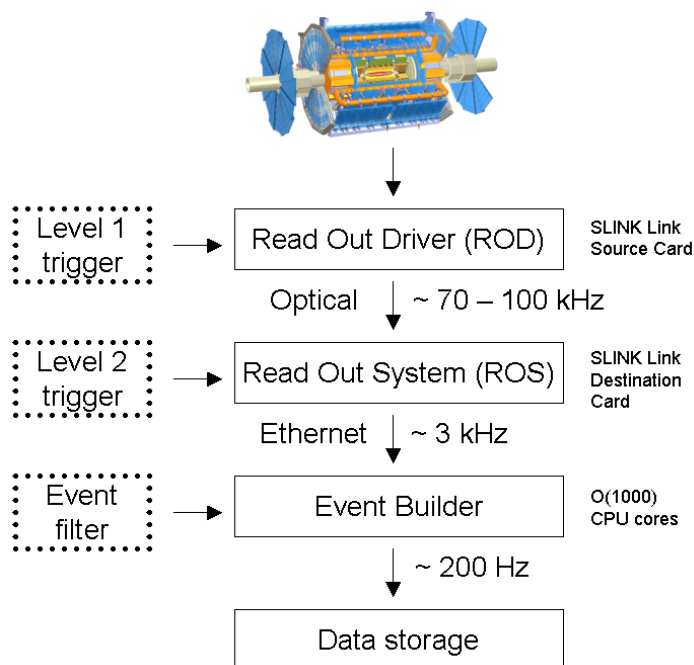
Figure 3.9: Simplified model of the ATLAS data acquisition chain.

With every bunch collision, the different subdetectors store raw data for all channels in their frontend electronics, either analog or digital. Due to the limited depth of memory at this high granularity and channel count, data can only be stored for a few μs.

Parts of the calorimeter and muon systems do not only store their data, but also send them to dedicated hardware triggering systems. Based on these data and a weighting combination ("Trigger Menu") of different measured parameters, a decision is met, whether to consider that particular event for further processing or not. This decision takes a constant time of about 2.5 μs ("L1 trigger latency") and the acceptance rate is limited to 70 kHz. This step is called the first level, or level 1 trigger (L1). During the LS1 shutdown it is foreseen to raise this rate to the design value of 100 kHz.

The L1 acceptance signal from this Central Trigger Processor (CTP) is distributed by an optical tree network to the Read Out Driver boards (ROD) of all different subdetectors. For each of these L1 triggers, the Read Out Drivers read the complete raw data from all detector channels that have been stored during the L1 trigger latency. All raw data not matching a L1 trigger are discarded by the frontend electronics at this point.

Raw data from all detector channels read by the RODs for each L1 trigger is then checked for integrity or errors, eventually processed and formatted as ATLAS ROD event fragment [41] (see figure 3.20). The event format also includes a consecutive 24-bit L1 trigger number, that is part of the "Extended Level 1 ID". This Number is used later, to merge correctly data from all subdetectors, matching a L1 trigger decision.

Data from multiple RODs of a single ATLAS sub detector is then pushed to dedicated PCs, that form the Read Out System (ROS). Each of these ROS PCs houses up to four ROBIN [42] cards, allowing data reception from up to three RODs, for a total of twelve Read Out Links (ROL) per ROS PC. Data

transmission is realized as SLINK [43] over optical fiber.

These ROBIN cards temporarily store the ROD data, and present part of it to the Level 2 trigger system upon request, based on Regions Of Interest (ROI) defined by the L1 trigger system.

ROD data for the regions of interest are transmitted to the level 2 trigger (L2) PC farm via ethernet. These L2 PCs perform a partial event reconstruction on each of these events, and decide whether to keep that event or not within ~10 ms. The L2 accept rate is at about 3 kHz and L2 triggers are propagated to the ROS PCs, still buffering all L1 data that are now either discarded (L2 reject), or read out of the local buffer (L2 accept).

Now the complete ROD event data for each L2 trigger are sent to the Event Filter (EF) PC farm, that further reduces the event rate to a final 200 Hz, which are then stored do hard disks. This last step is performed completely on commercial PC and Ethernet Infrastructure, no custom hardware systems are involved. With an event size of approximately 1.6 MB, the ATLAS data stream to be stored on hard disks is around 320 MB/s.

3.3   The Scalable Readout System SRS

The Scalable Readout System (SRS) project has been started by the RD51[2] collaboration in 2008. Since then, it has been continuously improved, and new components have been added.

The development has been driven by the need for a flexible and scalable electronic readout system to read different particle detectors with different frontend chips. A schematic view of the main SRS components is shown in figure 3.10.
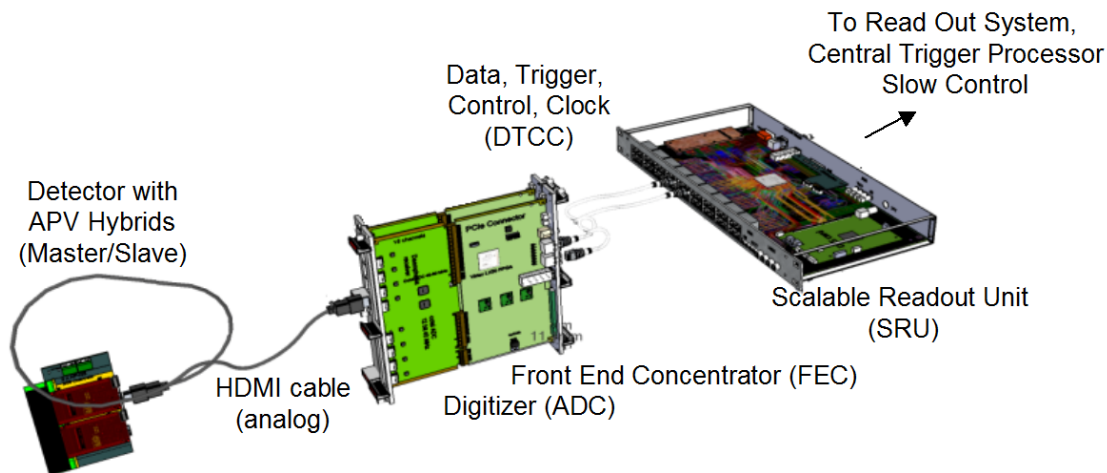
Figure 3.10: Schematic view of different Scalable Readout System (SRS) components

The very first component in the data acquisition system of a particle detector is the frontend chip, which is mostly an application specific chip (ASIC), specialized for the individual detector type (semiconductor, gaseous, etc). In the SRS system, this chip is mounted on a hybrid board (see figure 3.17) that is connected to the detector via a Panasonic brand connector[3]. This common connector ensures the possibility to exchange the type of frontend chip, without modification of the detector itself.

The connection type from the frontend chip carrier to the next acquisition board, as well as this board itself depends on the type of chip. In case of an analog frontend chip, data needs to be digitized by an Analog to Digital Converter board (ADC), that is accompanied by a Front End Concentrator card (FEC). Digital frontend chips use a similar card to connect multiple frontend hybrid cards to the

---

[2]www.cern.ch/rd51-public
[3]part number AXK5SA3277YG

FEC board. Upstream from this adapter card, all detector types use the same infrastructure, so only the hybrid board and eventually the adapter card (analog, digital or binary readout) are generic to a certain frontend chip.

FEC and ADC card use standard mechanic form factors, and fit 6U x 220 eurocrates or custom smaller crates. The whole system can use standard commercial off-the-shelf ATX computer power supplies to power electronics and frontend chips. An adapter card is needed to mate with the ATX 24 pin connector, filter noise and to generate the non-ATX standard +1.8 V and +4.2 V power rails via series-diodes, mounted on heat sinks. An additional switch-mode power supply is needed to generate the -5 V rail for the symmetric supply of the ADC card equalization circuitry.
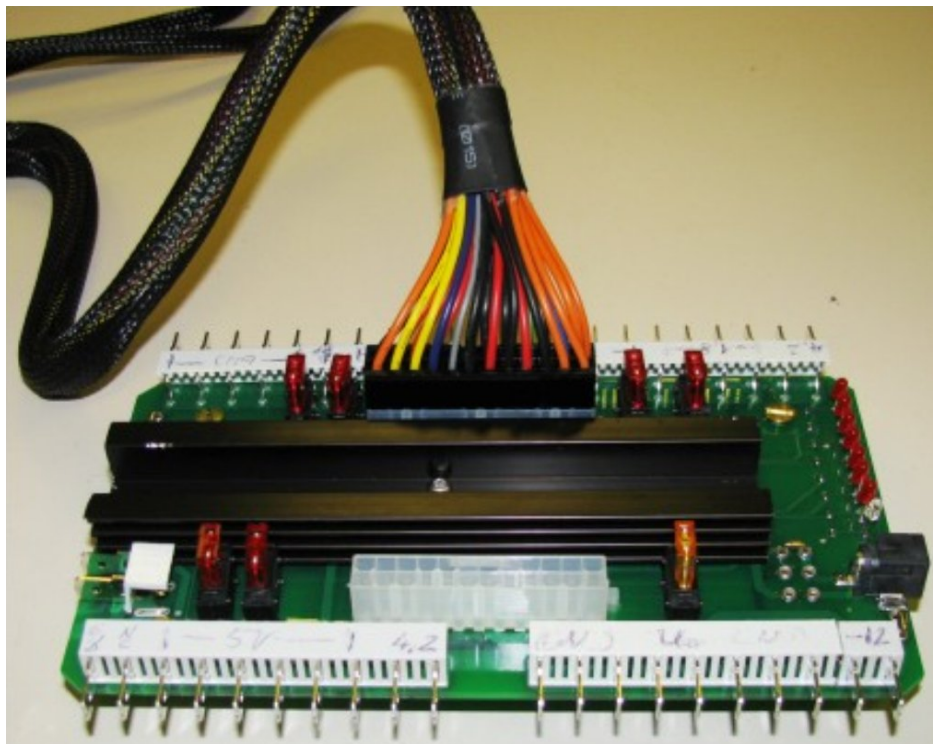
Figure 3.11: ATX power adapter board with standard 24 pin ATX connector, fuses and power rails for SRS supply.

If no other channels are explicitly implemented, all communication in between the data acquisition back-end computers and the SRS is handled using UDP packets[4] over IP ethernet. In this way standard commercial network cards, switches and cables (copper or fiber) can be used to read a large system of several FEC cards and thousands of channels. In addition, several software solutions are already available, that can be easily migrated to other frontend chips and detector technologies.

Systems can be upgraded to a higher channel count just by adding additional frontend hybrids and FEC cards. Once the channel count exceeds the available ethernet network bandwidth, or additional processing resources or connectivity is needed, one or several SRU (Scalable readout Unit, see chapter 3.3.3) boards can be added to the system (see figure 3.12).

The SRS system makes exclusively use of direct links for data transmission instead of bus systems (like the outdated VME bus). This allows a more reliable and scalable operation at higher bandwidth, without the risk of global failures.

---

[4]All network accessories need to support Jumbo Frames for data packets larger than 1500 bytes
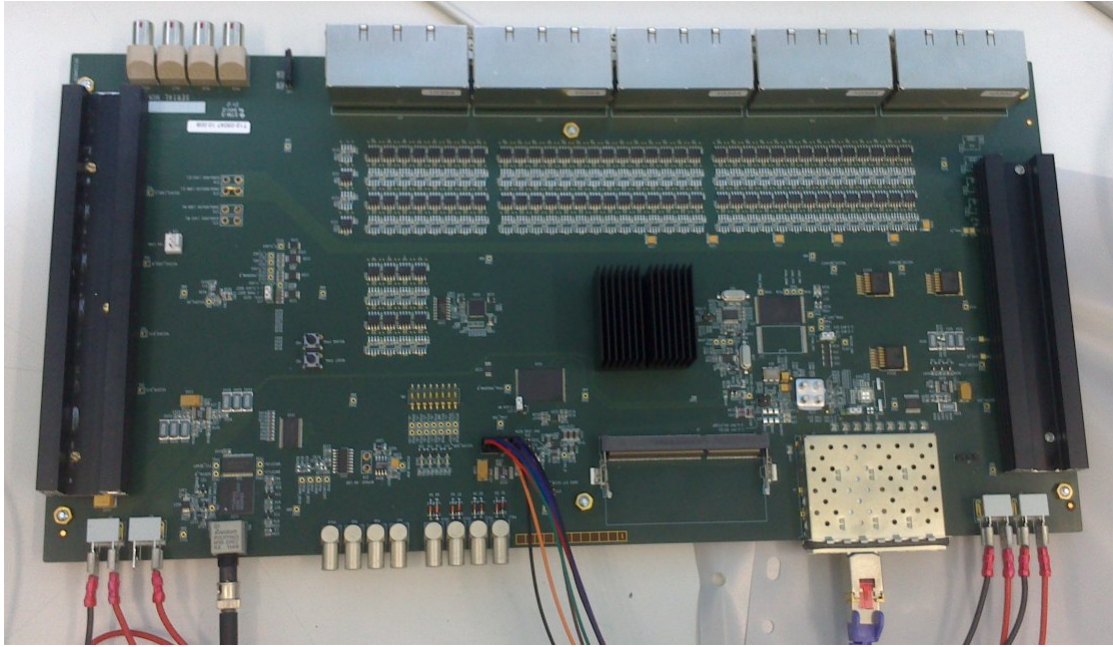
Figure 3.12: An SRU board, with the Virtex-6 FPGA under the central heat sink. Also visible is the TTCrx receiver ASIC in the lower left corner and the quad SFP+ cage in the lower right corner. The upper part of the board is occupied by the 50 RJ45 plugs with their corresponding LVDS transceivers. The main SRU linear voltage regulators are located under the large heat sinks on the SRU borders.

3.3.1   APV25 Frontend Hybrid

The APV25 [44] is a 128 channel analog frontend chip, developed for the silicon tracking detectors of the CMS experiment. It contains 128 channels, each of them consisting of a charge-sensitive preamplifier, shaper and analog pipeline memory. Sampling is performed synchronously with the LHC bunch-crossing clock of 40.08 MHz. See figures 3.13 and 3.14 for the corresponding schematics of the chip.

Although the APV25 has been developed for charge determination in semiconductor sensors, it was successfully adopted to gas detectors like GEM or Micromegas. In this case for example the default signal shaping time constant of 50 ns might be reconfigured by the user.

With every clock cycle, the charge signal at each channel is fed through the preamplifier and shaper stages and stored in a 192 cell deep analog pipeline memory. A special register within the APV25 accommodates for the (constant) Level 1 trigger latency, so once the L1 signal arrives at the APV25, the pipeline cells matching the physics event that caused the trigger, are flagged for readout. Unflagged cells are overwritten with new analog values, once the 192 cell deep chain wraps over, so the maximum L1 trigger latency is allowed to be 192×25 ns $= 4.8~\mu$s. See figure 3.16 for a timing diagram for the APV25 readout delay.

As already mentioned in Chapter 3.3, APV25 chips are used on hybrid chip-carrier boards of the SRS system. These boards also include all necessary circuitry around the APV25 chip:

1. The HDMI cables connected to the FEC/ADC card feed 3.3 V to the APV25 hybrid boards[5]. There, onboard voltage regulators generate the 2.5 V and 1.25 V for the APV25 chip.

2. Occasional discharges in the micro pattern gaseous detectors can generate potentially destructive amounts of charge at the input stages of the frontend chip. Therefore a network of protec-

---

[5]To compensate for the voltage drop on very long HDMI cables, the FEC/ADC cards can be modified to feed 5 V instead of 3.3 V to the hybrid boards.

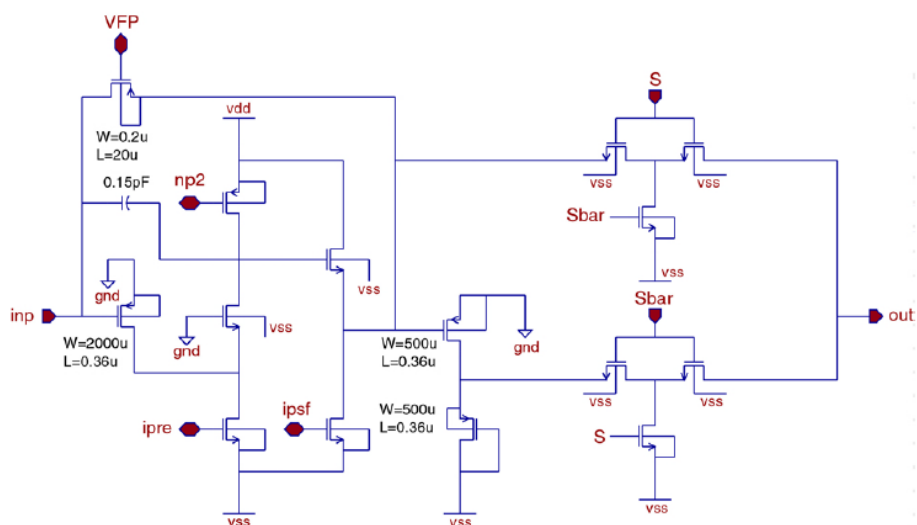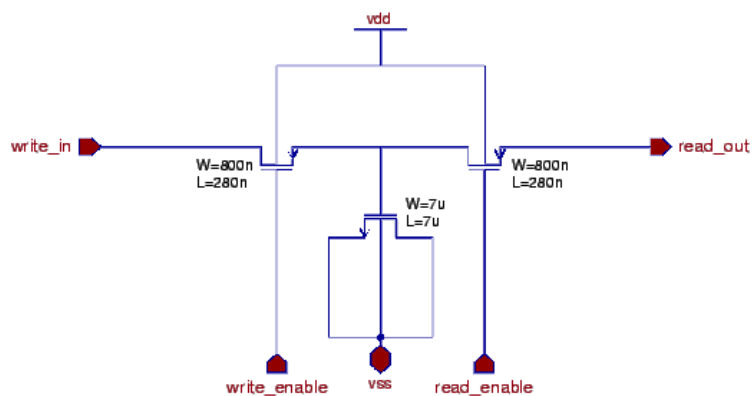**Figure 3.13:** Circuit of the APV25 preamplifier [44].

Figure 3.14: Scheme of the APV25 pipeline cell (right) circuitry [44].
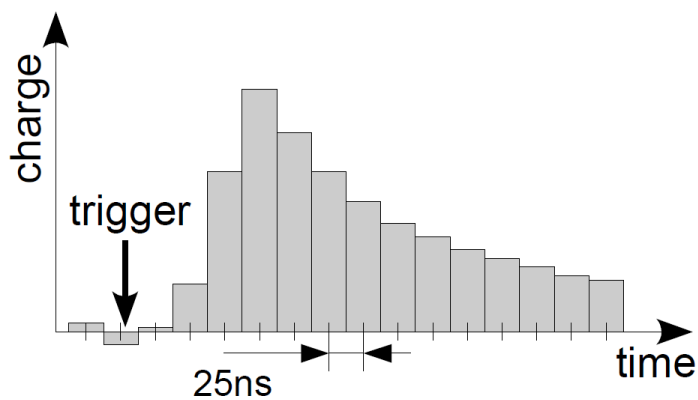

Figure 3.15: Schema of the APV25 sampling process, to record the signal evolution with time.
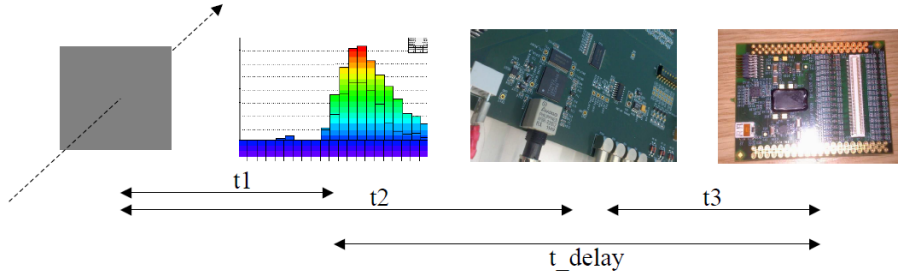
Figure 3.16: Trigger timing for the APV25 frontend electronics. t_1 is the time interval between a particle passing the detector and the analog signal being stored in the APV25 pipeline memory. In the LHC case, this time also includes the particle time of flight in between bunch collision and detector. t_2 accounts for the time of the trigger signal latency and trigger propagation time to the readout electronics. t_3 is the additional time needed to propagate the trigger from the readout electronics to the frontend chip. To read the correct data, matching the trigger event, t_{delay} must be chosen accordingly, to compensate for the different constant shares of the propagation time.

tion diodes and resistors is added to each of the APV25 channels to prevent irreversible damage to the chip caused by these very large charge signals.

3. APV25 hybrid boards are designed as either master or slave. Each HDMI cable is connected to a master hybrid, that connects to an optional slave via flat cable[6]. Only master boards house an Micro-HDMI header. Master and slave use separate lines of the HDMI cable for data transmission, so they are read in parallel.

4. The APV25 master hybrid boards also feature a PLL25 [45] chip that is responsible for trigger propagation to the APV25, but also for clock jitter reduction and fine-tuning of the clock phase to accommodate for propagation delays in cables. Slave boards share clock phase and trigger with the masters.

5. Low impedance connection to the chamber ground plane is necessary for effective discharge protection of the APV25 input circuitry. Therefore the hybrid board offers footprints to be equipped with low-impedance and low-resistivity SMA plugs[7], mating with the corresponding counterparts on the detector board.

The APV25 allows to read these consecutive sample data in multiples of three time bins, up to a maximum of 30. This feature can be used to reconstruct the charge signal shape and timing of gaseous detectors, like the exact determination of the start of the signal by means of fitting a Fermi function to the 25 ns spaced samples of the signal rising edge.

The readout of multiple time bins from the APV chip defines the maximum event rate that can be read out. When the chip is clocked with 40 MHz and each time bin needs 140 clock cycles to be sent out on the analog line (128 channels plus overhead) the maximum trigger frequency equals 285.7 kHz / $N_{timebins}$.

3.3.2   Front End Concentrator Card FEC and Digitizer Card ADC

A Front End Concentrator (FEC) card is accompanied by a frontend-specific adapter card to receive data from the frontend chips. In case of the APV25 chips, an Analog to Digital Converter (ADC) card is used. The ADC card matches the FEC card via three PCIe type edge connectors, see figure 3.18.

---

[6]Samtec FTSH-180 header and FFSD-08 cable
[7]Samtec MMCX-P-P-H-ST and MMCX-J-P-H-ST, lacking the central signal pin to save cost

Figure 3.17: Photo of an APV25 hybrid board, with Panasonic and Micro-HDMI connector. The APV25 chip itself is covered by black epoxy to protect the thin bond wires. Also visible are the 1.25 V and 2.5 V voltage regulators and protection diode networks.

The ADC card houses eight HDMI connectors to connect one APV25 master frontend hybrid each, supporting up to 2048 input channels with eight master and eight slave units. Two octal 40 MHz ADC chips[8] perform analog-to-digital conversion at a rate of 40 MHz.

The FEC card FPGA[9] connects not only to the ADC card, but also to several front panel headers. These include two LEMO 00 type connectors for NIM signals, one LEMO 0B connector for LVDS signals, two RJ45 headers, as well as an SFP cage which allows to connect to an ethernet network via fiber or copper cable.

Several different FEC card FPGA firmware versions are currently available to read data from APV25 chips.

Raw data FEC card firmware

In this firmware variant, data from all APVs connected to the ADC card and selected via a mask register are sent from the FEC FPGA to the data acquisition system. Additional data formatting steps include the addition of header and trailer words to the raw digitized samples from the APV25 chips. It is up to the user to extract the useful data from this stream. For an overview of the data format, see the official APV25 user guide [46].

Two sub-variants exist, depending on the upstream data acquisition system.

1. An Ethernet variant of the raw data firmware uses the FEC cards SPF plug to connect to an ethernet network. Data from each APV for a given trigger is sent via an individual UDP packet to a data acquisition PC. Several FEC cards can share a PC by using commercial network switch devices. To allow the readout of multiple time bins, all network equipment must support Ethernet jumbo frames of up to a size of 9 kbytes.

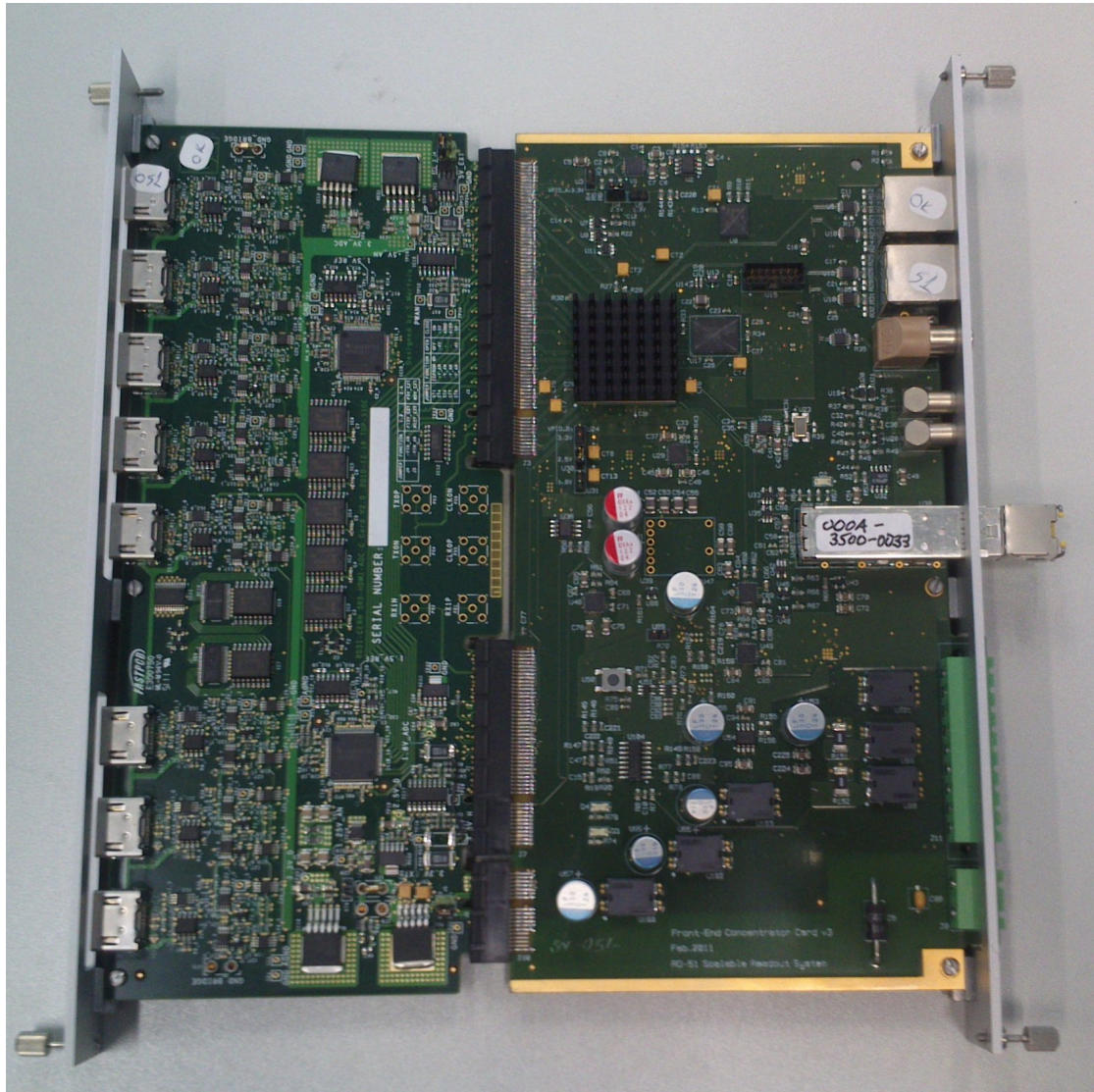[8]TI-ADC5281
[9]Xilinx Virtex5, XCV5LX50

Figure 3.18: ADC and FEC card with the Virtex-5 FPGA beneath the black heat sink. Also visible are the HDMI sockets, ADC5281 analog-to-digital converters (square chips on the left board) and SPF cage with transceiver for ethernet cable.

2. If a SRU unit is used (See chapter 3.3.3) to collect data from several FEC cards and to make use of its additional hardware and connectivity, communication in between FEC card(s) and SRU is realized with DTCC Links [47] (See chapter 3.4.5), using commercial CAT7 network cable.

The data size of an event using this firmware variant, is heavily dominated by the digitized samples for each strip and time bin. Two bytes of data transmission and storage are needed for each time bin for each of 128 channels for each of the connected APV25 chips, e.g. 73 kbytes per event for a complete FEC card with 16 APV25 chips at 18 time bins each. For the Ethernet variant, the trigger rate is therefore limited by the GBit/s bandwidth to ∼1.2 kHz, including protocol overhead.

Zero suppression FEC card firmware

If either the trigger rate on an SRS system or the channel count increases to a value, where the resulting data rate exceeds the bandwidth limitation of the networking equipment used, either the detector channels must be split to several FEC cards and PCs, or the event size needs to be reduced. Since in the application of a fine-pitch readout like the Micromegas detectors the occupancy of the channels is usually low, large fractions of the event data are just baseline values. To benefit from this fact and save bandwidth, a zero-suppressing FEC card firmware variant[10] has been developed, processing the event data and sending out only those channels, that had a signal above a certain and adjustable threshold value.

The zero-suppressing firmware again exists in the two sub-variants, supporting either direct connection via ethernet, or the DTCC link protocol to connect to an SRU unit. The latter has been chosen to be used with the Read Out Driver firmware, due to the high trigger rate in ATLAS and the necessity of an SRU unit.

3.3.3 Scalable Readout Unit SRU

The Scalable Readout Unit (SRU) is a board matching a 19 inch 1HE form factor case, housing a large and powerful Virtex-6[11] FPGA and a variety of additional components and connectivity options. These include:

1. A SO-DIMM slot for up to 4 GB DDR3 memory.

2. 4 SFP+ cages, one of them connected to a 10 GBit/s PHY chip, allowing 10 GBit/s ethernet connectivity

3. Optical fiber plug, connected to a TTCrx [48] chip, which is the default ASIC to receive Trigger and Timing and Control information within the LHC TTC distribution network.

4. 40 RJ45 plugs, connected to the FPGA via LVDS transceivers, for a total of 160 high-speed differential line pairs.

5. 8 LEMO 00 type connectors for NIM signals, 4 LEMO 0B connectors for LVDS signals.

The SRU needs to be powered from the external voltages 1.8 V, 3.3 V, 4.2 V and -12 V which are available for example from the ATX adapter board already mentioned for the FEC card power supply. All other necessary Voltages are generated on the SRU by means of linear regulators.

---

[10]Development of Raffaele Giordano, INFN Napoli
[11]Xilinx XCV6LX130

3.4   SRU as ATLAS Read Out Driver for Micromegas

The New Small Wheel upgrade for the ATLAS muon system will be installed during the Long Shutdown 2 (LS2) in 2018 and 2019. As mentioned, the previous shutdown period LS1 yields the opportunity to install a pre-series Micromegas chamber in advance of the NSW commissioning. This not only allows to develop and test simulation and reconstruction algorithms well in advance the NSW operation, but also to test and optimize design and operational parameters of the NSW Micromegas chambers. Therefore it is necessary, to fully integrate the prototype chamber into the ATLAS data acquisition chain, to be able to compare its measurements with the ATLAS data on an event-by-event basis.

This integration will be managed with the custom designed Micromegas Read Out Driver (ROD) described here, based on the Scalable Readout System (SRS). An interface from the Micromegas specific domain into the common ATLAS domain has been realized as FPGA firmware for the Scalable Readout Unit (SRU). The SRU therefore needs to interface to the following different systems.

1. Like the other ATLAS subsystems, the Micromegas SRU Read Out Driver uses the TTCrx chip, together with an optical receiver for L1 trigger signal reception from the ATLAS central trigger processor. It also recovers the LHC bunch crossing clock from the optical signal for a synchronous detector operation and allows a coarse and fine tuning of the clock and trigger signals, to compensate for different signal propagation time. The TTC network also transmits the bunch counter reset signal BCR that indicates a complete orbit of the LHC bunch train and the event counter reset ECR for a synchronous reset of the ATLAS wide event counter in all subsystems. Additional signal lines allow the broadcast or directed transmission of user data from the CTP to the system that house the TTCrx chip.

2. The FEC cards of the SRS system are connected to the SRU via DTCC [47] links. These are used to synchronize with the LHC clock and the transmission of triggers and configuration data in the one direction, and the reception of detector and configuration data in the other.

3. ATLAS event data sent from the RODs upstream to the ROS PCs are formatted using the SLINK protocol over optical fiber as carrier medium. Therefore the Micromegas ROD formats the event data the same way and uses SLINK over optical fiber as link to the ATLAS data acquisition infrastructure as well.

4. An additional connection to the ROD is necessary for configuration and monitoring. ATLAS ROD therefore normally use registers accessible via the VME backplane of the ROD crate, together with a single-board PC as VME Controller. The SRS does not support VME connectivity due to its outdated nature. The Micromegas ROD therefore utilizes a gigabit ethernet connection for this purpose.

In addition, the SRU needs to handle all trigger propagation and event building logic, to maintain synchronization with the other ATLAS subsystems. Each L1 trigger signal must result in a valid ATLAS ROD event fragment sent upstream to the ROS. For an overview of the main functionality blocks of the firmware see figure 3.19.

The latest ROD firmware design v.22 uses the SRU board revision 2, which differs in some points from a 0.3 version, making the firmware incompatible without modifications.[12]

The SRU firmware has been designed, synthesized and implemented using the Xilinx ISE design suite software, Version 14.4, logic edition.

---

[12]Only few modules of the version 0.3 board were shipped, mainly to SRS developers. The full SRU schematic is available on request from the RD51 Working Group 5 (electronics), together with all other SRS schematics and documentation. See the RD51 website http://rd51-public.web.cern.ch/rd51-public/ for more details.
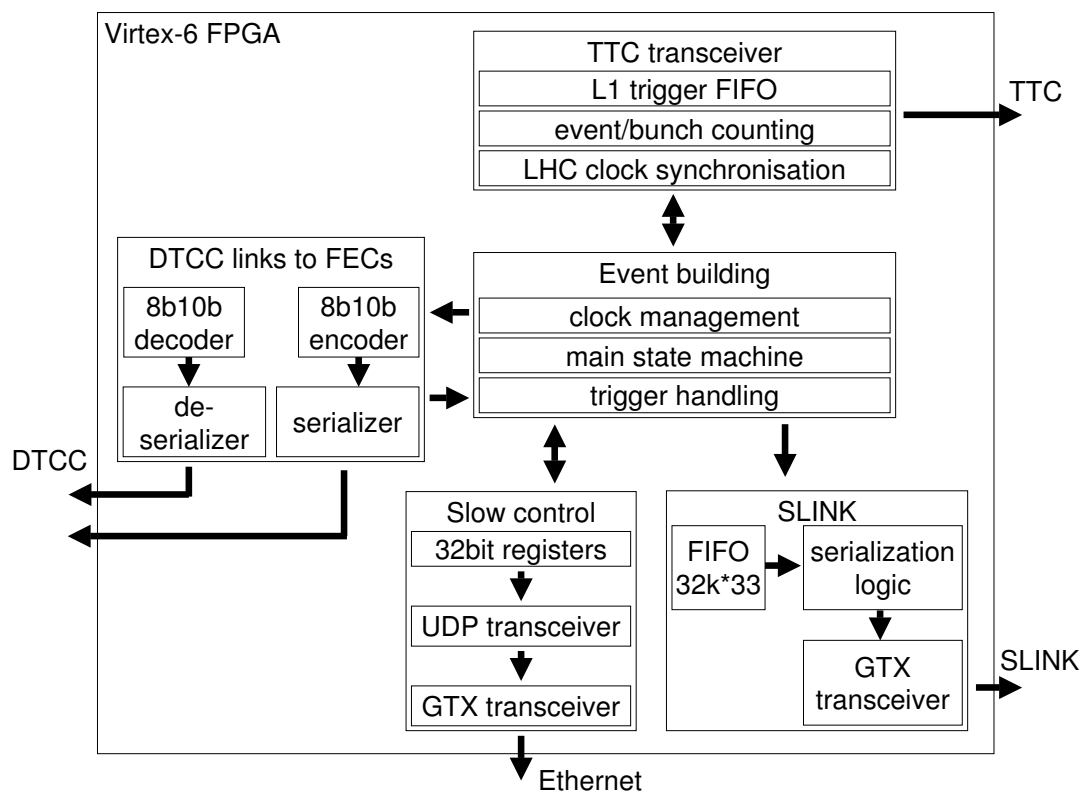
Figure 3.19: Simplified block diagram with the main tasks of the ROD Firmware of the SRU Virtex-6 FPGA [49].

3.4.1   Trigger handling and sources

The most important L1 trigger source of the Micromegas ROD is the TTC network, which is the one used during normal operation.

On the SRU board revision 2, in contrast to version 0.3, all important TTCrx pins are connected to FPGA pins, to make full use of its potential.

For test and debugging purposes, but also for standalone use without TTC network, the ROD firmware offers a variety of additional trigger sources. These are selectable via slow control register and consist of

1. none: disable trigger generation

2. one-time fixed number: a fixed amount of triggers is generated when selecting this source

3. fixed rate: triggers are generated at a selectable rate

4. external NIM: one of the SRU LEMO input plugs is used as trigger source

5. external TTC: triggers sent from the TTCrx chip are used

As triggers may occur faster than they can be processed, all triggers received by either trigger source are stored within a 4k deep L1 trigger FIFO pipeline and processed one after each other. As long as this buffer does not flow over, all triggers are guaranteed to be processed in either way, assuring a continuous sequence of events being sent upstream to the ROS. The occurrence of such an overflow will be monitored.

The SRU features an onboard 200 MHz oscillator, from which 40 MHz and 80 MHz are derived, using the Virtex-6 internal clocking resources. The 80 MHz are used as main clock for the event building functionalities, 40 MHz drive the data feed to the SLINK.

The TTCrx introduces the LHC bunch-crossing clock to the system, which is not synchronous to the onboard clocks. The nominal LHC clock is 40.08 MHz, with small deviations during the LHC ramp up. Therefore FIFO memories are used consequently to transport data in between the different unsynchronized clock domains.

The SLINK and Ethernet design blocks each use additional FIFO memories to be able to use the asynchronous 125 MHz reference clocks from the SFP+ transceivers for their serialized data streams.

3.4.2   Event building and busy logic

The Micromegas ROD firmware includes the following processes, running independent from each other, partly within different clock domains.

1. When a trigger arrives from the selected trigger source, a trigger decider module checks whether the event building process is currently busy or not.

   In the case of no busy signal, the trigger is propagated to the FEC cards, and an entry is put onto the L1 FIFO, containing additional information like event ID, bunch crossing ID, etc.

   When the event building process signals that the FEC cards are presently being read out and not ready to receive a new trigger, an entry is put onto the FIFO memory, containing a flag that marks this event as busy. For details on this behavior, see chapter 3.4.3.

2. The event building module checks the presence of an entry in the L1 FIFO. If at least one is available, the module begins with generating ATLAS event header information, including the event ID, etc. These words are written to another FIFO buffer for SLINK transmission, which is 32k words deep.

In case of a busy event without detector data to be expected from the FEC cards, the header words are immediately followed by trailer words, indicating that the event contains no usable detector data. Nevertheless, the event fulfills all requirements on an ATLAS ROD event fragment, to maintain overall consistency with the other systems despite the unavailability of APV25 data.

For each of the valid events that are not marked busy, the event building process waits for the data to arrive from the FEC via DTCC input buffers. Those data are then included into the ROD fragment which is marked as valid in the trailer. A time-out mechanism prevents the hang-up of the system in case of an interrupted transmission.

3. The SLINK FIFO is permanently being monitored and eventually read out with a rate of 40 MHz, feeding the data words to the SLINK transmission core. Buffer reading is interrupted in case of SLINK unavailability (link full or link down flags). Short SLINK unavailabilities during running data acquisition can by this method be compensated, until the SLINK buffer runs full, which will be again monitored.

The data format of an ATLAS ROD event fragment is shown in figure 3.20
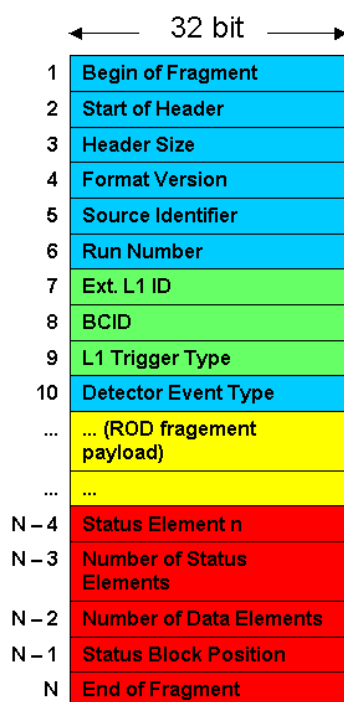
Figure 3.20: Structure of an ATLAS ROD event fragment [41]. The event header contains information about the origin of this fragment (blue) and trigger information (green). The event payload (yellow) contains the actual detector data matching the L1 trigger. The event fragment is concluded by several trailer words (red), containing status information about the event, like the occurrence of errors or loss of data.

3.4.3 Implications from the use of APV25 chips and from forming a stand-alone ATLAS DAQ partition

The APV25 chips were designed to be used in the CMS silicon strip detector, and thus to be read out at a rate comparable to the ATLAS L1 trigger rate. However it was not foreseen to read a large number of time bins from the chip at these rates, as it is necessary for the application of the μ-TPC

track reconstruction mode. As mentioned in chapter 3.3.1, the maximum trigger rate is defined as 285.7 kHz / $N_{timebins}$, or roughly 10.5 kHz at 27 time bins event width.

Since this is significantly lower than the maximum ATLAS L1 trigger rate of 100 kHz, not every trigger can be served by the Micromegas ROD. Even when accepting the low event yield of $\sim$10%, the ATLAS DAQ system does not allow missing events, and will drop out any subsystem that sends non-consecutive events above a certain threshold.

To nevertheless allow an operation within the ATLAS data acquisition, a bookkeeping-logic has been implemented within the ROD firmware. This system decides for each L1 trigger, whether it will be propagated to the APV25 chips or not, based on whether the preceding event has been processed completely (event building available) or not (event building busy).

As already mentioned in chapter 3.4.1, each of the events not selected for APV readout is nevertheless stored in the trigger FIFO memory, to generate a full valid ATLAS event fragment, without any detector data within the payload.

The Micromegas ROD has first been used within the ATLAS DAQ system during the last four months of proton-proton collisions before the beginning of the Long Shutdown 1 (LS1), from September 2012 to January 2013, for details see chapter 3.5.1.

To minimize the risk for the whole ATLAS data taking procedure, it has been decided to not fully integrate the prototype Micromegas ROD into the ATLAS system during a running data taking period. Nevertheless the SRU has been installed in a passive way, only receiving ATLAS L1 triggers, and writing the detector data to a standalone DAQ partition, independent from the ATLAS operation. In this way it was impossible to interfere negatively with the ATLAS DAQ partition, but also no Level 2 trigger information were available, as these are only propagated to ROS PCs that are part of the ATLAS DAQ partition.

This unavailability of L2 information caused a bandwidth limitation on the ROBIN card, that now could not delete 97% of the L1 events as usual, but needed to transfer all events from its input buffers to the ROS PC and to disk.

At the nominal ATLAS L1 trigger rates this caused an overflow of the ROBIN buffers, and thus the assertion of the Link Down (LD) signal upstream to the Micromegas ROD. As event building and the generation of events continued, the SLINK FIFO on the SRU immediately suffered from overflow and data words were lost, corrupting the integrity of the data stream.

To compensate for this additional limitation, caused by the incomplete integration into the ATLAS systems, an additional data rate control mechanism has been included, called safe mode. Upon activation of this mode, for each trigger the fill state of the SLINK FIFO is checked. In case of a fill state above a certain threshold, indicating a SLINK congestion, the event is not processed at all, resulting in a loss of data and continuity, but nevertheless this happens in a controlled fashion. The threshold is selected such, that a full event data will fit in the remaining FIFO space in case of an accepted event. The ROS checks for missing event IDs in the event headers, so in safe mode, the SRU firmware fakes this number to ensure a continuous stream of events despite possible ignored triggers in between.

This data stream satisfies the standalone DAQ partition, but events are no longer comparable with the other ATLAS subsystems by means of the event ID. This is why the original and ATLAS-wide valid event ID is also contained within the events payload, for offline analysis and comparison. It must be noted, that the yield of coincident stored events from the standalone DAQ partition and the events finally selected by the ATLAS event filter is very low due to that independent dilution.

Tests with a certain ROS configuration are suggesting a maximum event rate to be read from the ROBIN card of 20 kHz. This 1/5 yield of L1 events, together with the maximum ATLAS event filter rate of 200 Hz results in a coincidence rate of 40 Hz. Together with the above mentioned factor of $\sim$1/10 due to APV25 limitations, the final event rate available for comparison in between

Micromegas and ATLAS data is around 4 Hz, not including the geometric probability for a muon hit in the prototype Micromegas detector.

3.4.4 Connectivity to SLINK destinations (ROS)

The SLINK protocol is exclusively used within ATLAS for data transmission to ROBIN cards, using optical fiber with 2.0 GBit/s transmission speed as physical layer. Most of the systems use a separate HOLA [50] card, see figure 3.21, for SLINK transmission.
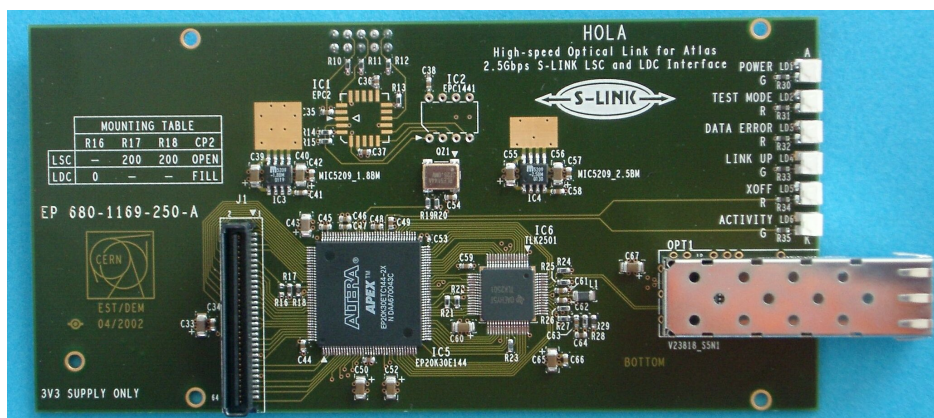

Figure 3.21: HOLA daughter card that offers SLINK connectivity for a large number of ATLAS ROD systems. The signals defined by the SLINK protocol are read from the header and transmitted over optical fiber, using the onboard FPGA and serializer chip (Texas Instruments TLK2501). In the Micromegas ROD the complete HOLA functionality is included within the SRU FPGA, using one of its internal high-speed serializers and an additional optical SFP+ plug [50].

Most of the ATLAS DAQ electronics has been designed in the late 90's, and modern FPGAs offer a heavily increased amount of resources and processing capabilities. This is why the complete HOLA card logic functionality has been redesigned [51] as IP core and in this project integrated into the SRU Virtex-6 FPGA. The signal interface of the IP core is identical to the hardware pins available on the HOLA board and according to the SLINK specifications. The TLK2501 serializer chip is substituted with one of the FPGA internal GTX transceivers and one of the SRU onboard SPF cages is used together with an optical SPF transceiver for signal conversion to optical fiber.

3.4.5 DTCC Link capabilities

The data transmission in between SRU and FEC cards is realized as Data, Trigger, Control and Clock (DTCC) link [47]. The SRU hardware offers up to 40 RJ45 plugs, whereas the DTCC link has up to now been successfully tested on a SRU board with 8 FEC cards in total.
In the Micromegas ROD implementation, the DTCC links are used to transmit the following information in the two directions:

1. Configuration data and commands from the SRU to the FEC cards and APV25 chips, as well as trigger information.

2. Detector data and FEC configuration data from the FEC to the SRU.

The DTCC link IP core uses clock multiplication from the connected 40 MHz input clock, so data transmission is again based on FIFO memories to divide the different clock domains.

3.4.6 Ethernet connectivity

The SRS slow control and configuration is based on the transmission of UDP packets. Each SRS component, like FEC and SRU, uses its own IPv4 address within the network. Therefore both make use of an SPF transceiver and FPGA internal ethernet resources and IP cores to provide the UDP connectivity[13].

Different services on a single SRS device use then different UDP ports for identification, each offering a number of registers for either read-only or read-write access. Additional sub addresses are available for further refinement. Figure 3.22 shows the structure of a SRS slow control request and reply packet, used either for a read or write access to a single register or several registers.
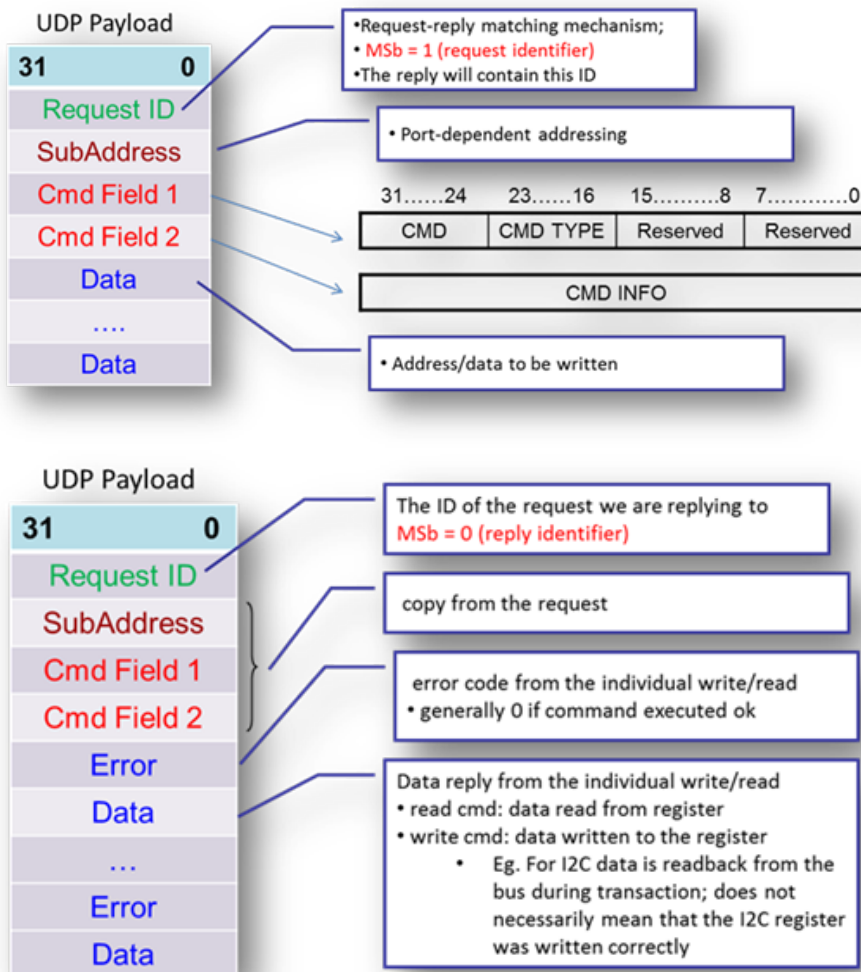
Figure 3.22: Format of the SRS slow control request and reply UDP packets [52]

In case several FEC cards are connected via DTCC links to a SRU and a slow control PC connected via ethernet to the SRU, the SRU acts as an ethernet switch, being transparent for packet exchange in between the PC and the FEC.

To control the Micromegas ROD in a convenient way, including the configuration of SRU, FEC cards

---

[13]the implementation of the SRU firmware ethernet connectivity and slow control has kindly been contributed by Sorin Martoiu, INFN Bucharest

and APV25 chips, a C++ application has been developed, that make use of system calls to the netcat[14] tool to send and receive UDP packets.

3.5 Test of the Firmware

3.5.1 Test within the ATLAS infrastructure

In early 2012, two small Micromegas prototype detectors have been installed within the ATLAS detector - one attached to a Small Wheel CSC chamber and one in the minimum bias trigger scintillator (MBTS) area, next to the liquid argon calorimeter system.

These detectors have been operated successfully in a stand alone mode, using random triggers to record particle tracks, and also to study the proportionality of the high voltage channels current with the LHC luminosity. For details on these detectors and the measurements, see [53].
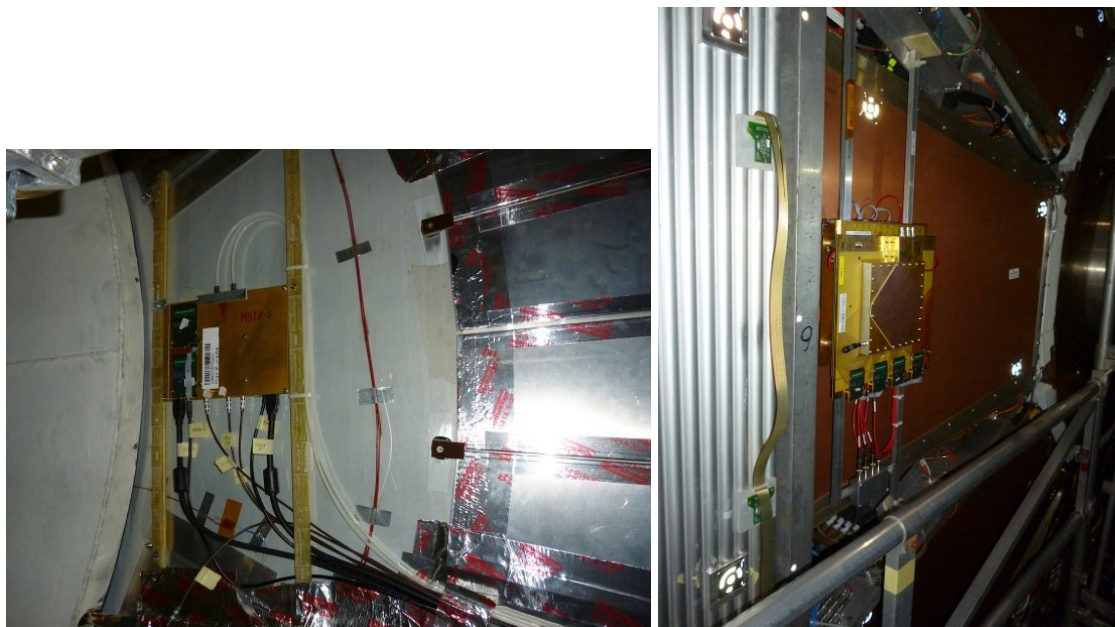

Figure 3.23: Photos of the Micromegas detectors installed within ATLAS in the MBTS region (left) and the current small wheel (right) [53].

The FEC card used to read the detectors via APV25 chips was installed in an electronics rack very close to the ATLAS detector, using 30m HDMI cables to connect to the APV hybrid boards. During a technical stop in September 2012, a SRU unit was installed additionally at the same place, to allow triggering and readout via the ATLAS data acquisition system, using the Micromegas ROD firmware. The ATLAS detector is located within the UX15 cavern, whereas the data acquisition systems are housed in the neighboring cavern USA15, mostly protected from magnetic fields and radiation, see figure 3.24

Figure 3.25 shows the schematic connection between the different components of the ATLAS compatible Micromegas readout structure. Data transmission in between the UX15 and USA15 caverns are realized by optical fiber for

1. SLINK event data transmission from the SRU to the Micromegas ROS PC.

---

[14]Netcat is part of most linux distributions. See the official website http://netcat.sourceforge.net/
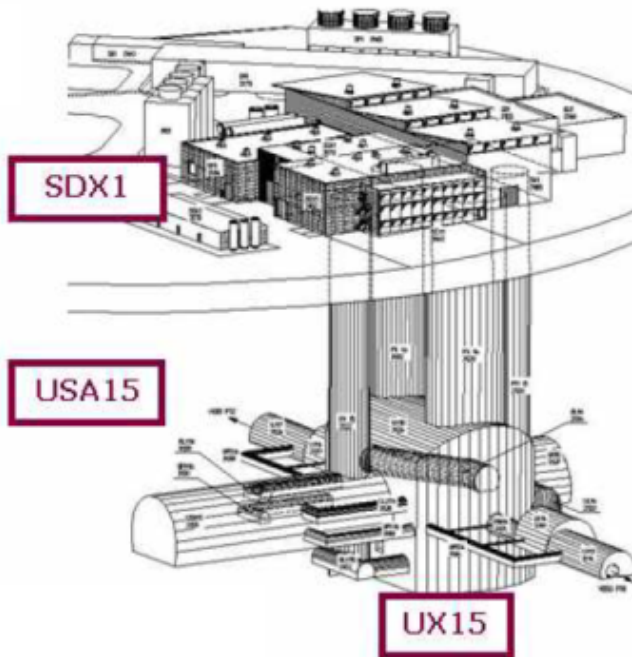
Figure 3.24: Buildings and structures related to the ATLAS Experiment: the surface installation SDX1, electronics cavern USA15 and detector cavern UX15 [54].

2. LHC clock and ATLAS L1 trigger propagation from the Central Trigger Processor (CTP) in USA15 to the SRU. To be more precise, one of the spare optical outputs of the Cathode Strip Chamber (CSC) TTC crate was connected to the SRU, so the Micromegas ROD received the same triggers as the CSC chambers.

3. GBit/s ethernet via optical fiber to the slow control PC.
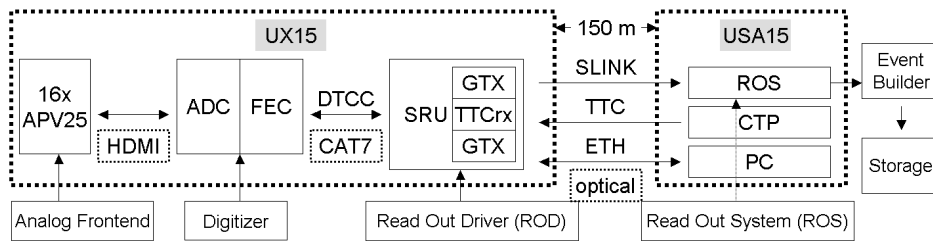
Figure 3.25: Schema of the SRS interconnections and the integration into the ATLAS DAQ infrastructure. The SRU was located in the detector cavern, connected to the ATLAS components via optical fibers.

During ATLAS operation, several runs have been taken with the Micromegas stand alone partition, taking into account the limitations mentioned in chapter 3.4.3. Unfortunately, a severe error in the FEC card zero suppression firmware was found only after the end of the technical stop, which could only be fixed during a later technical stop. This error rendered the charge information read by the APV25 chips completely useless, but nevertheless allowed to test the event building procedure, which was found to be working correctly and according to previous tests in a test bench environment.

Figure 3.26 shows the distribution of the Bunch Crossing IDs (BCID) belonging to triggers during ATLAS run number 214494 on November 13th 2012, measured with the Micromegas ROD. The

bunch train structure of the LHC is clearly visible, together with the fact that in 2012 the LHC was running with a bunch spacing of 50 ns, leaving every second bunch unoccupied and thus unable to generate triggers. This indicated, that the TTC connection and interpretation as well as the SLINK connectivity do work as expected.
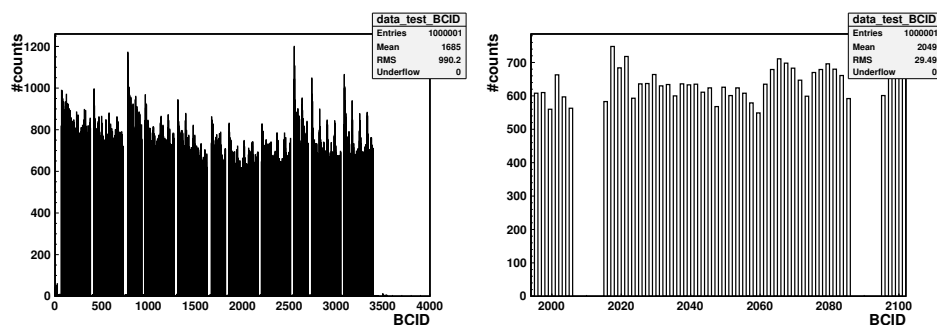

Figure 3.26: Bunch crossing IDs matching the ATLAS L1 triggers during a portion of ATLAS run 214494, collected with the SRU ROD firmware. The structure represents the bunch structure of the LHC with gaps due to the injection and extraction scheme. A close-up (right) reveals the bunch spacing of 50 ns in 2012, leaving every second bunch empty and thus creating no trigger.

A refined version of the zero suppressing FEC card firmware was received in January 2013 and programmed into the FEC card during the winter shutdown, but unfortunately no reliable DTCC link connectivity could be established in the remaining days of heavy ion collision operation before the LHC shutdown on February 14th 2013.

Nevertheless the development on the SRU firmware continued, and is planned to be in full operation within ATLAS in 2014, as described in chapter 4.1.

3.5.2 The L1 chamber at the LMU Cosmic Ray Test Stand

Another test of the Micromegas ROD firmware for the SRU has been performed within the LMU Munich Cosmic Ray Facility (CRF), located in Garching.

The CRF features two 2.2 x 4.0 m^2 sized ATLAS barrel MDT chambers as reference detectors for the track reconstruction of cosmic muons. The unoccupied space in between allows the installation of a detector under test for track measurement comparison. This installation has originally been used to measure the construction precision and wire position of a fraction of the barrel MDT chambers that have later been installed in ATLAS.

During 2013, a ~1m^2 sized Micromegas chamber has been installed at the CRF, to measure spatial resolution, efficiency and μ-TPC performance at high statistics [55].

Since the CRF makes broad use of ATLAS data acquisition electronics, it was at the same time used as a test bench for the Micromegas ROD. 16 APV25 chips were read out via a single FEC card, connected to an SRU board. The SRU has been triggered together with the MDT electronics via TTC VME modules. Data were read out via a dedicated ROBIN card, and later merged with the MDT data via the L1 event number, resulting in a readout scenario very close to the operation within ATLAS, from an electronics point of view. The Read out Driver performed without errors for a total of more than 200 million triggers.

Figure 3.28 shows the measured difference in between MDT and Micromegas measurement along the precision coordinate as one of the results. The shape of the distribution indicates a rotation of the L1 chamber in the horizontal plane with respect to the MDT coordinate system. In addition, a jump in the distribution is visible exactly in the middle of the chamber as a result of the imperfect alignment of the two readout boards that form the active area of the detector.

Figure 3.27: The LMU Cosmic Ray Facility, located in Garching. Two 2.2 x 4.0 m^2 sized ATLAS MDT chambers measure cosmic muon tracks as reference for a detector under test. The L1 Micromegas chamber is located in between, together with additional trigger scintillators.

The measurements also indicate, that the former problems with charge measurement corruption due to an error in the zero suppression core of the FEC card firmware were successfully solved.
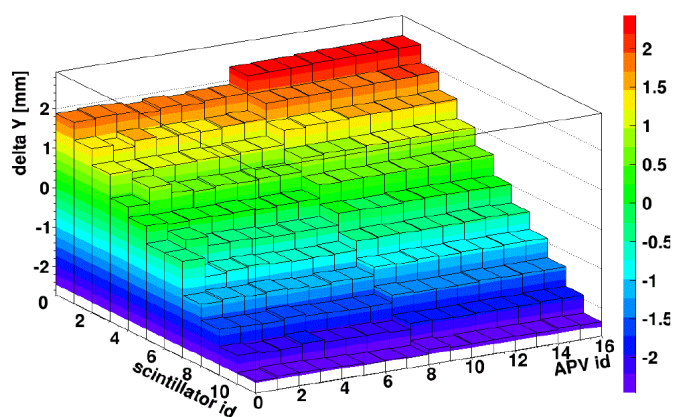
Figure 3.28: Measured discrepancy in between MDT track prediction and L1 Micromegas chamber measurement in the precision coordinate, measured within the LMU Cosmic Ray Facility (CRF). The slope of the distribution is the result of a rotation of the Micromegas detector in the horizontal plane. The additional jump in between APV numbers 7 and 8 results from the imperfect alignment of the two readout panels that were merged to form the 1 m^2 sized readout structure of the detector. [55].

Chapter 4

Summary and Outlook

4.1   Status and future plans for the ATLAS Micromegas ROD

The presented ATLAS compatible Read Out Driver, based on the Scalable Readout System, fulfills all important requirements to be integrated into the ATLAS data acquisition chain. Tests of the system were performed within the LMU Cosmic Ray Facility, as well as within the ATLAS detector cavern and several small sized setups to study and improve the performance of the system.

Any detector equipped with up to four FEC cards or 64 APV25 hybrid boards can be read out with the system, including zero suppression on the FEC card level for an optimized counting rate.

Micromegas detectors will be one of the technologies to be installed in the ATLAS New Small Wheels during the Long Shutdown 2 of the LHC accelerator in 2018/19.

The presently ongoing Long Shutdown 1 offers the opportunity to install already now a pre-series Micromegas chamber within its designated environment, attached to one of the present small wheels. The operation of this detector during the run period from 2015 to 2017 will give important information and hints for the construction and operation of the NSW detectors, but also allow early tests of the integration of Micromegas into the simulation and reconstruction framework of ATLAS.

This prototype detector will consist of four detection layers with 1024 strips each, and a total size of 1.20 m x 0.60 m.

The VMM2 chip is expected to arrive from the factory in time for installation together with the pre-series chamber, so it will be the first medium-sized physics application and test for the chip. Figure 4.1 shows the planned readout scheme for this chamber.
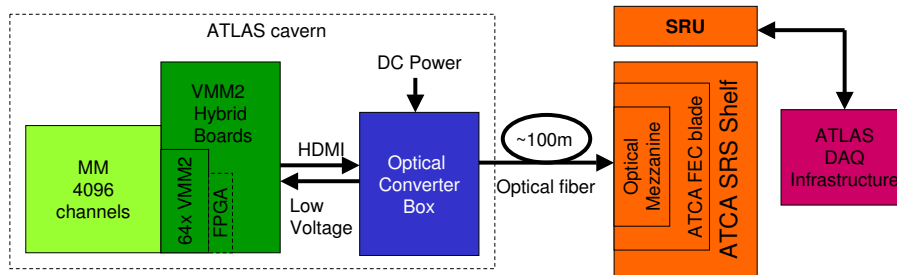

Figure 4.1: Readout scheme for the prototype chamber equipped with VMM2 chip hybrids. An additional intermediate optical converter box multiplexes the data from several VMM2 chips and converts the signal to optical fiber, fed to the SRS hardware in the neighboring cavern. The optical converter box also contains switched mode DC to DC converters for the VMM2 hybrid power supply.

The figure introduces several new components to the SRS system:

1. The VMM2 hybrid board contains, apart from a certain number of VMM2 chips, also a companion FPGA, that stores detector data temporarily, until a L1 trigger decision is received, and also handles communication in between the VMM2 chip and the following components. The FPGA is according to vendor descriptions insensitive to radiation damages, and will later in the NSW design be replaced by a dedicated digital ASIC chip.

2. An optical converter box is needed, to translate the slow control, trigger, clock and data streams from the HDMI cables in the ATLAS cavern onto optical fiber, reaching into the neighboring counting cavern. The box will also supply the necessary low voltages for the connected VMM2 hybrid boards via HDMI cable, by means of a magnetic field insensitive switched mode DC to DC converter modules.

3. As a step towards a higher integration density and flexibility, the FEC and ADC cards have been redesigned to meet the specifications of the ATCA[1] standard. Figure 4.2 shows a prototype of the FEC card, converted into the ATCA form factor, together with two ADC mezzanine cards. The ATCA FEC features improvements in FPGA resources, memory and number of connections for frontend chips, compared to the classical eurocrate FEC. A mezzanine card with optical connectors to be used with the optical converter box for the readout of VMM2 frontend chips is currently being designed.
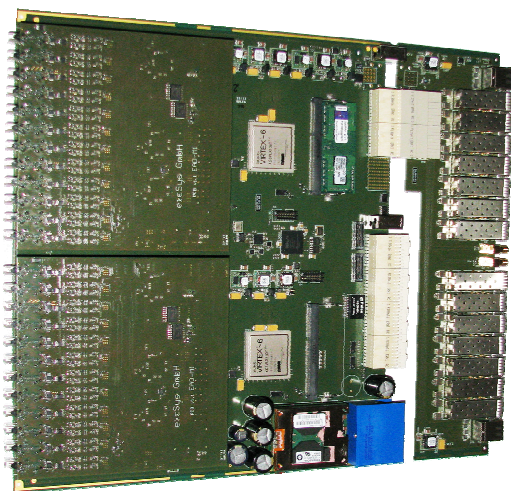

Figure 4.2: Picture of an ATCA FEC blade, together with two ADC mezzanine cards, for a total of 24 HDMI connectors, or 48 APV25 frontend chips.

Figure 4.3: Two ATCA FEC blades in a 3U ATCA shelf, together with a shelf controller.

4.2 Summary of the sMDT irradiation studies and outlook

The LMU tandem accelerator facility offers the possibility to generate particle irradiation scenarios that are comparable with the rate of background hits in LHC experiments, or even above that. This can be used, to test detector components and electronics at conditions very similar to their later field of application within high energy physics experiments like ATLAS.

sMDT detectors are based on the Monitored Drift Tube technology that are widely used within the ATLAS muon spectrometer. Due to their smaller diameter construction, these large-area detectors are applicable in high-rate environments.

A sMDT prototype detector made from 46 tubes has been tested under high rate irradiation with protons and a mixed field of neutrons and γ-particles.
At 200 kHz of proton irradiation rate, or $\sim$19 kHz/cm^2, the spatial resolution of the detector has been measured as (164.6 ± 3.1) μm, compared with a resolution of around 110 μm in the unirradiated case. Using the original 30 mm MDT tubes, this decrease of spatial resolution already occurs at around 10% of that irradiation rate.
Using a precisely defined irradiated tube area, together with a segmentation of the trigger scintillators, it was possible to distinguish in between the two main effects altering the tracking efficiency

---

[1]Advanced Telecommunications Computing Architecture, defined by the PCI Industrial Computer Manufacturers Group (PICMG), describes the mechanical and electrical specifications for electronics crates and boards

at irradiation: electronics dead time and space charge effects. Using a weighting model, these different contributions could be transferred to another measurement performed at the CERN Gamma Irradiation Facility in very good agreement.

The measurement of cosmic muon tracks under neutron and γ irradiation revealed a comparable spatial resolution, but a slightly lower tracking efficiency.
The very high analog signals created in the sMDT tubes due to nuclear recoils from the neutron irradiation flux content has been investigated for crosstalk effects. A strong correlation was found in between irradiation flux neutron content and the probability for electronic crosstalk from one channel on an ASD readout chip to another. This is in accordance with the high ADC value signals caused by the neutron recoil nuclei, and the ASD chip datasheet section for analog crosstalk.
Using the sMDT detector together with a BF_3 neutron counter allowed to determine, within certain errors, the neutron and γ composition of the irradiation flux, using different kinds of absorber material. The technique is only sensitive to neutron recoil signals, counting (n, γ) reactions as photons.

The measurement of the sMDT analog signal shapes by means of a fast flash-ADC could confirm the gain drop effects due to space charge at high rate proton irradiation. No abnormal signal shapes were observed during proton and neutron irradiation.

Although the ATLAS collaboration has decided against the use of sMDT technology in the New Small Wheel project in favor of the Micromegas technology, several sMDT chambers will be installed within the ATLAS detector. Due to structural constraints, several parts of the ATLAS muon spectrometer are only equipped with two layers of precision tracking devices, instead of three. This results in a reduced momentum resolution for muons, as only 2/3 of the track segments can be used to measure the track curvature.
These areas include elevator shafts to the inner parts of ATLAS, as well as the areas that are occupied by the massive structure where the detector sits atop.
Chambers with sizes of 1.2 x 2.2 m^2 have already been produced [56] and will be installed during the Long Shutdown 1 in the elevator shafts. Part of these chambers have also been tested and calibrated within the Garching Cosmic Ray Facility, see figure 4.4.
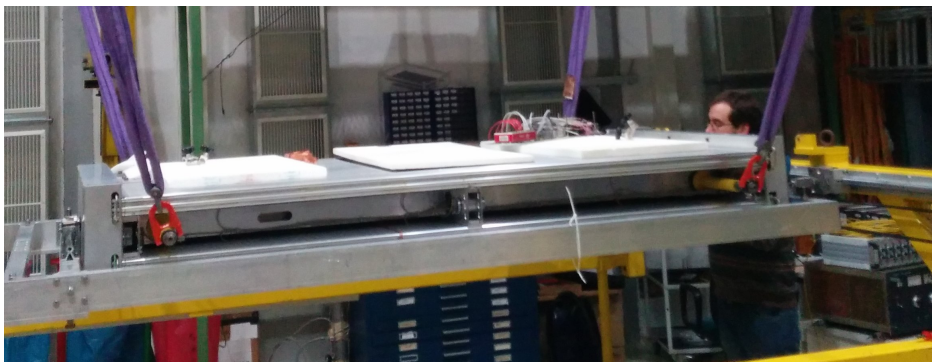

Figure 4.4: One of the sMDT elevator chambers, prior to the insertion into the Garching Cosmic Ray Facility for calibration and test measurements.

Appendix A

Appendix

A.1   Analysis methods for (s)MDT detectors

The analysis of sMDT data is based on the "mt-offline" program package[1]. This package was modified and adapted to the needs of this thesis.

A.1.1   T0-determination

To calculate the MDT drift radius from the drift time, two offsets of the measured drifttime have to be removed.

1. The LHC is a synchronous machine, and apart from (constant) time offsets, particles emerging the collision point arrive at each MDT chamber synchronous to the bunch crossing clock of 40.08 MHz. Trigger signals are also generated synchronously to this clock, and therefore drift time measurements start in intervals of 25 ns. As cosmic muons do not arrive in this regular fashion, drift time measurements are up to 25 ns too short, since measurements start with the next 40 MHz clock cycle only. This effect can be corrected by measuring the arrival time of this next clock cycle with respect to the cosmic muon trigger signal. This measurement is performed by an external Time to Digital Converter (TDC) module. Adding this time to each events measured drift time returns the correct value.

2. Due to propagation delays in cables and electronics, a constant offset is added to each time measurement. It can be removed by the determination of the beginning of the drift time spectrum using a fit function to describe its rising edge.
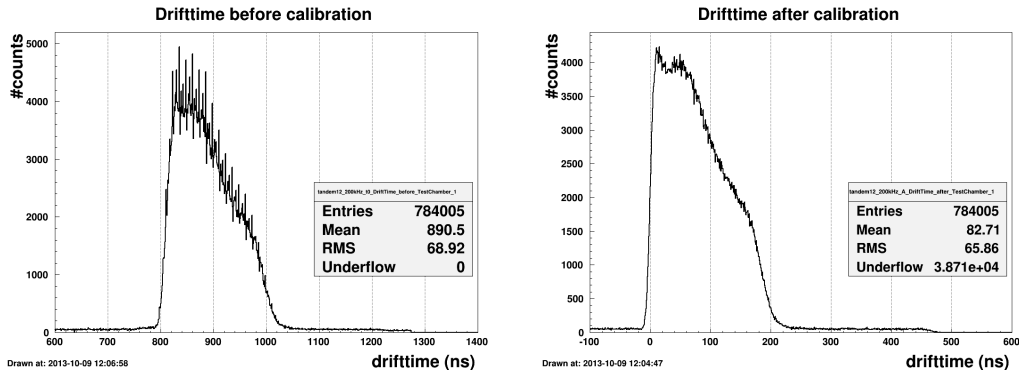

Figure A.1: Drift time spectra before (left) and after (right) calibration for offset and trigger jitter.

A.1.2   Rt-relations

Since the rt relation - the relation between measured drift time and determinable drift radius - is sensitive to a variety of environmental conditions, it must be determined for each measurement individually. This must be performed in an iterative process, since the rt relation is computed based on itself.

A first iteration of the rt relation can be obtained by integration of the drifttime spectrum. Each channel of the drift time spectrum represents $\frac{dN}{dt}$, which can be multiplied by $\frac{dr}{dr}$. The very first iteration uses the fact, that cosmic muons hit the tubes at random locations, so drift radii are equally distributed, and $\frac{dN}{dr}$ =const. In this way, the rt relation can be determined as $r(t) \propto \int_{t_{\min}}^{t_{\max}} \frac{dr}{dt}$. The boundaries $t_{\min}$ and $t_{\max}$ correspond to the rising slope and the end of the drift time spectrum.

---

[1]Originally developed by O.Kortner and F. Rauscher

This rt relation is then further iterated. A track fit through the whole chamber using the radii calculated with the previous rt relation iteration returns the distance between each hit tube wire and the fit as a new set of radii. The difference between the predicted radius and the track fit radius is defined as residuum $\Delta r = r_{\text{track}} - r_{\text{drift}}$, and its value is a good indicator for the quality of the track prediction. The residual distribution for the coarse rt-relation obtained by integration is shown in figure A.2 (left). It contains a systematic and radius depended variation from the ideal value zero for most radii. These values are now used, to modify the rt-relation in an iterative process, until they converge at a mean residual value for each radial section smaller than 30 μm, see figure A.3 and note the different scaling on the y-axis.

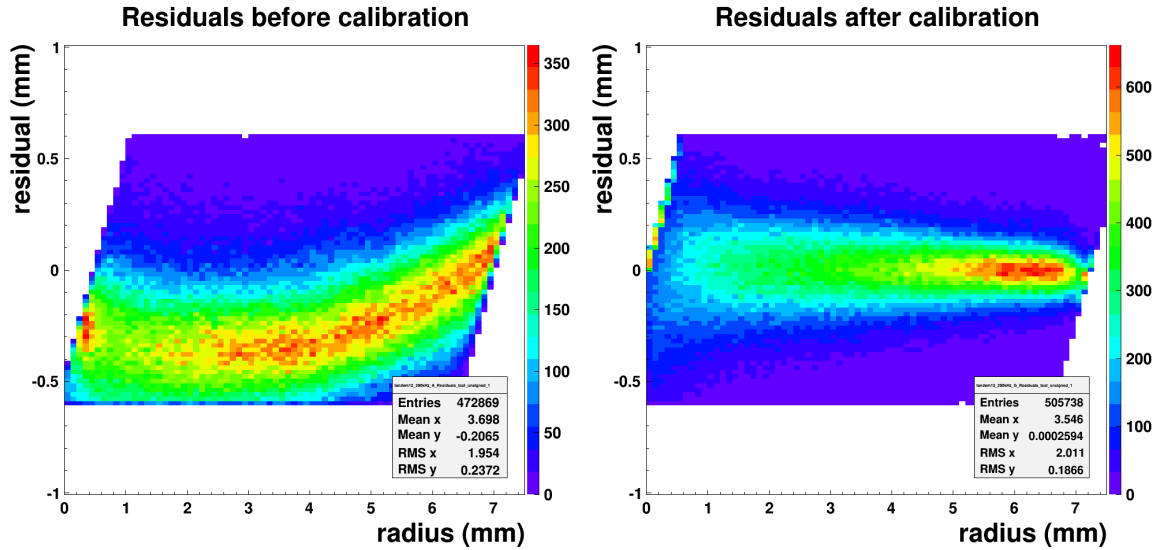**Figure A.2:** Residual distributions before (left) and after (right) calibration.
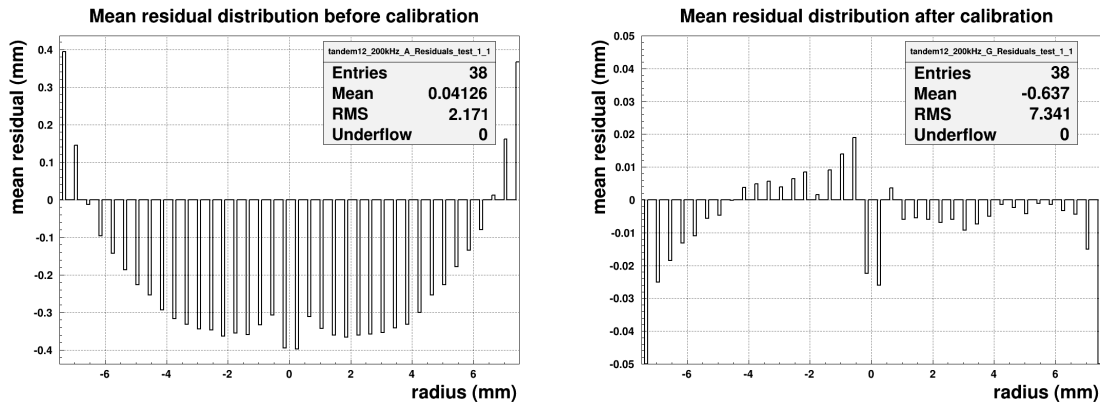
Figure A.3: Mean residual distributions before (left) and after (right) calibration. Note the different scaling on the vertical axis.

A.1.3   Spatial resolution

To determine the single tube spatial resolution of the sMDT chamber, tracks of cosmic muons are reconstructed, whereas a single tube layer is excluded from the track fit. In case of the proton irradiation of a single tube layer, this layer is the one to be excluded from the fit, to investigate the influence of the proton irradiation on the tube resolution, as shown in figure A.4.

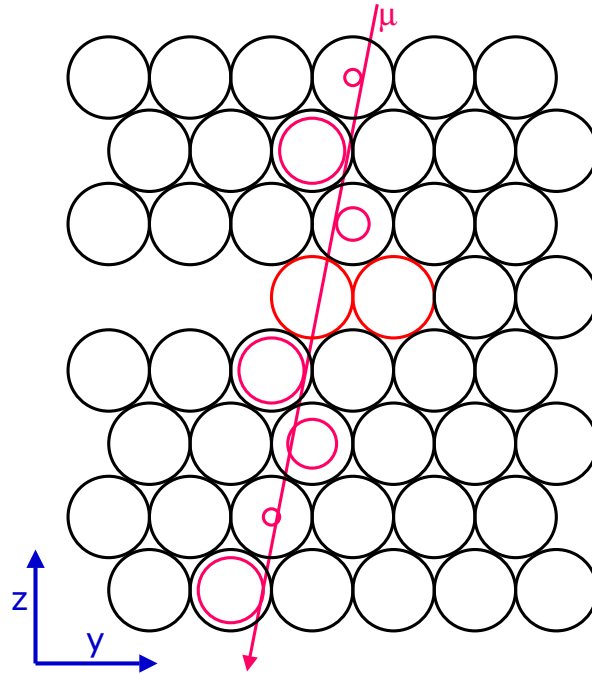**Figure A.4:** Schematic drawing of the principle for the determination of the spatial resolution. A straight track is fitted to radii measured in the reference layers, and its distance from the irradiated tube center is compared to its radius measurement.

The track fitting algorithm searches for a straight line, that fits the measured drift radii of all tubes that were hit and that passed several cut criteria. This removal of hits is necessary to filter out bad measurements or out-of-time hits, that do not belong to the cosmic muon track. The following cut criteria were used to determine the chambers spatial resolution and efficiency.

1. Each of the two trigger hodoscope layers is demanded to have exactly one hit in its three segments. Otherwise it can not be determined, whether the cosmic muon passed the irradiated tube section or not, as the trigger segmentation contains the only information about the x-coordinate along the tubes. Figure A.5 (left) shows the distribution of the number of scintillator hits on a logarithmic scale. The distribution is dominated by events with two scintillators being hit, but it also shows shower events that triggered up to all six scintillators.

2. The measured drift time with respect to the cosmic muon trigger needs to be within the window of zero to 200 ns. Hits outside this window are caused by other particles than the triggering cosmic muon. Nevertheless, hits with a drift time within this window do not necessarily result only from the muon track, but also from coincident particles, like δ-electrons.

3. As the detector uses seven layers for track fitting, events with hits in less than six or more than eleven tubes are sorted out to facilitate unambiguous track finding. The distribution of this number of hits can be taken from figure A.5 (right). The chosen boundaries contain the large majority of events.

4. The χ^2 value of the track fit is demanded to be lower than 10, to exclude reference track fits of poor quality due to mismeasurements in the reference tube layers.

Two example event displays for track reconstruction are shown in figure A.6. In the event shown in the left part of the figure, the track fit was successful, whereas in the event shown on the right, too
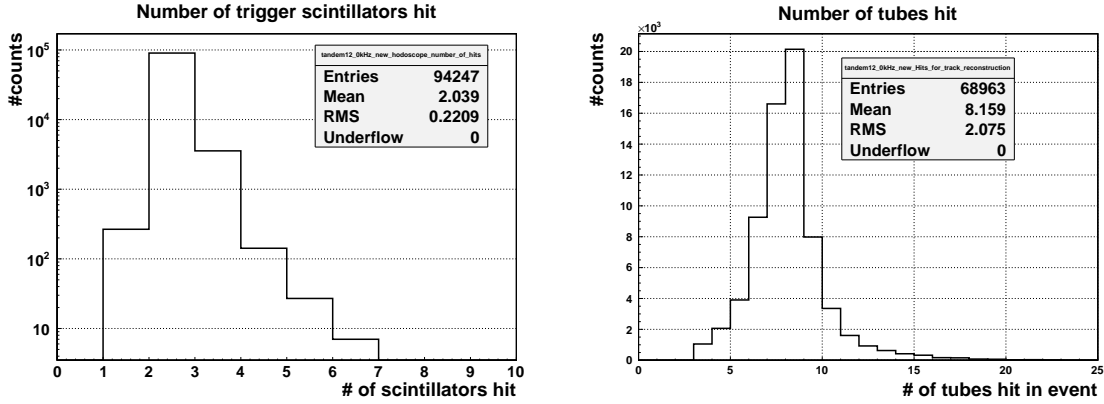
Figure A.5: Distribution of number of trigger scintillators (left) and number of tubes hit per event (right)

many tubes were hit, not allowing a clear straight track to be fit. The hit distribution indicates, that one or more muons passed through the outermost left part of the detector, and in addition the primary irradiated tubes show coincident proton hits.
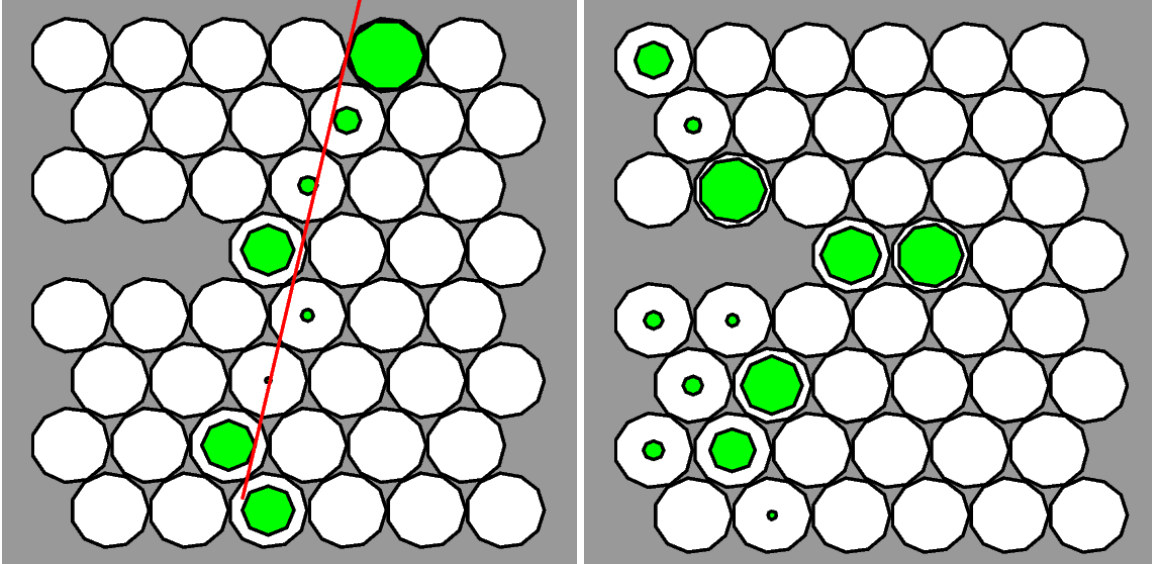

Figure A.6: Example events where the track finding algorithms found a track matching the drift radii (left), and where no unambiguous track could be matched (right)

After a successful muon track reconstruction using only the reference layers, the track is compared with the radius measurement of the corresponding tube in the layer under test. For the determination of the drift radius predicted by the reference track see figure A.7.

With $r_{\text{prediction}} = s \times \cos\alpha$ and $\cos\alpha = \frac{1}{\sqrt{1+\tan^2\alpha}} = \frac{1}{\sqrt{1+a^2}}$ and $s = b + a \cdot z_{\text{wire}} - y_{wire}$ follows:

$$r_{\text{prediction}} = \frac{-y_{\text{wire}} + b + a \cdot z_{\text{wire}}}{\sqrt{1 + a^2}} \tag{A.1}$$

The difference between the radius prediction through the reference track and the measurement of the tube itself defines the residual.

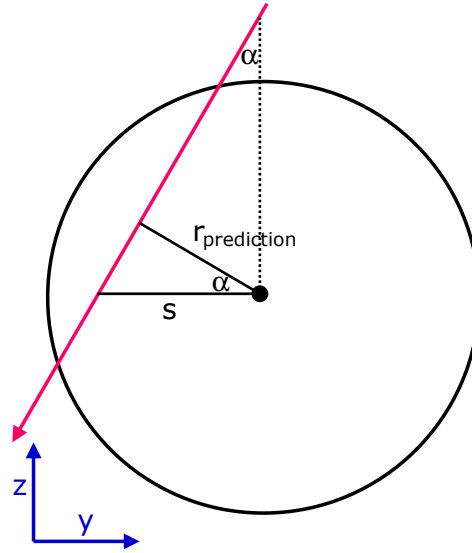$$\Delta r = r_{\text{prediction}} - r_{\text{measured}} \tag{A.2}$$

Figure A.7: Geometric determination of the track distance $r_{\text{prediction}}$ from the tube wire

An example distribution of residuals Δr vs. the radius of the measurement is shown in figure A.8. The distribution shows a band of entries, centered along the horizontal axis for residual $\Delta r = 0$ with a certain width. The outer entries within the band represent events with a greater mismatch between track measurement and prediction, and vice versa.

The tube resolution is a radius dependent value. Therefore the residual distribution is divided into "slices" for radius intervals of 1 mm width. Generally, a finer binning of resolution determination would be desirable, but limited measurement statistics do not allow smaller slice width.

For each slice, a Gaussian function is fitted along the residual axis. The width of the Gaussian function within each bin is then considered the uncertainty of track measurements for hits within this radius interval. Since the muon track prediction is not absolutely precise, the track uncertainty measured within the tested layer is a combination of its own spatial resolution, and the resolution of the reference track. To obtain the spatial resolution of the tested tube layer, the track predictions resolution is subtracted quadratically from the residual width.

$$\sigma = \sqrt{\sigma_{\Delta r}^2 - \sigma_{\text{track}}^2} \tag{A.3}$$

The resolution of the reference track itself contains the resolution of the single tube, so the process of the calculation of the spatial resolution must be iterative, and repeated until the obtained resolution does no longer differ from the resolution used to calculate the reference track resolution. In this work, the iteration was stopped after five steps.

It is clear, that this is only true if the spatial resolution of the tested layer is identical to that of the reference layers, hence this operation is performed with a dataset without proton irradiation, which affects only the single layer under test. Once the resolution for unirradiated tubes is known, it can be used for the track prediction from the unirradiated layers in all datasets.

The iterative method to calculate the reference track resolution is described in detail in [57].

The result for the single tube spatial resolution in the case of the absence of irradiation is shown in figure A.9. This resolution does not yet include corrections for the time slewing effect, which is described in chapter A.1.4.

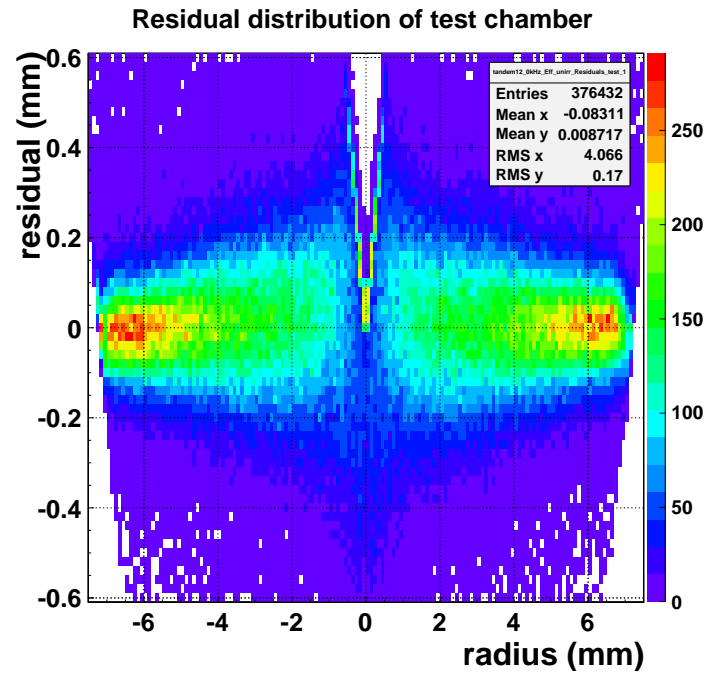**Figure A.8:** Residual distribution over track $r_{prediction}$, defining the mismeasurement of the tube compared to the track prediction.
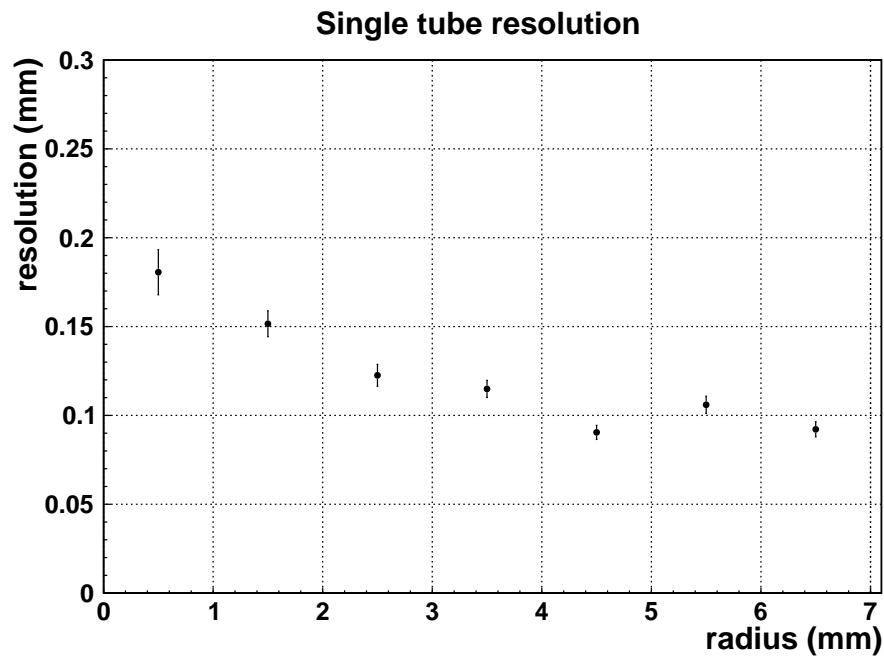

Figure A.9: Single tube resolution in case of no proton irradiation. No Time slewing correction is included yet. The mean resolution value can be obtained by a horizontal fit over all radii.

A.1.4 Time slewing

The signals on the anode wire of the sMDT tube are processed by amplification and signal shaping stages, before they are fed to a discriminator. The discriminator compares its input voltage to a tunable threshold voltage, and as soon as the input voltage is higher than the threshold, the electronics signals a hit, and the drift time measurement is stopped. As mentioned in chapter 2.2 (see figure 2.13), the non-negligible rise time of the analog signal leads to a signal height depending threshold crossing. This time slewing effect is responsible for an unprecise measurement of drift times, especially for low signal heights from muons passing the tube at low radii.

Since the time measurement of the drift electrons is the crucial parameter to calculate the drift radius, it is necessary to compensate for the time slewing effects to achieve best tracking performance. As the sMDT electronics does not only measure the drift time, but also the height of the analog signal within the first 25 ns, it is possible to use this signal height value (ADC counts) to determine a compensation function. The ADC value obtained from the detector electronics is a non-linear but steady function of the analog signal shape [13].

To determine the time slewing compensation function, the residuals of tube hits are plotted against their signal height in a two-dimensional histogram. As the time slewing effect is also drift radius dependent, this operation is performed within radius intervals of 0.5 mm width.
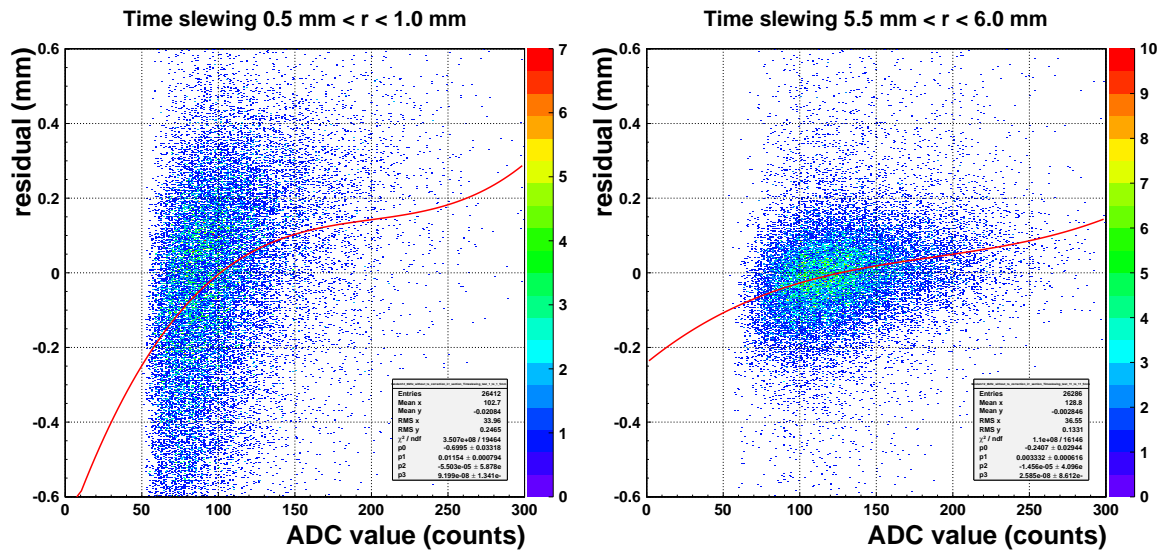

Figure A.10: Determination of timeslewing compensation values

The residual distribution within each of these radius bins shows a visible dependence on the ADC value. Events with a low signal height in between 50 and 100 ADC counts tend to have a negative residual value, which is the result of an overestimation of drift radius and drift time, due to the late crossing of the discriminator threshold. To quantify this value from the experimental residual distributions, a third order polynomial function $\Delta_r(\text{ADC}) = a(\text{ADC}) + b(\text{ADC})^2 + c(\text{ADC})^3$ is fitted. Figure A.10 shows these fit functions for two example radius intervals.

Cosmic muon hits with very high ADC values happen quite rarely, and therefore the residual vs. ADC value plot suffers from low statistics in this region. To avoid unprecise correction values due to a bad polynomial fitting, the correction function is clipped to the value at ADC=200 for ADC values larger than 200 counts.

$$\Delta_r(\text{ADC} > 200) = \Delta_r(200) \tag{A.4}$$

This compensation value for the given drift radius bin is then added to the measured drift radius for each hit in a tube, before the radii are further used for track fitting.

$$r_{\text{corr}} = r_{\text{meas}} + \Delta(r_{\text{meas}}, \text{ADC}) \tag{A.5}$$

The comparison of the compensation functions for different radius bins shows, that the timeslewing effect is most pronounced for signals with small radii, as these tend to be smaller in general (See figure 2.13 for the geometric explanation).

Using the time slewing correction improves the spatial resolution of all detector layers. Therefore the correction enters the iterative process of resolution determination described in chapter 2.5.5. The result is shown in figure A.11, as a comparison of the radius-dependent spatial resolution with and without the application of time slewing correction. The improvement in Δr for small radii up to 4 mm is in the range of 20 μm.
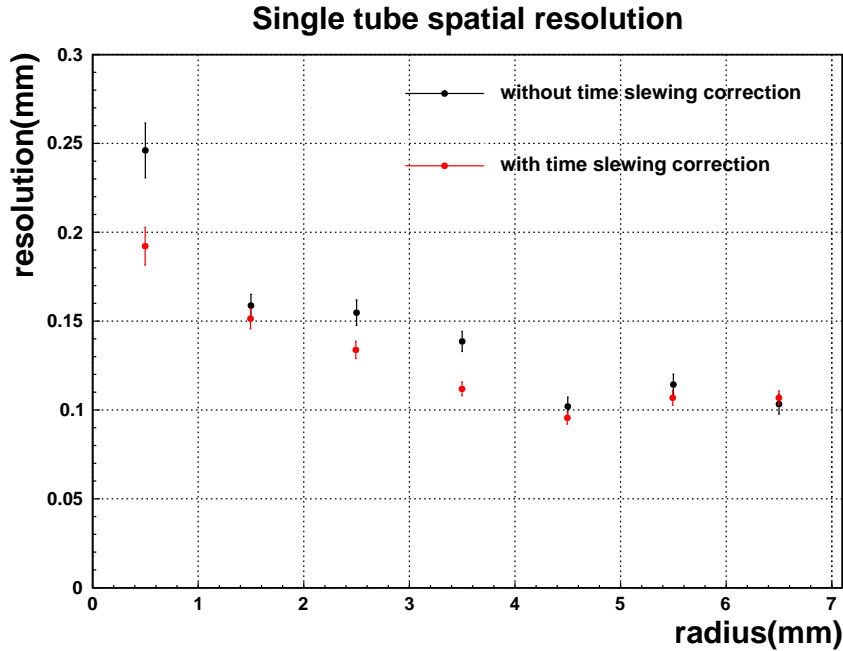

Figure A.11: Improvement of single tube spatial resolution, when applying time slewing correction.

A.1.5   Detector Alignment

Key to an excellent particle tracking operation of the detector it exact knowledge of the tube and wire positions for each tube. A possible source of errors during the tracking process is the misalignment of tubes within the hexagonal structure of the chamber. During the glue curing, precise machined jigs are used to hold the detector tubes in place, maintaining an even layer of glue in between the tubes, and thus a regular arrangement of the tubes. Nevertheless the positioning accuracy must be verified or corrected for during the track reconstruction process.

Another potential source for mismeasurements is the inexact centering of the anode wire within the tube, or an insufficient wire tension, that leads to excessive wire sag. During the tube production, several quality checks are performed [22] to ensure a correct wire positioning and tension, but again this needs to be checked.

The regularity of the horizontal wire positions along the detectors y-axis can be checked with help of the rt-relation of each tube. The drift time is measured by the tubes electronics channel, and the particle track defined by the other tube layers defines a track distance, taking into account the geometry

of the chamber. A potential wire position error can be obtained by the systematic displacement of the V-shaped r-t relation for this tube.

Figure A.12 (left) shows this plot for all tubes. To get the exact value of displacement on the distance-axis, a fourth order polynomial function is fitted into the sliced distribution of each rt relation

$$p_1 + p_2 * |x - p_0| + p_3 * |x - p_0|^2 + p_4 * |x - p_0|^3 + p_5 * |x - p_0|^4 \tag{A.6}$$

The parameter p_0 is then considered the displacement for this tube, or its wire.
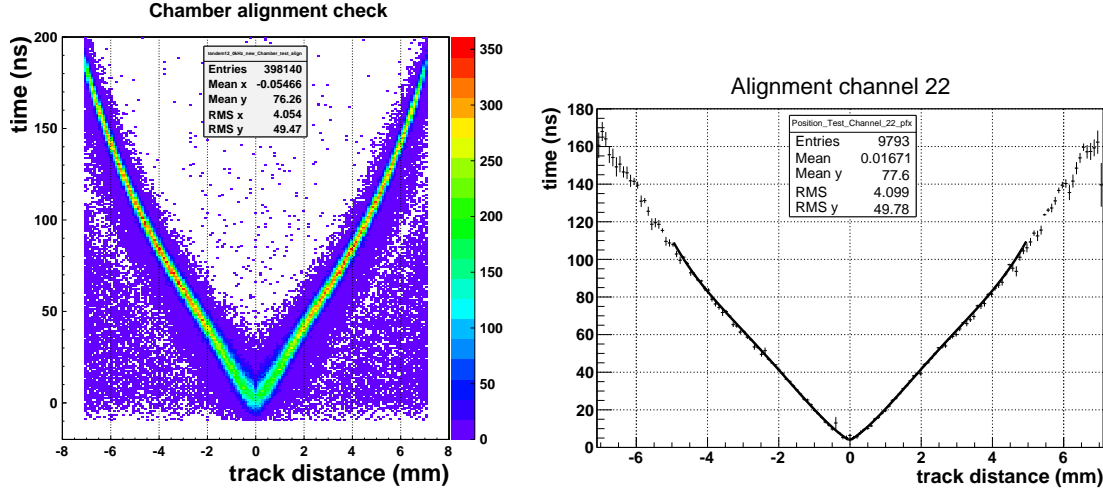

Figure A.12: Check of mechanical chamber alignment by fitting a polynomial function onto the V-shaped rt-relation. Overlay of all 46 rt relations showing the overall excellent quality of the prototype chamber (left). Applicaton for tube 22, y-displacement is below 10 μm (right).

The reconstruction of cosmic muons that hit the chamber perpendicularly at angle zero is insensitive to tube or wire displacements in the vertical z-axis. But with increasing track inclination, a possible vertical z-displacement affects the track reconstruction.

As described in [58], the mismeasurement Δr due to a wire position displacement Δz for a track under the angle α can be written as

$$\Delta r = \Delta z * \sin\alpha \tag{A.7}$$

where Δz can be interpreted as the slope of the Δr value as a function of $\sin\alpha$. Using $\alpha = \arctan a$ with a being the track inclination, and $\sin\alpha = \frac{\tan\alpha}{\sqrt{1+(\tan\alpha)^2}}$ follows

$$\Delta z = \frac{\Delta r}{\frac{a}{\sqrt{a^2+1}}} \tag{A.8}$$

The value for z-displacement can now be obtained by fitting a straight line to the distribution of the value of $\frac{a}{\sqrt{a^2+1}}$, plotted against the residual $\Delta r = r_{\text{prediction}} - r_{\text{measured}}$ as shown in figure A.13.

Here it is necessary to distinguish between tracks passing the tube above and below the wire, because the vertical displacement affects the residual $\Delta r = r_{prediction} - r_{measured}$ either additively or subtractively. To correct for this, δr needs to be inverted for tracks below the wire.

As defined in A.1, $r_{\text{prediction}}$ is negative for tracks passing the tube left of the wire, with the y-axis running from left to right. The multiplication of the sign of $r_{\text{prediction}}$ with the sign of a returns -1 for tracks above the wire. Therefore Δr is multiplied by the term $-1 * \text{sgn}(r_{\text{prediction}} * a)$ before being used.
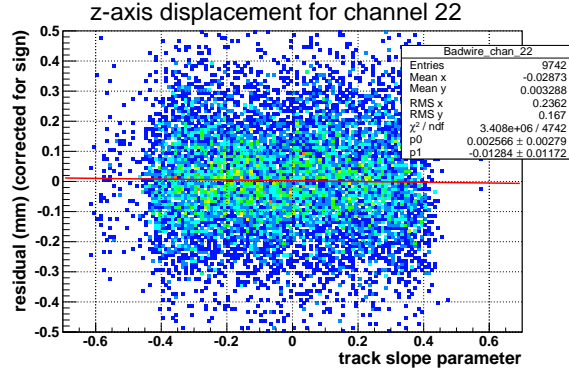
Figure A.13: Distribution of Δr as a function of the track slope parameter $\sin\alpha$ or $\frac{a}{\sqrt{a^2+1}}$, with α being the track angle or $a = \tan\alpha$ the track slope. A vertical displacement of the wire can be directly extracted as the slope, p1 of the distribution.

In addition, this method allows to directly read the wire displacement in y as the offset parameter of the linear function. Nevertheless the method using the rt-relation is expected to be more precise, due to the fact that the majority of the muon tracks are crossing the chamber at small angles, which lead to a small lever arm for the determination of the slope in figure A.13.

A result of the displacement measurements along the y and z-axis is shown in figure A.14. Tubes on the outer chamber boundaries are only partially irradiated and no polynomial function can be fitted to their V-shaped rt-relation reliably. In addition, the geometric acceptance of the triggering scintillators does not allow heavily inclined tracks for the outer tubes, and thus the method to measure the z-displacement cannot be applied, or suffers from very low statistics.
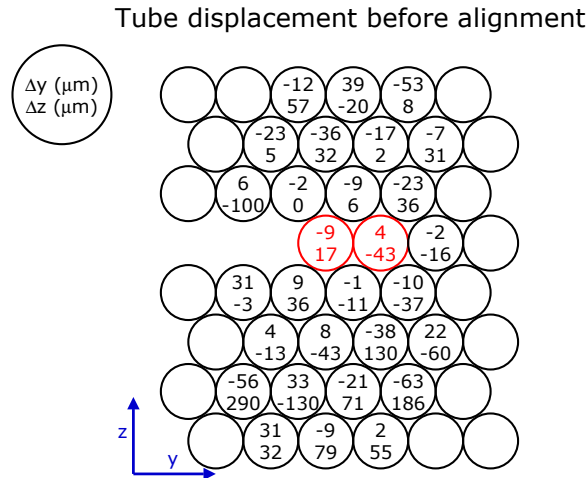

Figure A.14: Displacement of the tubes in y-direction in μm, obtained by the V-fit method and z-displacement obtained by the slope fit method. Tubes on the chamber edges are excluded due to inhomogeneous occupancy. The precision on the z-displacement method is very low, due to a lack of inclined tracks due to geometric restrictions.

Considering the misalignment in y-direction, only several tubes close to the upper and lower chamber border show misplace measurements of more than 20 μm. Especially the tubes of the fourth layer that are irradiated by protons show very small displacement. It turns out, that a correction for the displacement in y-direction has no considerable effect on tube resolution and efficiency of the fourth layer, as shown in figure A.15.

Displacement along the z-axis as determined by the method above shows relatively large displacements for several tubes. These are mostly located close to the horizontal borders of the chamber,
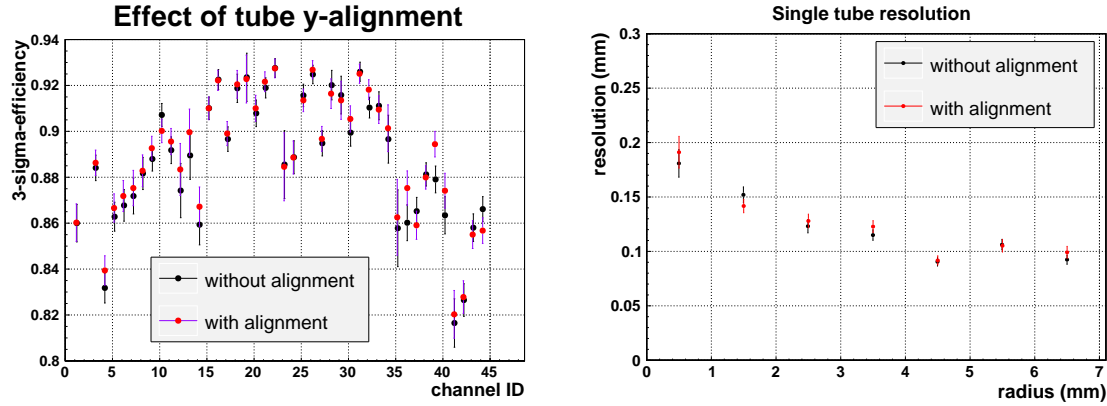
Figure A.15: Negligible effect of the tube y-alignment on efficiency and spatial resolution

where muon statistics for strongly inclined tracks is rather low, due to the geometric triggering constraints. As the lever on the determination of the z-displacement depends on the availability of inclined tracks the measured values should be used with caution. In addition the application of the obtained values has to be performed iteratively and in small steps.

Since the measured displacement for the investigated tubes in the fourth layer is small, and displacements of the outer layers cancel out to some extend as all seven layers are used for track reconstruction, no further alignment of the 46 tube chamber has been taken into account.

A.1.6   Electronics deadtime

The shaping time of the MDT electronics is 15 ns [13]. Together with the relatively large drift time of $\tilde{2}00$ ns for 15 mm tubes ($\tilde{8}00$ ns for 30 mm tubes respectively) and the clustered primary ionization, the analog signal fed into the discriminator of the electronics can fire multiple times per signal, as the threshold voltage is crossed more than once. These additional hits have no value for analysis and consume bandwidth for the following stages of data processing, and must therefore be eliminated. This is achieved by an adjustable deadtime that is applied after each threshold crossing, disabling the discriminator for a certain time.

As this is a necessary feature for data integrity and processing, it is also a source for missed relevant hits at increasing background hit rates. If a muon signal is preceded by a background hit by less than the selected deadtime, it will ultimately be lost, and this tube cannot participate in the muon track reconstruction. This deadtime should be set to a value only slightly above the maximum drift time.

Even if the muon hit lies outside the deadtime of a preceding hit, the analog baseline of the bipolar pulse that has not fully recovered from the preceding hit can affect the subsequent hit. See figure A.16 for example plots that have been captured with a flash ADC module from the diagnosis analog output of the MDT electronics as described in chapter 2.6. The right plot in figure A.16 shows a secondary signal that lies just outside the 200 ns deadtime, but is affected by the reversed polarity pulse generated from the shaping electronics and following the first hit. This second hit might not cross the discriminator threshold and be therefore not detected.
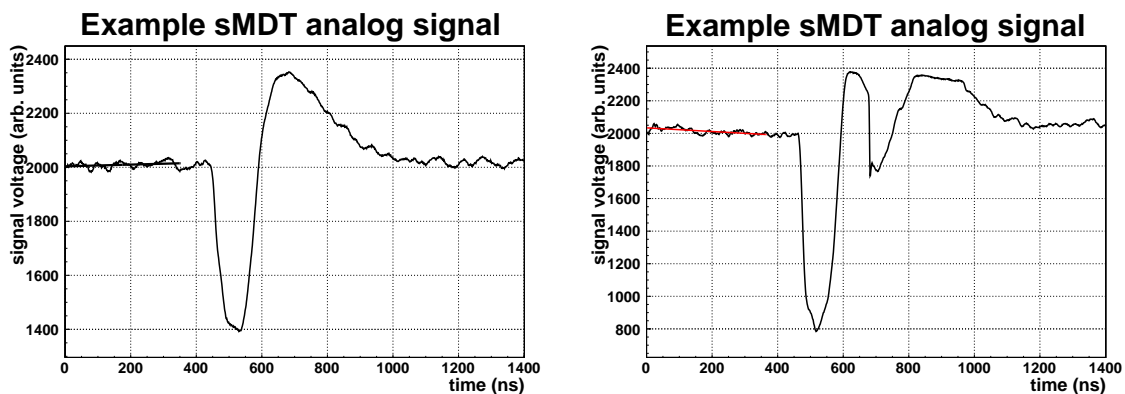
Figure A.16: Typical negative analog signal shapes of a sMDT hit, captured with a flash ADC module from the MDT electronics diagnosis output before being fed to the discriminating circuitry (left). A (negative) follow-up hit can sit on top of the (positive) shaper pulse that follows the preceding signal due to its bipolar nature. (right)

Bibliography

[1] CERN: *LHC Technical Design Report Vol.1*
CERN-2004-003

[2] ATLAS Collaboration: *Observation of a new particle in the search for the Standard Model Higgs boson with the ATLAS detector at the LHC*
Physics Letters B, 716 (2012), 1-29

[3] Caron, J.-L: *The LHC injection complex*
LHC-PHO-1993-008, CERN 1993

[4] ATLAS Collaboration: *CERN twiki sites*
https://www.atlas.ch

[5] T. Lari: *Measurements of spatrial resolution of ATLAS Pixel detectors*
Nucl. Instrum. Meth. A465 (2000) 112 - 114

[6] ATLAS Collaboration: *CERN twiki sites*
https://twiki.cern.ch/twiki/bin/view/AtlasPublic

[7] B. Ruckert: *Search for a Higgs Boson Produced in Association with a W Boson at ATLAS*
Dissertation, LMU Munich (2009)

[8] ATLAS Collaboration: *ATLAS New Small Wheel Technical Design Report*
ATLAS - TDR-20-2013 (2013)

[9] Baranov, S. et al.: *Estimation of Radiation Background, Impact on Detectors, Activation and Shielding Optimization in ATLAS*
ATL-GEN-2005-001 (2005)

[10] L. Ropelewski et al.: *R&D Proposal Development of Micro-Pattern Gas Detectors Technologies*, CERN-LHCC-2008-011. LHCC-P-001 (2008)

[11] S. Martoiu, H. Muller, A. Tarazona, J. Toledo: *Development of the scalable readout system for micro-pattern gas detectors and other applications*, Journal of Instrumentation, Vol. 8 C03015 (2013)

[12] Y Arai et al.: *ATLAS Muon Drift Tube Electronics*
Journal of Instrumentation Vol. 3 P09001 (2008)

[13] J. Huth et al.: *Development of an octal CMOS ASD for the ATLAS Muon detector*
Fifth Workshop on electronics for LHC experiments, Snowmass, CO, USA, 20-24 (1999) Proceedings

[14] Y. Arai, T. Emura: *Development of a 24 ch TDC LSI for the ATLAS muon detector*
KEK-2000-108

[15] Y Arai et al.: *On-chamber readout system for the ATLAS MDT muon spectrometer*
Nuclear Science, IEEE Transactions on, Volume 51 Issue 5 (2004) 2196 - 2200

[16] V. Bcares, J. Blzquez: *Detector Dead Time Determination and Optimal Counting Rate for a Detector Near a Spallation Source or a Subcritical Multiplying System*
Science and Technology of Nuclear Installations, Volume 2012 (2012) 240693

[17] Ch. Posch, E. Hazen, J. Oliver: *MDT-ASD User's Manual*
ATL-MUON-2002-003

[18] C. Cernoch et al.: *MDT performance in presence of a high photon background - results from studies at the Gamma Irradiation Facility and X5 test beam in summer 2002*
ATL-MUON-2004-006

[19] F. Rauscher: *Untersuchung des Verhaltens von Driftrohren bei starker γ Bestrahlung sowie Vermessung von Driftrohrkammern mit Hilfe von Myonen der kosmischen Höhenstrahlung.*
Dissertation, LMU Munich (2005)

[20] L. Huber: *Analyse der Pulsform und Untergrundeigenschaften von Ar-CO2-N2 Driftgasen an MDT-Driftrohren*
Bachelor thesis, LMU Munich (2009)

[21] A. Zibell: *Pulsformanalyse an MDT Myondetektoren*
Diploma thesis, LMU Munich (2010)

[22] P. Schwegler: *Construction and test of Muon Drift Tube Chambers for high Counting Rates*
Diploma thesis, TU Munich (2010)

[23] B. Bittner: *Development and Charakterisation of New High-Rate Muon Drift Tube Detectors*
Dissertation, TU Munich (2012)

[24] R. Veenhof: *Garfield - simulation of gaseous detectors*
http://garfield.web.cern.ch/garfield/

[25] J. Beringer et al (Particle Data Group): *Particle Physics Booklet*
Phys. Rev. D 86, 010001 (2012)

[26] Stefan König: *Ageing studies for the ATLAS MDT Muonchambers and development of a gas filter to prevent drift tube ageing*
Dissertation, Freiburg (2008)

[27] *ATLAS muon spectrometer technical design report*
CERN/LHCC/97-22 ATLAS TDR 10 (1997)

[28] Maier-Leibnitz-Laboratorium der Universität München und der Technischen Universität München: *Tandem-van-de-Graaff Beschleuniger*
http://www.bl.physik.uni-muenchen.de/

[29] James F. Ziegler: *SRIM/TRIM The stopping and range of ions in matter*
https://www.srim.org

[30] S. Haas, M. Joos, W. Iwanski: *A PCI interface with four 2 Gbit/s serial optical links*
Nuclear Science Symposium Conference Record, Volume 3 (2004) 1535 - 1539

[31] B. Bittner et al.: *Performance of drift-tube detectors at high counting rates for high-luminosity LHC upgrades*
Nuclear Instruments and Methods in Physics Research Section A, Volume 732 (2013) 250 - 254

[32] P. Schwegler: *Studies on sMDT muon detectors*
Dissertation in preparation, TU Munich 2014

[33] A. Ruschke: *Erzeugung von hochenergetischen Neutronen und Protonenbestrahlungen an ATLAS Driftrohren*
Diploma thesis, LMU Munich 2010

[34] T. Müller: *Monitored Drift Tube-Detektoren des ATLAS-Experiments im Neutronenuntergrund*
Diploma thesis, LMU Munich 2006

[35] J. H. Hubbell, S. M. Seltzer: *Tables of X-Ray Mass Attenuation Coefficients and Mass Energy-Absorption Coefficients from 1 keV to 20 MeV for Elements Z = 1 to 92 and 48 Additional Substances of Dosimetric Interest*
http://www.nist.gov/pml/data/xraycoef/

[36] S. Ahlen, J. Butler, M. Kruskal, J. Love: *High Energy Neutron Rates in the ATLAS MDT Chambers for $\sqrt{s}$=7 TeV pp Collisions*
ATLAS NOTE, ATL-COM-MUON-2010-020, September 9 (2010)

[37] M. Lambacher: *Study of fully hadronic ttbar decays and their separation from QCD multijet background events in the first year of the ATLAS experiment*
Dissertation, LMU Munich (2007)

[38] Y. Giomataris et al.: *MICROMEGAS: a high-granularity position-sensitive gaseous detector for high particle-flux environments*
Nuclear Instruments and Methods in Physics Research Section A, Volume 376 (1996) 29 - 35

[39] T. Alexandropoulos et al.: *A spark-resistant bulk-micromegas chamber for high-rate applications*
Nuclear Instruments and Methods in Physics Research Section A, Volume 640, Issue 1 (2011) 110 - 118

[40] G. De Geronimo et al.: *VMM1 - An ASIC for Micropattern Detectors*
IEEE Transactions on Nuclear Science, Volume 60, Issue 3 (2013) 2314 - 2321

[41] C. P. Bee, D. Francis, L. Mapelli, R. McLaren, G. Mornacchi, J. Petersen, F. Wickens: *The raw event format in the ATLAS Trigger & DAQ*
ATL-DAQ-98-129 (1998)

[42] A. Kugel: *The ATLAS ROBIN A High-Performance Data-Acquisition Module*
CERN-THESIS-2009-113, Dissertation, Mannheim (2009)

[43] H.C. van der Bij, R.A McLaren, O. Boyle, G. Rubin: *S-LINK, a data link interface specification for the LHC era*
IEEE Trans. Nuclear Science, Volume 44 (1997) 398 - 402

[44] L. Jones et al.: *The APV25 deep submicron readout chip for CMS detectors*
Fifth Workshop on electronics for LHC experiments, Snowmass, CO, USA, 20-24 (1999) Proceedings

[45] P. Moreira, A. Marchioro, P. Placidi: *CMS Tracker PLL Reference Manual*
CERN (2000)

[46] L. Jones: *APV25-S1: User guide version 2.2*
RAL Microelectronics Design Group (2001)

[47] A. Tarazona Martinez: subm. to 2013 TWEPP conference (JINST)

[48] J. Christiansen, A. Marchioro, P. Moreira and A. Sancho: *Receiver ASIC for Timing, Trigger and Control Distribution in LHC Experiments*
IEEE Trans. Nuclear Science, Volume 43 (1996) 1773 - 1777

[49] A. Zibell: *Development of a ReadOutDriver (ROD) for ATLAS micromegas*
Nuclear Instruments and Methods in Physics Research Section A, Volume 718 (2013), 260 - 261

[50] S. Haas et al.: *HOLA card website*
http://hsi.web.cern.ch/hsi/s-link/devices/hola/

[51] A. Aloisio et al.: *S-LINK on a Chip for Embedded Applications*
Nuclear Science Symposium and Medical Imaging Conference (NSS/MIC), IEEE (2012), 1090 - 1091

[52] *SRS slow control manual*
http://test-rd51-wg5-v2.web.cern.ch/test-rd51-wg5-v2/srsdoc/SRS_Slow_Control_Manual.htm

[53] Y. Kataoka, S. Leontsinis, K. Ntekas: *Performance Studies of a Micromegas Chamber in the ATLAS Environment*
arXiv:1310.8603 [physics.ins-det]

[54] O. Brüning et al.: *LHC Design Report Vol. 2*
CERN-2004-003-V-2

[55] P. Lösel: *Performance Studies of Large Size Micromegas Detectors*
Master thesis, LMU Munich 2013

[56] H. Kroha et al.: *Proposal for the Upgrade of the Elevator Regions in the ATLAS Barrel Muon Spectrometer*
ATL-MUON-INT-2014-001 (2013)

[57] S. Horvat: *Study of the Higgs Discovery Potential in the Process $pp \rightarrow H \rightarrow 4\mu$*
Dissertation, TU Munich 2005

[58] A. Mlynek: *Ortsauflösung der Driftrohre des ATLAS-Myonspektrometers bei Neutronenuntergrund*
Diploma thesis, LMU Munich 2006